This project has received funding from the European Union's Horizon 2020 research and innovation programme under grand agreement No 773715

**Grant Agreement No**.: 773715

**Project acronym**: RESOLVD

**Project title**: Renewable penetration levered by Efficient Low Voltage Distribution grids

**Research and Innovation Action**

**Topic**: LCE-01-2016-2017

Next generation innovative technologies enabling smart grids, storage and energy system integration with increasing share of renewables: distribution network

**Starting date of project**: 1st of October 2017

**Duration**: 36 months

# D2.4 – Power sharing strategies for performance optimization of a heterogeneous grouping of storage devices into the power electronics device

| Organization name of lead contractor for this deliverable: UPC | |
|---|---|
| **Due date:** | M28 – 31th of July 2019 |
| **Submission Date:** | 31th of July 2019 |
| **Primary Authors** | UPC – F. Díaz-González; F. Girbau-Llistuella; M. Aragüès; M. Llonch<br>JR – K. Nahrgang; H. Vallant<br>SIN – C. Willems<br>UdG – A. Ferrer |
| **Contributors** | UPC, SIN, UdG, JR |
| **Version** | Version 3.0 |

| Dissemination Level | | |
|---|---|---|
| **PU** | Public | X |
| **CO** | Confidential, only for members of the consortium (including the Commission Services) | |

This project has received funding from the European Union's Horizon 2020 research and innovation programme under grand agreement No 773715

## Deliverable reviews

| Revision table for this deliverable: | | |
|---|---|---|
| **Version 1.0** | Reception Date | 26st of July 2019 |
| | Revision Date | 30st of July 2019 |
| | Reviewers | K. Nahrgang (JR) |
| **Version 2.0** | Reception Date | 26st of July 2019 |
| | Revision Date | 31st of July 2019 |
| | Reviewers | Q. Melendez (UdG) ; |
| **Version 3.0** | Reception Date | 26st of July 2019 |
| | Revision Date | 31st of July 2019 |
| | Reviewers | Q. Melendez (UdG); F. Díaz-González (UPC) |

## Contributions of partners

| Partner | Contribution |
|---|---|
| **UPC** | Main contributor for the development and testing of the power sharing algorithm. |
| **UdG** | Collaboration in performing an iterative procedure to test the performance of the power sharing algorithm while in connection to the scheduling algorithms managing the whole power network. |
| **SIN** | Support in the definition of the power sharing algorithm. Support in the definition of degradation costs for batteries. |
| **JR** | Main contributor for the cybersecurity assessment. |

# Table of contents

# Table of Figures

# Acronyms and abbreviations

| | |
|---|---|
| BMS | Battery Management System |
| DAA | Data Acquisition Application |
| DEA | Data Exchange Application |
| DLA | Data Logger Application |
| DoD | Depth of Discharge |
| ESS | Energy Storage System |
| HTTP | Hypertext Transfer Protocol |
| HTTPS | Hypertext Transfer Protocol Secure |
| ILEM | Intelligent Local Energy Manager |
| LMM | Local Manual Mode |
| MIA | Main ILEM Application |
| MOA | ILEM Mode Operation Application |
| NLP | Non Linear Problem |
| PED | Power Electronics Device |
| RAM | Remote Automatic Mode |
| MRM | Manual Remote Mode |
| SCADA | Supervisory Control And Data Acquisition |
| SOC | State of Charge |
| SSH | Secure Shell |
| VSA | ILEM Voltage Support Application |
| WSA | ILEM Webserver Application |

## Executive Summary

This report summarizes the work done in regard of the development of the so-called Power Sharing Algorithm (PSA). The PSA is one of the algorithms composing the local controller of the Power Electronics Device (PED). The PED development is the main goal of Work Package 2 of the RESOLVD project.

The PSA receives a time-dependent power profile set-point from the network operator, and distributes it among the different battery types embedded into the PED. This way, it triggers an internal power sharing, based on the criteria of maximum performance and minimum battery degradation. Following contents summarizes the contents in regard of the development of the PSA, all included in this deliverable 2.4.

The main objective of deliverable 2.4 is to the report the design the PSA, evaluate its performance and assess its integration as one of the modules of the Intelligent Local Energy Manager (ILEM) software, which is the software in charge of connecting the Power Electronics Device (PED) with the rest of the power network. As specific objectives, the report considers:

i) The formulation of the PSA, as an optimization mathematical problem that can be recurrently executed as part of ILEM, providing real time power set-points for the different batteries embedded into the PED.

ii) The development of a simulation environment for evaluating the dynamic behavior of the batteries embedded into the PED while driven by the set-points from the PSA.

iii) The evaluation of the performance of the PSA in terms of managing the PED to follow the time-dependent power profile set-point calculated by the network operator, while ensuring minimum battery degradation.

iv) The integration of the PSA as part of the ILEM, also addressing the cybersecurity aspect.

As defined in previous tasks of Work Package 2, the PED holds two battery types. The first one is a lithium-ion pack, rated at 30 kWh and nominal voltage around 345.6 V. The second one is a lead-acid pack, providing about 14 kWh and with nominal voltage about 240 V. As a result, the PED holds a total of 44 kWh in energy. The power ratings of the PED are 75 kVA at grid side. However, the power that each battery type can exchange is bounded at 20 kW, by the associated dc-dc converter connected at their respective terminals.

To evaluate at the design stage the dynamic behavior of the PED and embedded batteries, a simulation environment in Matlab Simulink is included in the section 2 of the deliverable. This simulation environment will serve afterwards to check the accuracy of the PSA (and of the algorithm executed by the network operator in charge of providing the power set-points to the PED, the Grid Operation Scheduler) while estimating the SOC of the batteries.

For the characterization and modelling of the lithium-ion battery pack in the PSA, laboratory tests were carried out. In there, the pack was connected to a grid connected bidirectional voltage source converter. The ratings of this converter are 50 kVA in power and up to 800 V dc voltage. At the grid side, the converter can be connected to a three-phase 400 V ac network. The converter communicates with the battery pack through a MODBUS RS485 protocol. Through this converter, a train of charging and discharging current pulses were applied to the battery. As a consequence, the battery was fully charged and discharged. Then, through the application of the least-squares estimation theory (explained in Annex II), the parameters of the battery model were found. This exercise is necessary because of the little information usually provided in manufacturer's datasheet for such high-tech lithium-ion packs. Tests results are reported in section 2.2.1 of this deliverable.

After the development of the simulation environment and the description of the tests for the characterization of the battery packs, the formulation of the PSA is presented in section 3.

The hybridization of an energy storage system, so the inclusion of different types of batteries, permits to take advantage of the main performances of each one depending on the service to provide. However, to do so, the heterogeneous grouping of batteries must be managed optimally. Such exercise is solved through a mathematical optimization (i.e. the PSA) using diverse and representative time series data on the grid power flows.

The PSA is formulated as a multi-objective function to be minimized. The objective function is:

$$z = \alpha \cdot \frac{z_p}{Z_p^*} + \beta \cdot \frac{z_{d1}}{Z_{d1}^*} + \gamma \cdot \frac{z_{d2}}{Z_{d2}^*}$$

The terms $Z_p^*$, $Z_{d1}^*$ and $Z_{d2}^*$ are determined after running 3 optimization problems. The first is to minimize the discrepancy between the power output of the PED and the power scheduling profile ($\alpha = 1, \beta = \gamma = 0$). The corresponding optimal solution is $Z_p^*$. The second is to minimize the degradation cost for the batteries as function of excessive driving currents ($\beta = 1, \alpha = \gamma = 0$). The corresponding optimal solution is $Z_{d1}^*$. The third is to minimize the degradation cost for the batteries as function of excessive depth of discharge ($\gamma = 1, \alpha = \beta = 0$). The corresponding optimal solution is $Z_{d2}^*$. So, each time the PSA is executed (e.g. in an hourly basis), it is in fact solved four times. Tests performed and reported in this deliverable indicated that considering time-dependent power profile series of 24 set-points, the time needed for carrying out such four executions for the PSA is just few seconds at most. Thus, formulating this as a multi-objective criteria problem, it becomes feasible to be applied on field for the purposes of the project.

Costs $z_{d1}$ and $z_{d2}$ are formulated considering some parameters weighting the degradation of lithium-ion and lead-acid batteries in terms of the driving currents and of the depth of discharge. This approach is motivated by a literature review on battery degradation mechanisms, from which, in general terms, we can conclude that:

i) **The higher the depth of discharge, the lower the lifespan of batteries**. This has sense, since high depth of discharge means to utilize most of the active material in battery electrodes for electrochemical reactions and thus, batteries become degraded.

ii) **The higher the current rate, the lower the lifespan of batteries**. This also has sense, since the higher the current, the higher also the density of electrochemical reactions happening in the electrodes and thus degrading them.

So, a comparison of degradation mechanisms for lithium-ion and lead-acid batteries on the above mentioned terms serve to weight the parameters associated to costs $z_{d1}$ and $z_{d2}$. This work is included in section 3.1.

Then, section 4, presents a study case for the performance evaluation of the PSA. Two different exercises are carried out. The first one aims to test the PSA while driven by an arbitrary, academic time-dependent power profile set-point. The adoption of such academic power set-point eases the performance evaluation of the PSA while letting the PED to develop a power as close as possible to the demand, while also minimizing batteries degradation. The second exercise aims to test the PSA while driven by a realistic time-dependent power profile set-point. This profile is solved by the power network operator, addressing the needs of the grid for the next 24 hours. This second exercise aims to also reproduce the interaction between the Grid Operation Scheduler, carried out by the network operator, and the PSA.

For such second exercise, an iterative procedure is needed, and this is described through the following steps. The first step of this iterative process is the estimation of the future State of Charge of batteries, SOC. The partials and averaged SOCs are estimated taking into account the current power set-points and the current SOCs. Note that the partials SOCs corresponds to lithium and lead-acid batteries. The second step initializes when the averaged SOC is forecasted. The Grid Operation Scheduler is executed according to the most recent consumption and generation forecasts. Posteriorly, the energy schedule for the next 24 hours is requested to the PED. The third step is mainly the power sharing algorithm which takes this energy schedule and tries to

optimize it to ensure the requested power and procure to take care of batteries. Finally, it defines how much energy comes from lithium and lead-acid batteries. Simultaneously, the battery behavior simulation is performed in order to calculate the real SOCs when the batteries perform the requested energy set-points. The results are the point of departure for the estimation of future SOCs.

Results of such iterative process show how the PSA manages the charging and discharging of the batteries following the power set-points from the network operator. Little discrepancy between the requested power and the developed by the PED is noticed. In fact, the output of the PED mostly fits with the requested value for most of the evaluated time periods, and for those presenting discrepancies, the error with respect to power demand is lower than 10%. Such performance validates the interaction between the management algorithm carried out by the network operator, i.e. the Grid Operation Scheduler, and the PSA.

The interaction between both algorithms is also assessed in terms of the discrepancies between the estimated SOCs. The problem here is that the PSA models and estimates the SOC for each of the batteries embedded into the PED, while the Grid Operation Scheduler considers an aggregated SOC for the set of batteries. This accounts for a loss of accuracy in SOC estimation. Anyhow, performance of both algorithms in SOC estimation was proved to be quite accurate. In particular, the error for both algorithms in SOC estimation (PSA and Grid Operation Scheduler) was below 10% for almost all evaluated cases.

After section 2, 3 and 4, which are central parts for the PSA development and testing, the deliverable includes section 5, in which the integration of the PSA into the ILEM is described. Also, the cybersecurity aspect is assessed, motivated by the fact that the ILEM is actually exchanging information with other agents of the network. The PSA was defined as a module of the software ILEM, which manages the whole PED. The way it interacts with the rest of the modules of ILEM was presented in section 5 in a comprehensive and synthetic way.

The aim of the cybersecurity check is the identification of typical application and configuration vulnerabilities of the public available services. Section 5.2 gives an overview about the systems which were investigated, describes the testing approach and lists the recommendations and actions to take. This security audit was based on a grey box approach where the partner of the RESOLVD project, Joanneum Research, investigated the provided IP address on a single host. This host is secured by a whitelisting approach, which is a good and secure way to prevent public access. Therefore, it was not possible to access it until the administrators whitelisted the IP address which were used for the audit. The security audit identified a total of one low and two medium vulnerabilities. These vulnerabilities were in regard of SSH user enumeration; unencrypted communications; and weak directory listing. These vulnerabilities are considered as recommendations for the field implementation of the PED.

# 1. Introduction

This report summarizes the work done in regard of the development of the so-called Power Sharing Algorithm (PSA, hereinafter). Based on a time-dependent power profile set-point received by the Power Electronics Device (PED), the PSA distributes it among the different battery types embedded in. This way, it triggers an internal power sharing, based on the criteria of maximum performance and minimum battery degradation. **Figure 1** depicts the main subsystems of the PED, depicting the power electronic modules, the batteries and the ILEM, in which the PSA is embedded.

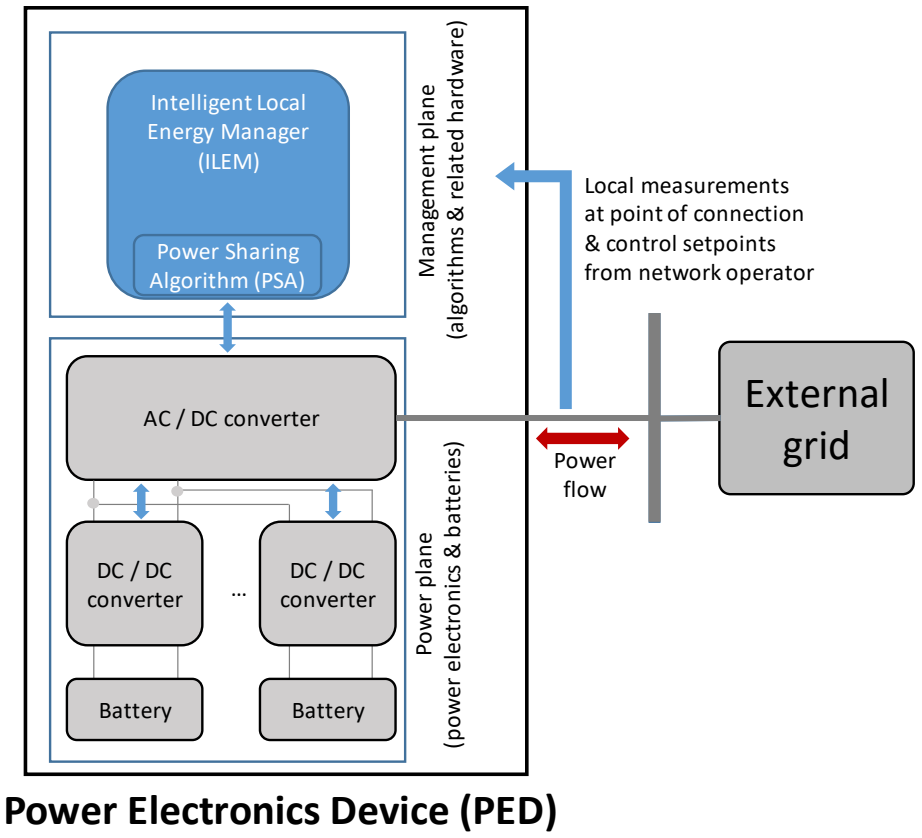


**Figure 1**. The Power Electronics Device (PED).

Following contents succinctly states the objectives of the report and its structure.

## 1.1. Objectives

The main objective of the report is to design the PSA, evaluate its performance and assess its integration as one of the modules of the Intelligent Local Energy Manager (ILEM) software, which is the software in charge of connecting the Power Electronics Device (PED) with the rest of the power network. As specific objectives, the report considers:

i) The formulation of the PSA, as an optimization mathematical problem that can be recurrently executed as part of ILEM, providing real time power set-points for the different batteries embedded into the PED.

ii) The development of a simulation environment for evaluating the dynamic behavior of the batteries embedded into the PED while driven by the set-points from the PSA.

iii) The evaluation of the performance of the PSA in terms of managing the PED to follow the time-dependent power profile set-point calculated by the network operator, while ensuring minimum battery degradation.

iv) The presentation of the integration of the PSA as part of the ILEM, also addressing cybersecurity aspect.

The scope of the report is bounded by the level of PED hardware development at the time of writing it. The PED prototype is to be finished during the second year of RESOLVD project. Consequently, the performance evaluation of the PSA on field is addressed in other tasks of the project and reported in associated deliverables. For the present work, the dynamic behavior of the PED is estimated from simulations through a simulation platform in Matlab Simulink. Nevertheless, the methodology for the work presented in this report does already include laboratory tests for the characterization of one of the battery packs to be embedded into the PED.

The target audience for this report is composed by engineers and researchers in the field of energy storage and power systems.

### 1.2. Report structure

Section 2 introduces the PED as a hybrid energy storage system. The concept of power sharing is defined and then, a simulation platform for the different subsystems of the PED, i.e. power electronics and batteries, is presented. Further, the electrical environment at which the PED is connected to, so the rural distribution grid of EyPESA is introduced. Further even, a typical shape of the time-dependent power profile set-point for the PED while connected to this power network is depicted. Altogether aims to provide a complete and high-level picture of the technology and the adopted testing scenario.

Section 3 addresses the formulation of the PSA, as a mathematical optimization problem. The input data, decision variables, problem constraints and objective function are presented.

Section 4, after describing the technology, testing scenario and the PSA, describes a study case for performance evaluation. The PSA is firstly evaluated adopting an arbitrary, academic time-dependent power profile setpoint, so the way it adjusts the output of the PED in time and considering the degradation of the batteries can be easily appreciated. Then, the PSA is tested as it were actually implemented in the PED and working on field. This way, it recurrently receives time-dependent power profile setpoint from the network operator, determines the output of the different batteries included in the PED, and interact back with network operator to perform the next iteration.

After the performance evaluation, Section 5 presents how the PSA is integrated into the ILEM software. This software acts as the bridge between the PED and the rest of the network and also includes various modules for the internal management of the PED. Finally, as receiving exogenous signals and sending back information to other actors of the network, cybersecurity aspect is assessed also in this section.

Section 6 summarizes the main conclusions of the work.

Finally, three annexes complete the document, detailing on the modeling of the PED, the testing procedure of the lithium-ion battery pack in laboratory for its parametrization, and on cybersecurity analysis.

## 2. Hybrid energy storage system for grid support

The services the Energy Storage Systems (ESSs) can provide in distribution grids are various. Among them, there are services related to the power quality improvement (e.g. reduction of phase unbalances and current harmonics, smoothing of fast fluctuations of power flows; compensation of reactive currents as well). For such services, little or none active power exchange with the grid is needed from a battery. The stress is in the power ratings of the associated power electronic modules to the batteries instead; for batteries, it is on providing short time response and high cyclability. On the other hand, other services such as the balancing or time shifting of renewable generation according to technical grid constraints (e.g. congestion), market premises (e.g. electricity price), and consumer habits (e.g. consumption profiles) require to actively and smartly exchange the energy stored in batteries in an hourly basis. A review of such services can be found in [1].

The hybridization of ESSs, so the inclusion of different types of batteries, permits to take advantage of the main performances of each one depending on the service to provide. However, to do so, the heterogeneous grouping of batteries must be managed optimally. The solving of such management optimization is the main object of the present work. Such exercise is solved through a mathematical optimization using diverse and representative time series data on the grid power flows. This describes the scope of the work, which is complemented graphically in **Figure 2**. As can be noted, the grid operator, through its corresponding management algorithm, which is called Grid Operation Scheduler, provides input data for the PSA. The PSA, in addition, considers the status of batteries embedded into the PED, noted in the Figure as a hybrid energy storage solution, and provides the setpoints for charging / discharging each of the battery packs.

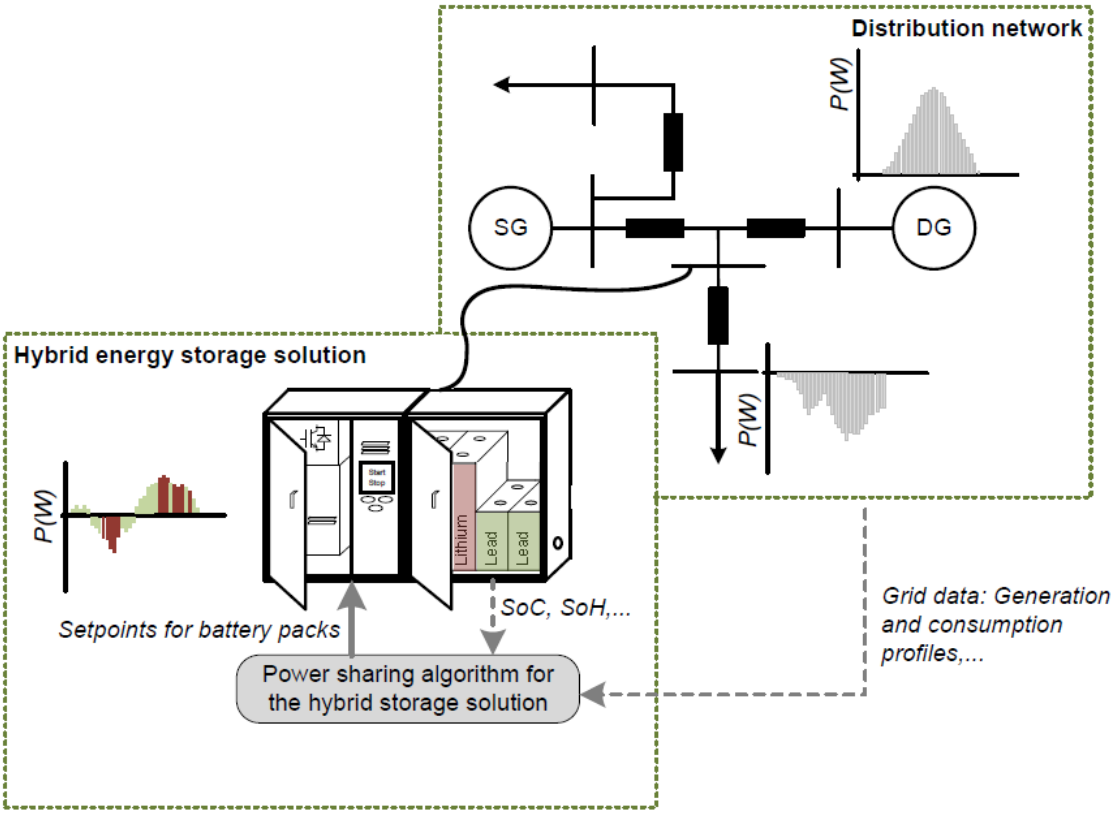


**Figure 2**. The concept of power sharing algorithm (PSA) for the hybrid storage solution (the PED).

The topology and ratings of the hybrid energy storage system, named as Power Electronics Device, PED, in RESOLVD project, were determined in previous deliverables (deliverable D2.1

and D2.2). As a summary, the required size for PED, this is determined around **75 kVA** in power and **44 kWh** in energy.

In order to provide 75 kVA peak power, three power inverters will be connected in parallel, 25 kVA each. Two of these inverters would be employed so as to exchange active power with the main grid (i.e. charging or discharging batteries when needed). The third converter would be employed to solve the above mentioned power quality issues. Such strategy provides the PED with enhanced operational flexibility. Internally, two different battery types will be integrated: a lead-acid pack and a lithium-ion one. The main performances of such hybrid solution will be exploited synergistically. Each pack will be integrated into the PED through a dedicated dc-dc power converter. The ratings (in energy) of each battery pack are around: 14 kWh for the lead-acid pack, and 30 kWh for the lithium-ion one. The rated power for each of the packs is the same and limited to 20 kW by the associated dc-dc power converter.

This permits to feed the whole neighbourhood under consideration in SS 030 and SS 528 simultaneously during 4 hours approximately while isolated from the main grid and in summer months (this time period of energy supply is diminished in winter).

The rest of the section, further deepening in the description of the problem of developing a hybrid ESS for grid support, presents the modeling of a distribution grid, stressing in the main defining characteristics; and of the hybrid ESS itself, depicting the modeling of both the batteries and the associated power electronics. The development of the mathematical optimization problem (i.e. the power sharing algorithm, PSA) is presented in a dedicated section afterwards, since comprising the main object of the work.

### 2.1. Grid model

The study case is based on the pilot grid. The grid is composed by two radial lines supplied by two corresponding Secondary Substations (SS), namely CT-030 and CT-528. Each line has 12 CUPS installed each one with a power between 4.4kW – 8.8kW, few CUPS which are connected to the same bus have been aggregated in order to simplify the grid model.

After the aggregation, the model consists on a total of 43 buses; 17 at line CT-030 where we have 7 consumption nodes at different buses and 2 generation ones, and 26 buses at line CT-528 with also 2 producers but 9 consumption points. The 4 distributed generators are photo-voltaic technologies of 4.9kW – 7.5kW.

Naturally, we have a total of 41 branches between the buses and one additional switch connecting both radial lines. We also have as well the batteries embedded into the PED located at the same CT-030 bus.

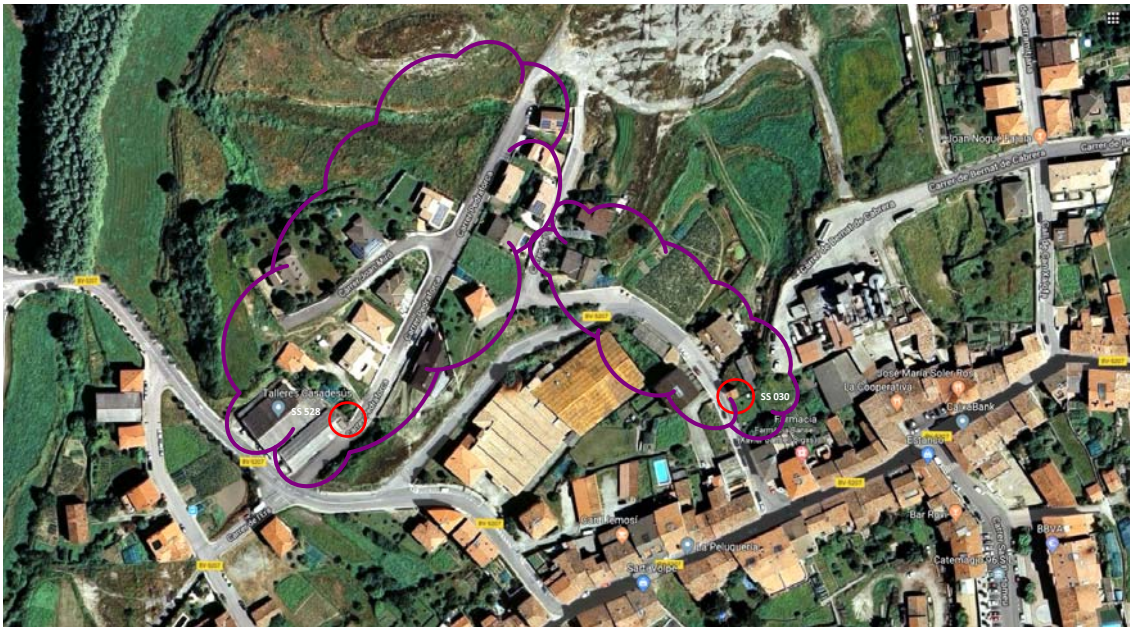


**Figure 3.** Aerial picture of the pilot network. The two SSs are circled in red.

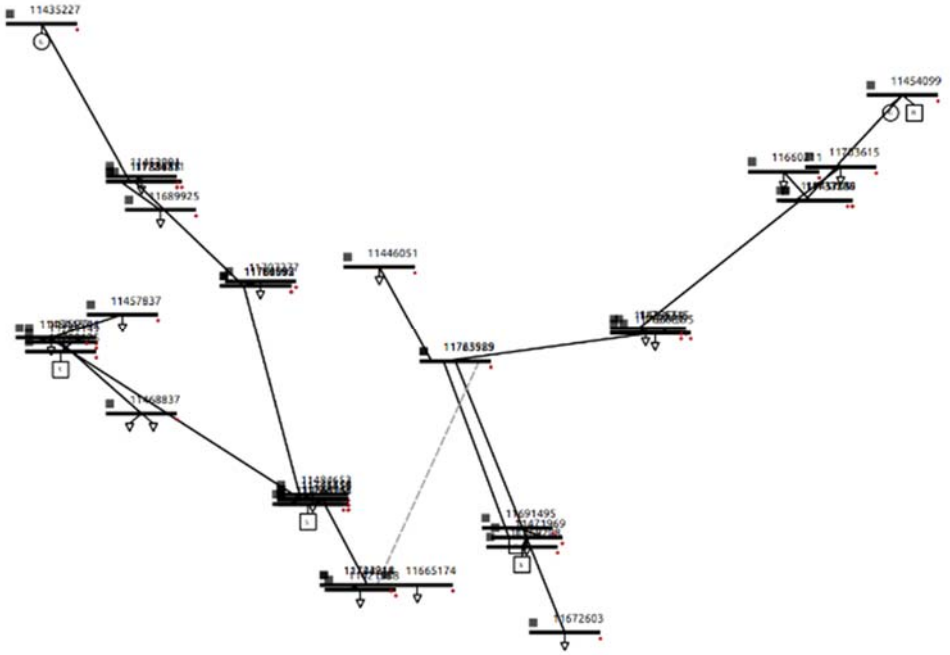


**Figure 4.** Grid representation using the real coordinates distribution.

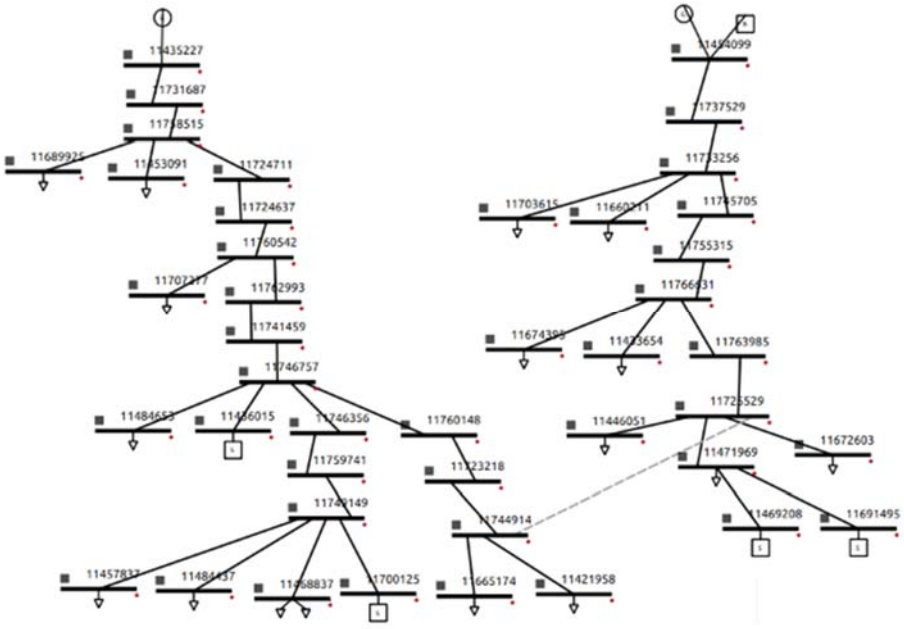


**Figure 5.** Grid scheme.

In order to study the grid, we have used the measured historic data between February and December 2017 of both consumers and producers. To emulate the forecast uncertainty, we have considered a 30% MAPE for the loads forecast and 10% for the generation, nevertheless these is only used for the robust approach applied in the reconfiguration of the grid with the switch.

Based on the above assumptions, the time-dependent power profile set-points for the PED are determined by an optimization algorithm so-called "Grid Operation Scheduler".

The algorithm applied to optimize the set points of the battery is a Particle Swarm Optimization (PSO) used to evaluate the search space in order to minimize a given fitness function/ objective. The fitness function proposed is composed by two terms, the main one wants to flatten the energy curve in the CT-030 by performing **peak-shaving**, the second term wants to keep as low as possible the use of the battery in order to longer the last battery life. The importance of each term is determined by a decision-making parameter.

$$\min\{\nu \cdot F_1 + (1-\nu) \cdot F_2\} \quad (1)$$

$$F_1 = \theta_1 \sum_t E_{G_t}^2 \quad (2)$$

$$F_2 = \theta_2 \sum_t (soc_t - soc_{t-1}) \quad (3)$$

The branch switch has been considered to be open all the time for the purposes of the present deliverable, therefore only the CT-030 part (where the battery is placed) is considered in this situation.

### 2.2. Power electronics and battery modeling and control

The topology of the power conversion system at which the batteries are connected to, is presented in **Figure 6**. As can be observed, each battery pack is connected to a dedicated H-bridge dc-dc converter which in turn, is connected to a single dc-link. Then, a three-phase H-bridge inverter interfaces with the external ac grid. This topology is flexible in the sense that different battery packs with diverse voltage and current ratings can be integrated. In the same

manner, it presents a good reliability since the system can still be operative in case one of the packs fails.

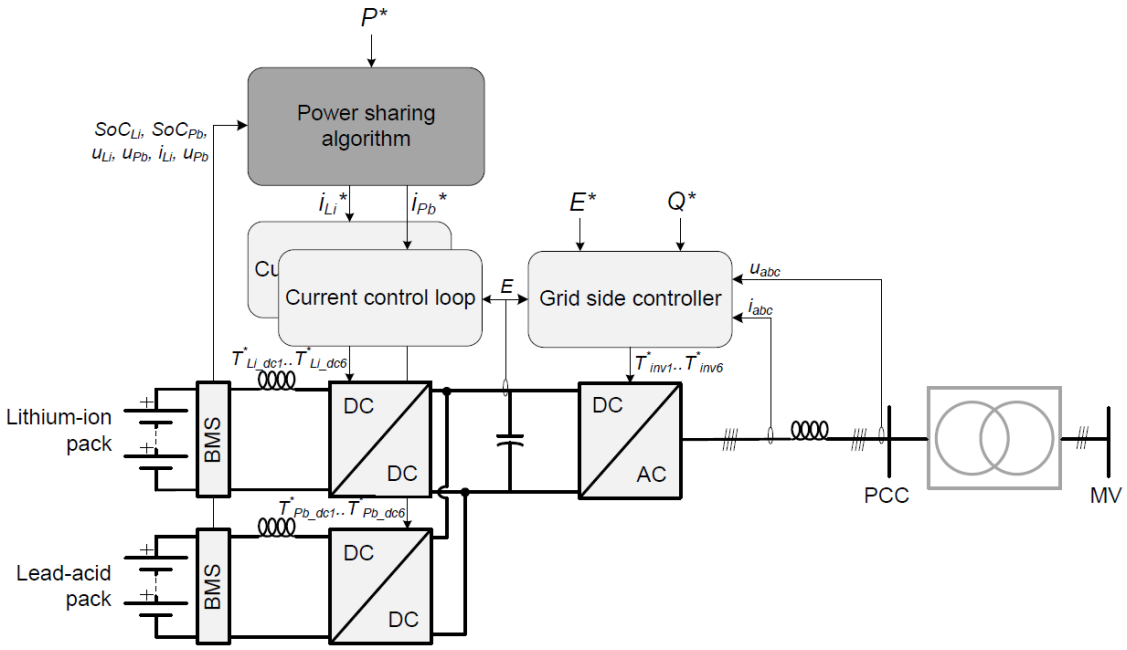


**Figure 6**. The hybrid energy storage solution (the PED) managed by the power sharing algorithm (PSA).

### 2.2.1.Battery modeling

There are different options in literature to model batteries. A review of model types can be found in [1]. Models can be classified into electrochemical, analytical, stochastic and electrical circuit based ones. Each type can represent to a greater or lesser extent specific phenomena in batteries. For instance, the impact in battery performance of state of charge (SOC) levels, energy capacity variations, temperature and aging. The model types usually included in commercial battery management systems (BMSs) are those based on equivalent electrical circuits. These models permit to reproduce voltage and current characteristics for batteries, and also their dynamic responses while charging and discharging. To do so, such models are based on controllable voltage and current sources, in combination with passive components like resistances, capacitors and inductors. See in **Figure 7** a summary of battery models.

For the purposes of BMSs, one straightforward (and useful) approach to model batteries is adopting the so-called "simple model". This is an equivalent circuit-based model based on a voltage source in series to a resistance. A description of this model can be found in [2].

Following contents presents the basis for the "simple model", as well as for other eligible approaches for the purposes of the present project.

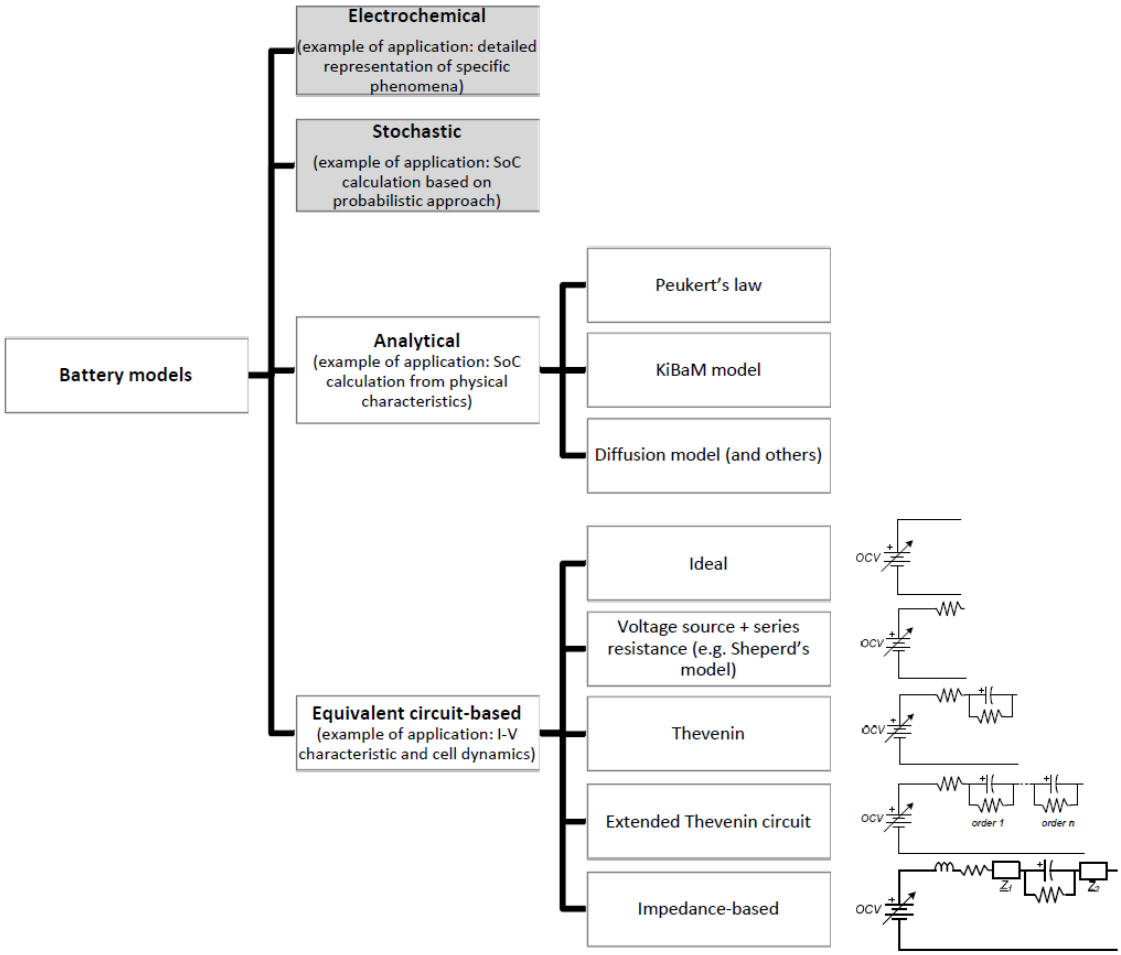


**Figure 7**. Summary of battery models.

#### 2.2.1.1. Simple battery model

The equivalent circuit of the simple model is presented in **Figure 8**. The internal resistance of the battery is represented in the circuit by two resistances $R_c$ and $R_d$ so as to depict the slight variation of it while charging and discharging. Accordingly, to drive the current through either one or the another resistance, each is integrated in the circuit by a diode.

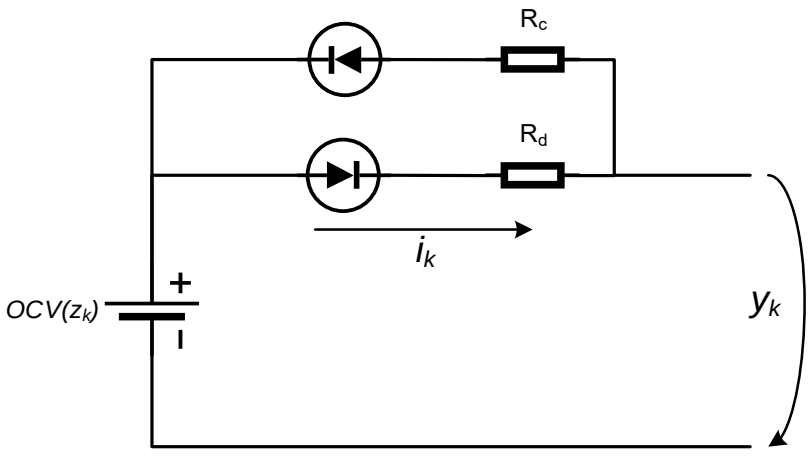


**Figure 8**. Adopted equivalent circuit for modelling a battery.

The magnitude of resistances $R_d$ and $R_c$ can be obtained by testing the battery or directly from the information provided by the manufacturer. The same applies to the voltage source $OCV(soc_t)$.

This voltage source depicts the open circuit voltage of the battery while in rest conditions. The magnitude for this voltage depends on the SOC: the higher the SOC for a battery, the higher the open circuit voltage.

At the end, the sum of the voltage $OCV(soc_t)$ and the voltage drop at the internal resistance yields the voltage at the terminals of the battery $y_t$, so

$$y_t = OCV(soc_t) - R \cdot i_t \tag{4}$$

and $R$ should be considered as $R_d$ while discharging; $R_c$ while charging. Positive current is intended for **discharging**. To compute this equation, it is necessary to previously calculate $OCV(soc_t)$. This correspondence between the open circuit voltage of the battery and the SOC is usually reflected into a lookup table that can be programmed easily in BMS devices. In turn, the SOC for a battery can be computed using the Coulomb counting method, which can be formulated as,

$$soc_{t+1} = soc_t - \left(\frac{\eta_i \cdot \Delta t}{C_n}\right) \cdot i_t \tag{5}$$

where $\eta_i$ is the columbic efficiency (usually set as 1 for lithium-ion), $\Delta t$ the time step for computation, $C_n$ the rated capacity of the battery in Ah and $i_t$ the exchanged current, in A, at time step $t$. At the end, $soc_t$ results expressed in per unit values.

Through recurrent computation of equations (1) and (2), the BMS calculates the battery voltage and SOC. However, prior implementation of equations in the BMS, the parameters should be calculated. A rough estimation of $C_n$ and $R_d$ and $R_c$ can be obtained from datasheets. To improve the accuracy (and then the performance of the BMS while estimating battery state) an **identification procedure** should be carried out though. This procedure is based on a test of the battery before its utilization on field. Such identification procedure is depicted in Annex 2.

#### 2.2.1.2. Zero-hysteresis battery model

As depicted in equation (1), the battery voltage just depends on the open circuit voltage $OCV(soc_t)$ and the voltage drop because of the internal resistance. However, such voltage drop does not only depend on the current flowing through the battery, but on its "stress". After a charge or discharge process, the battery needs some time to relax and recover a voltage $y_k$ very similar, but not equal, to the open circuit voltage $OCV(soc_t)$. It happens, in fact, that following a discharge, the battery voltage relaxes to a value slightly lower than $OCV(soc_t)$. On the other way round, following a charge, the battery relaxes to a value slightly higher than $OCV(soc_t)$.

These phenomena can be actually represented by a hysteresis. Such hysteresis is not actually represented in the previous model.

As a result, the equation yielding the battery voltage for the zero-hysteresis model is

$$y_t = OCV(soc_t) - R \cdot i_t - s_t \cdot M(soc_t) \tag{6}$$

where $s_t$ is a function representing the sign of the current and depends on parameter $\varepsilon$, small and positive. Then,

$$s_t = \begin{cases} 1, & i_t > \varepsilon \\ -1, & i_t < -\varepsilon \\ s_{t-1}, & |i_t| \leq \varepsilon \end{cases} \tag{7}$$

Function $M(soc_t)$ is half the difference between such $OCV(soc_t)$ while computing it from charge and discharge curves. In practice, we consider $M$ as a constant parameter, not a function of the State of Charge.

Then, for state of charge calculation, variable $soc_t$, the same equation (2) utilized for the simple battery model can be adopted.

#### 2.2.1.3. Combined battery model

The simple model and the zero-hysteresis one relay in previous (offline) tests, in which the $OCV(soc_t)$ is determined. As a difference, such magnitude is not needed in the so-called combined battery model.

This model is a combination of the well-known Shepherd's model [3], the Unnewehr universal model and the Nernst model [2], [4]. The Shepherd's model is one of the most utilized approaches for representing the averaged dynamic electrical behavior of batteries. As for the simple model, the battery resembles to a voltage source connected to a series resistance. The magnitude of the voltage source varies with the state of charge, as for the simple and zero-hysteresis model. However, as a difference with the simple model, the dependency between the voltage at this voltage source and the state of charge is not programmed as a lookup table or similar, but corresponds to

$$OCV(soc_t) = E_0 - \frac{K_1}{soc_t} \tag{8}$$

As a result, the battery terminal voltage is given by

$$y_t = E_0 - \frac{K_1}{soc_t} - R \cdot i_t \tag{9}$$

The approach proposed by Unnewehr's universal model is quite similar for the one in Shepherd's model, as noted below

$$y_t = E_0 - K_1 \cdot soc_t - R \cdot i_t \tag{10}$$

The way the open circuit voltage for the battery is calculated is further complicated in Nernst's model, as can be noted in the following expression

$$y_t = E_0 + (K_2 \cdot \ln(soc_t) + K_3 \cdot \ln(1 - soc_t)) - R \cdot i_t \tag{11}$$

At the end, the expression for calculating the battery voltage according to the Combined model becomes

$$y_t = K_0 - (\frac{K_1}{soc_t} + K_2 \cdot soc_t - K_3 \cdot \ln(soc_t) - K_4 \cdot \ln(1 - soc_t)) - R \cdot i_t \tag{12}$$

For state of charge calculation, variable $soc_t$, the same equation (2) utilized for the simple battery model can be adopted.

#### 2.2.1.4. Selection of the battery model for the purposes of the project

All three models presented so far, can effectively represent state-of-charge and terminal voltage variations for the batteries to be included in the PED. Simple model can be included in a simulation environment in a straightforward manner, and this also applies to the Zero-hysteresis model and the Combined one. So, in terms of computational effort, all three alternatives are perfectly eligible.

The main difference is in terms of parameter identification. The Simple model just accounts on 2 parameters, while there are 3 parameters to identify adopting the Zero-hysteresis option, and 7 for the Combined model.

The parameters identification procedure relays on the application of the least-squares estimation theory [5]. The idea is to compare the response variable of a real system (let's say, the terminal voltage of a battery), with the estimated response by a model $Y$. The quadratic error between these two magnitudes is to be minimized applying this theory. The optimal solution, i.e. the one with minimum error, is the one provided by a particular set of $X$ parameters of the model. This set

contains the value for the parameters of the model being adjusted. A detailed description of the least-squares estimation is offered in the Annex 2.

For the application of the least-squares estimation technique, the batteries should be tested and the terminal voltage and the current profiles should be saved. Then, these are utilized in the parameters estimation procedure. In such test, periods in which the battery is relaxed and others when the battery is driving current should be considered. Thus, results would provide information for characterizing the open circuit voltage for different state of charge, and also for characterizing the internal resistance, and hysteresis-related phenomena as well. What is usually applied to this end, is a train of charge and discharge current pulses for the battery, distributed in time between periods for the battery to relax.

The test data are obtained from a public database [6] and corresponds to a lithium-ion cell (INR 18650-20R model). This is a cylindrical, 18650 standard type, similar to the ones actually building the lithium-ion battery pack to be integrated into the PED. Since considering such exemplary test as the common basis for adjusting the parameters of battery models, their performance can be fairly assessed. The input data are plotted in **Figure 9**. Orange and blue lines clearly plot the charge and discharge train of current pulses. As a consequence of such charge and discharge processes, the voltage of the cell (and thus the state of charge) varies in time (see purple and yellow lines). The relaxation of the cell can be clearly appreciated between current pulses. The voltage measured while the battery is relaxed, serves to compute the open circuit voltage characteristic as function of state of charge: variable $OCV(soc_t)$ in the battery models.

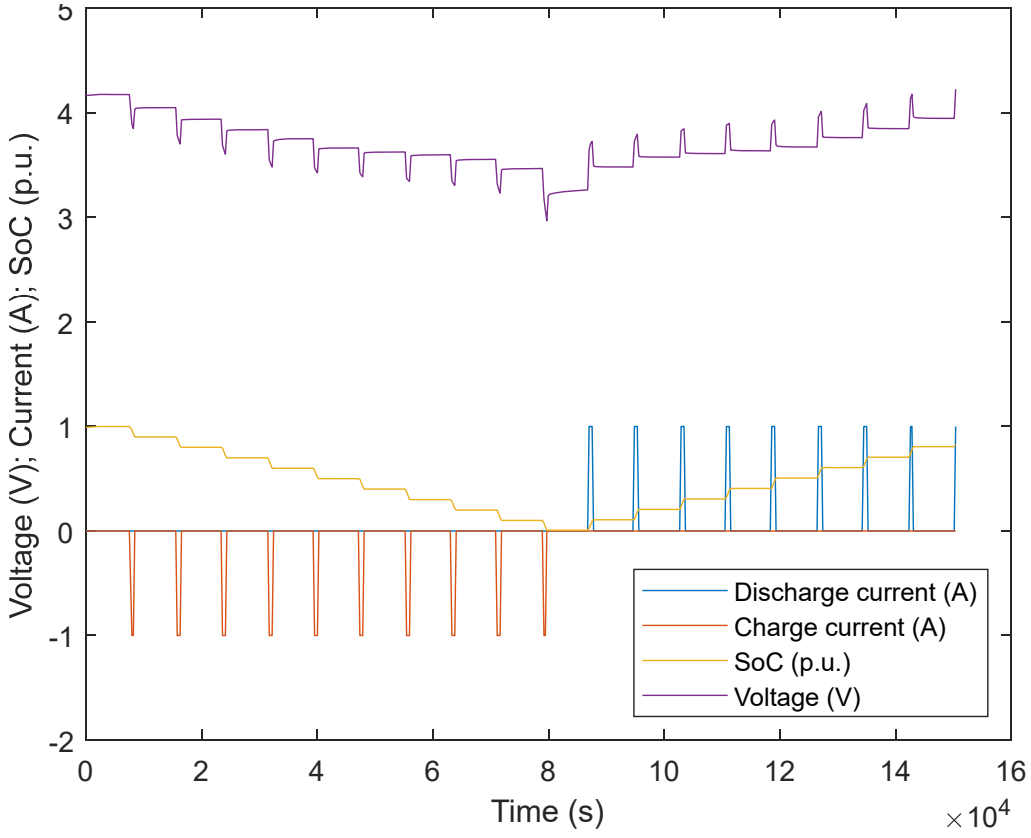


**Figure 9**. Input data for estimation of model parameters (least-squares estimation method) and comparing their performance.

**Table 1** depicts a summary of the parameters found through the application of the least-squares estimation method for each battery model.

| Model | Parameter | Value |
|---|---|---|

| | | |
|---|---|---|
| **Simple** | Charge resistance, $R_c$ | 0.2430 Ohm |
| | Discharge resistance, $R_d$ | 0.2648 Ohm |
| **Zero-hysteresis** | Charge resistance, $R_c$ | 0.2411 Ohm |
| | Discharge resistance, $R_d$ | 0.2629 Ohm |
| | Hysteresis parameter, $H$ | 0.0019 V |
| **Combined** | Charge resistance, $R_c$ | 0.2531 Ohm |
| | Discharge resistance, $R_d$ | 0.2561 Ohm |
| | $K_0$ | 3.2290 V |
| | $K_1$ | 0.0030 V |
| | $K_2$ | -0.8030 V |
| | $K_3$ | -0.0908 V |
| | $K_4$ | -0.0249 V |

**Table 1**. Adjusted parameters for the 3 models applying the least-squares estimation method and adopting the exemplary test data in **Figure 9**.

Now, applying the parameters in **Table 1**, simulation results for all three battery models are compared in **Figure 10**. As can be observed, the performance of all three models is quite similar while calculating the cell voltage (blue line). To better evaluate the difference among all three models, **Figure 11** zooms the "Area A" in **Figure 10**.

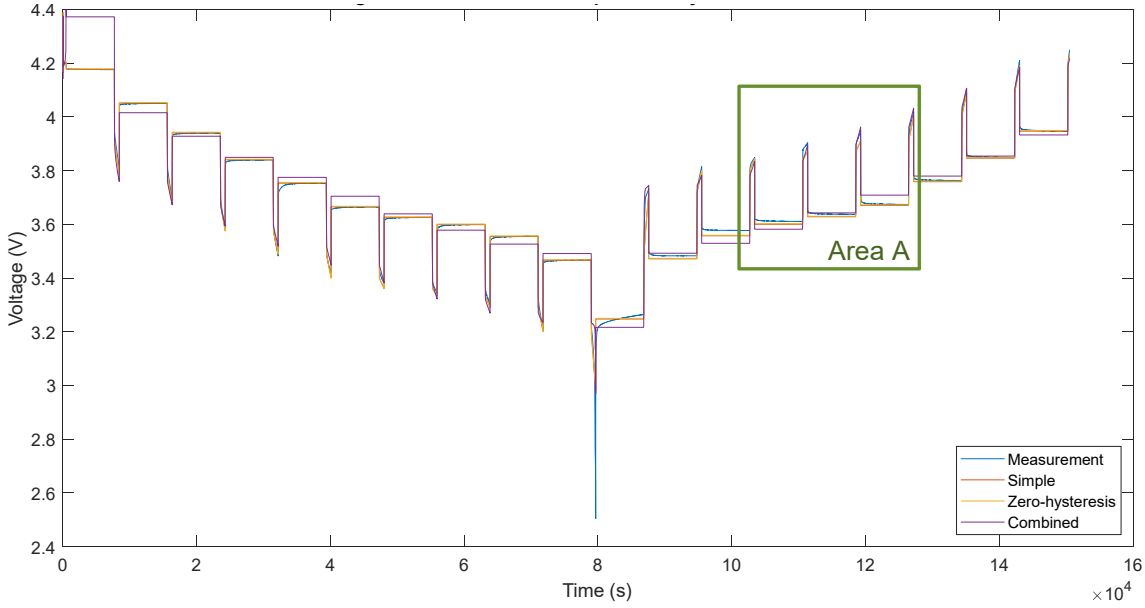


**Figure 10**. Simulation results for all three battery models (Simple, Zero-hysteresis and Combined), and test data (blue line).

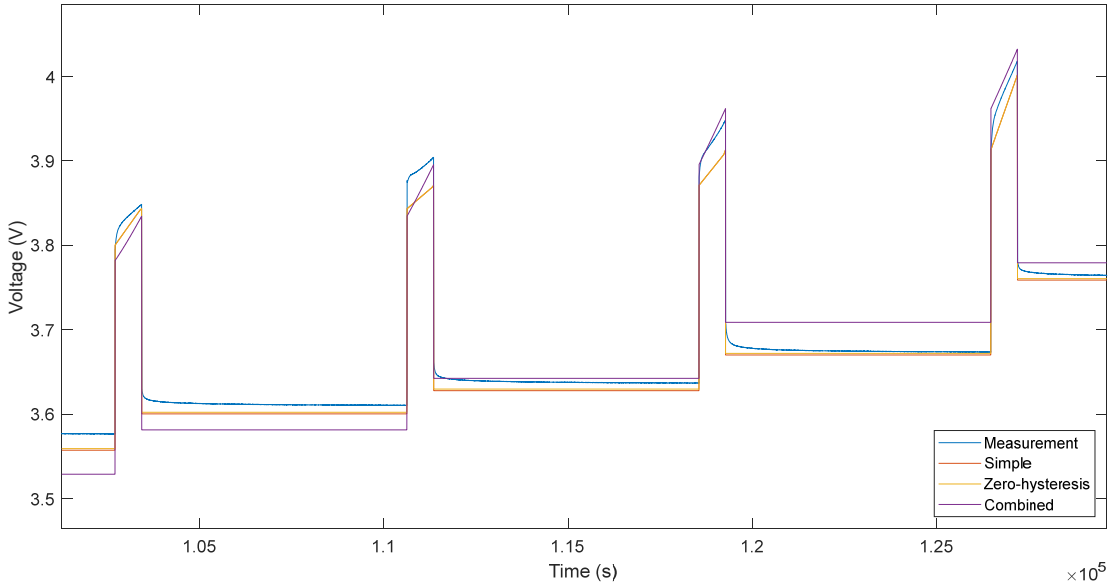


**Figure 11**. Simulation results for all three battery models (Simple, Zero-hysteresis and Combined), and test data (blue line). Detail of **Area A** in **Figure 10**.

The root mean square error between the simulated profile for each battery model and the test data in **Figure 9** are presented in **Table 2**.

| Model | Root Mean Square Error |
|---|---|
| **Simple** | 0.0146 p.u. |
| **Zero-hysteresis** | 0.0144 p.u. |
| **Combined** | 0.0291 p.u. |

**Table 2**. Adjusted parameters for the 3 models applying the least-squares estimation method and adopting the exemplary test data in **Figure 9**.

As can be noted, the best adjustment is achieved through the Zero-hysteresis model, while the poorest is reported for the Combined one.

The Simple model, despite relaying on just 2 parameters ($R_c$ and $R_d$), offers a performance almost as good as for the Zero-hysteresis model, which relays on 3 parameters ($R_c$, $R_d$ and $M$). For this reason, the battery model selected for the purposes of this project is the **Simple model**.

### 2.2.2.Front-end grid inverter modeling and control

The three-phase inverter is modelled as an ideal voltage source. For its modelling and control purposes, it is preferable not to consider time varying magnitudes, so ac voltages and currents are not treated as seen from a stationary frame, but from a rotating reference with grid frequency. This way, such magnitudes are seen as constant in time. To do so, the *qd0* Park's transformation is utilized [7]. In short, Park's transformation permit to represent the three sinusoidal waveforms for the current and voltage of a three phase system, as mainly two vectors in the Gaussian plane at 90º. These two vectors are stationary, and from their magnitude and phase, all information to the corresponding sinusoidal waveforms can be derived. Thus, the application of this transformation reduces the computational effort for the model, since not dealing with sinusoidal waveforms anymore. The result of such exercise can be consulted in [1].

Adopting such mathematics, the tuning of the control system of the front-end grid inverter can be easily solved. The aim of such controller, as can be noted in **Figure 6**, is to manage the reactive power $Q$ exchanged with the main grid and to maintain constant the dc-link voltage $E$ for the

proper operation of the dc-dc modules. This controller is solved through a set of two PI control loops in cascade. The inner control loop manages the instantaneous currents exchanged with the grid expressed in the Park's frame, so in the *qd0* reference. In turn, the active current set-point is provided by an outer control loop keeping the voltage $E$ as constant.

For the sake of completeness, the expressions for the calculation of the parameters of the above explained PI control loops are introduced in the following. For the current control loops, it reads,

$$K_{iqd} = \frac{R}{\lambda} \tag{13}$$

$$K_{pqd} = \frac{L}{\lambda} \tag{14}$$

where $K_{iqd}$ is the integral term and $K_{pqd}$ is the proportional one. The parameter $L$ is the grid inductance, and $R$ its phase resistance. The parameter $\lambda$ is a time constant to be determined by the designer.

Similarly, for the dc-link voltage control loop, it reads,

$$K_{iE} = \frac{2 \cdot C \cdot \omega^2}{3 \cdot k} \tag{15}$$

$$K_{pE} = \frac{4 \cdot C \cdot \varepsilon \cdot \omega}{3 \cdot k} \tag{16}$$

where $C$ is the dc-link capacitance, $\omega$ the oscillation frequency of the desired time response of the controller, and $\varepsilon$ the associated damping coefficient.

### 2.2.3.DC-DC converters modeling and control

The dc-dc power modules actually manage the charging and discharging processes of batteries. So as to provide wide voltage operating range and protection against short-circuits, H-bridge modules are considered in this work. The operating principle of H-bridge modules while operated as dc-dc conversion blocks is explained extensively in literature, as for instance in [8]. In the present work, the average voltage synthetized at the battery side $V_0$, as a result of the application of PWM techniques, is

$$V_0 = E \cdot (2 \cdot D - 1) \tag{17}$$

being $E$ the dc-link voltage, and $D$ the duty cycle for the transistors in the principal diagonal of the H-bridge matrix. So, the charging and discharging of batteries depend on the magnitude of the voltage $V_0$ and this, in turn depends on the applied duty cycle $D$. The duty cycle is solved by a current control loop, as noted in **Figure 6**. Such loop can be realized by a PI controller which tuning procedure can be consulted in state-of-the-art literature [1]. For the sake of completeness, the expressions for the calculation of the PI parameters are

$$K_{idc} = \frac{\omega_{dc}^2 \cdot L_{dc}}{E} \tag{18}$$

$$K_{pE} = \frac{2 \cdot \varepsilon \cdot \omega_{dc} \cdot L_{dc}}{E} \tag{19}$$

where $K_{idc}$ is the integral term and $K_{pdc}$ is the proportional one. The parameter $L_{dc}$ is the inductance interfacing the battery and the dc-dc module. The parameter $\omega_{dc}$ is the oscillation frequency of the desired time response of the controller, and $\varepsilon$ the associated damping coefficient.

# 3. Optimization of the power sharing among the hybrid battery energy storage solution

A hybrid ESS is proposed in the present work. Hybridization is because the ESS combines a heterogeneous grouping of battery types in a single unit. In particular, in this study the hybrid ESS is composed by two different battery types: one based on lithium-ion batteries and the other based on lead-acid ones. The motivation of combining those technologies is due to the fact that the associated investment can be diminished (as a difference with lithium-ion, lead-acid batteries are cheap, so part of storage requirements for the ESS can be fulfilled at low cost). However, the performance of lead-acid batteries is not as good as for lithium-ion in terms of cyclability and efficiency. Thus, optimal operational capability is needed to operate simultaneously and in a complementary way both battery technologies, so the performance of the hybrid ESS as a whole, is not diminished. Such optimal operation is enabled by a novel power sharing algorithm and this is the main contribution of the paper. This algorithm distributes the power demand received by the ESS from the network operation among the battery types embedded in, considering different aspects including the performance and degradation of each type.

The optimization algorithm –the power sharing algorithm, PSA-- is a Non-Linear-Problem (NLP). Input data is introduced in subsection 3.1, decision variables in subsection 3.2, and constraints and function objective in subsection 3.3.

## 3.1. Input data

The input data for the mathematical problem are presented in **Table 3**.

| Item | Description |
|---|---|
| $T$ | Set for time period $T = t_0 \,..\, t_f$. |
| $I$ | Set for battery units $I = i_0 \,..\, i_f$. |
| $P_{r_i}$ | Rated power for battery $i$, in kW. |
| $E_{r_i}$ | Rated energy for battery $i$, in kWh. |
| $P_{tot_t}$ | Power demand for the ESS at time $t$, in kW. |
| $U_t$ | Boolean parameter indicating the sign of $P_{tot_t}$, (1 for positive; 0 otherwise). |
| $\varepsilon$ | Maximum discrepancy between initial and final state of charge for the set of batteries, in kWh |
| $\delta$ | Maximum discrepancy between $P_{tot_t}$ and actual output / input for the ESS, in p.u. |
| $SOC_{max_i}$ | Maximum admissible state of charge for battery $i$, in p.u. |
| $SOC_{min_i}$ | Minimum admissible state of charge for battery $i$, in p.u. |
| $\eta_{in_i}$ | Charging efficiency for battery $i$, in p.u. |
| $\eta_{out_i}$ | Discharging efficiency for battery $i$, in p.u. |
| $C_{p_i}$ | Degradation cost in terms of the power magnitude exchanged by battery $i$, in p.u. |
| $C_{d_i}$ | Degradation cost in terms of depth of discharge experienced by battery $i$, in p.u. |
| $\alpha$ | Weight for optimization objective of minimizing the discrepancy between power demand for the ESS and actual output, in p.u. |
| $\beta$ | Weight for optimization objective of minimizing degradation because of excessive power, in p.u. |
| $\gamma$ | Weight for optimization objective of minimizing degradation because of excessive power ramp, in p.u. |

**Table 3**. Input data for the PSA.

### 3.2. Decision variables

The decision variables for the mathematical problem is divided into sets and parameters, see **Table 4**.

| Item | Description |
|---|---|
| $p_{i,t}$ | Power exchanged by battery $i$ at time $t$, in kW. |
| $e_{in_{i,t}}$ | Energy consumed by battery $i$ at time $t$, in kWh. |
| $e_{out_{i,t}}$ | Energy injected by battery $i$ at time $t$, in kWh. |
| $soc_{i,t}$ | State of charge of battery $i$ at time $t$, in kWh. |

**Table 4**. Decision variables for the PSA.

### 3.3. Problem constraints and objective function

The state of charge for the battery $i$ at time $t$ is expressed in terms of the energy absorbed and injected ($e_{in_{i,t}}$ and $e_{out_{i,t}}$ respectively), and the corresponding charging and discharging efficiencies, $\eta_{in_i}$ and $\eta_{out_i}$. Thus,

$$soc_{i,t} - soc_{i,t-1} = e_{in_{i,t}} \cdot \eta_{in_i} - e_{out_{i,t}}/\eta_{out_i} \tag{20}$$

and $soc_{i,t}$ should be maintained within predetermined limits, so

$$soc_{i,t} \leq SOC_{max_i} \cdot E_{r_i} \qquad \forall_i \in I\,, t \in T \tag{21}$$

$$soc_{i,t} \geq SOC_{min_i} \cdot E_{r_i} \qquad \forall_i \in I\,, t \in T \tag{22}$$

From the energy charged and discharged for the battery $i$ at time $t$, the associated average power $p_{i,t}$ developed in this time step can be derived as

$$p_{i,t} \cdot T_s = e_{in_{i,t}} - e_{out_{i,t}} \qquad \forall_i \in I\,, t \in T \tag{23}$$

Power $p_{i,t}$ should not exceed the ratings for each battery $i$. This is represented as

$$e_{in_{i,t}} + e_{out_{i,t}} \leq p_{r_i} \cdot T_s \qquad \forall_i \in I\,, t \in T \tag{24}$$

Then, constraint (22) ensures that the sign for the power developed by battery $i$ at time $t$ is coherent with that for the power set-point $P_{tot_t}$,

$$e_{in_{i,t}} + e_{out_{i,t}} \leq p_{r_i} \cdot T_s \qquad \forall_i \in I\,, t \in T \tag{25}$$

Constraint (23) avoids the simultaneous changing and discharging for a battery,

$$e_{in_{i,t}} \cdot e_{out_{i,t}} = 0 \qquad \forall_i \in I\,, t \in T \tag{26}$$

In addition, the power exchanged by the set of batteries at time $t$ should be similar to the setpoint $P_{tot_t}$. A margin is provided though, because the ESS should have some flexibility to adjust their output so it can compensate power losses. Such flexibility is represented by an admissible error to $P_{tot_t}$, expressed by parameter $\delta$,

$$\delta \cdot U_t \cdot P_{tot_t} \geq U_t \cdot \left(P_{tot_t} - \sum_i p_{i,t}\right) \qquad \forall_t \in T \tag{27}$$

$$-\delta \cdot U_t \cdot P_{tot_t} \leq U_t \cdot \left(P_{tot_t} - \sum_i p_{i,t}\right) \qquad \forall_t \in T \tag{28}$$

$$\delta \cdot (1 - U_t) \cdot P_{tot_t} \leq (1 - U_t) \cdot \left(P_{tot_t} - \sum_i p_{i,t}\right) \qquad \forall_t \in T \tag{29}$$

$$-\delta \cdot (1 - U_t) \cdot P_{tot_t} \geq (1 - U_t) \cdot \left(P_{tot_t} - \sum_i p_{i,t}\right) \qquad \forall_t \in T \tag{30}$$

Constraint (28) ensures that the difference between the initial and final state of charge for the set of batteries (in kWh) is almost equal –assuming a small discrepancy represented by parameter $\varepsilon$, in kWh– to the energy balance derived from the power set-point profile for the whole time period of analysis,

$$\left(\sum_i soc_{i,t_f} - \sum_i soc_{i,t_0} - \sum_i P_{tot_t} \cdot T_s\right)^2 \leq \varepsilon \tag{31}$$

Finally, constraints (29) to (31) ensure the non-negativity of variables,

$$soc_{i,t} \geq 0 \qquad \forall_i \in I\,, t \in T \tag{32}$$

$$e_{in_{i,t}} \geq 0 \qquad \forall_i \in I\,, t \in T \tag{33}$$

$$e_{out_{i,t}} \geq 0 \qquad \forall_i \in I\,, t \in T \tag{34}$$

The optimization criteria are two-fold. Firstly, the discrepancy between the power demand for the ESS and the actual power exchanged should be minimized, regardless the power losses. Such discrepancy is quantified by term $z_p$, which is formulated as,

$$z_p = \sum_t \left(\frac{P_{tot\_t} - \sum_i p_{i,t}}{\sum_i P_{r_i}}\right)^2 \tag{35}$$

As can be noted, the square of the difference between $P_{tot_t}$ and $\sum_i p_{i,t}$ is computed in equation (32). This is a strategy to fit the response of the ESS to the power set-point at all times. The second optimization criterion is to operate each of the batteries so the associated degradation can be minimized. This is related to two circumstances: i) the power exchanged; and ii) the depth of discharge. The higher the magnitude of such quantifiers, the higher the degradation for batteries. In general terms, thus, it is advisable to operate batteries as de-rated as possible and performs smoothed power profiles also. The advantage of hybridizing the ESS is to use the lithium-ion battery when answering to high and prolonged power demand; and the lead-acid battery for less stringent power profiles. This way, the degradation for lead-acid battery can be minimized, and the ESS can still provide good dynamic response through the resiliency of lithium-ion battery against degradation.

To penalize the degradation of batteries in terms of power rating, term $z_{d1}$ is included and formulated as,

$$z_{d1} = \sum_{i,t} \left(\frac{p_{i,t}}{P_{r_i}} \cdot C_{p_i}\right)^2 \tag{36}$$

To penalize the degradation of batteries in terms of depth of discharge, term $z_{d2}$ is included in the objective function and formulated as,

$$z_{d2} = \sum_{i,t} \left(\frac{soc_{i,t}}{E_{r_i}} \cdot C_{d_i}\right)^2 \tag{37}$$

At the end, the problem turns into a multi-objective criterion which objective function is,

$$z = \alpha \cdot \frac{z_p}{Z_p^*} + \beta \cdot \frac{z_{d1}}{Z_{d1}^*} + \gamma \cdot \frac{z_{d2}}{Z_{d2}^*} \tag{38}$$

where $\alpha$, $\beta$ and $\gamma$ are weighting factors for each of the optimization criteria, and the sum of all three factors is one. In addition, each of the optimization criterion $z_p$, $z_{d1}$ and $z_{d2}$ are divided by the value it takes $z$ when considering each one as the unique criterion for optimization ($Z_p^*$, $Z_{d1}^*$ and $Z_{d2}^*$ respectively). Thus, each of the optimization criterion can be summed and compared between them.

# 4. Application example for performance evaluation

This section presents a study case for the performance evaluation of the PSA. Two different exercises are carried out. The first one aims to test the PSA while driven by an arbitrary, academic time-dependent power profile set-point. The adoption of such academic power set-point eases the performance evaluation of the PSA while letting the PED to develop a power as close as possible to the demand, while also minimizing batteries degradation. The second exercise aims to test the PSA while driven by a realistic time-dependent power profile set-point. This profile is solved by the power network operator, addressing the needs of the grid for the next 24 hours. This second exercise aims to also reproduce the interaction between the grid scheduling algorithm, carried out by the network operator; and the PSA.

## 4.1. Input data

This section presents the input data for the PSA, stressing in the characteristics of the PED, batteries and power profile set-point.

### 4.1.1. Lithium-ion battery energy ratings and efficiency

**Figure 12** presents the lithium-ion battery pack. This battery, holds around 30 kWh, thus providing the majority of the 44 kWh of storage capacity for the PED. It is a modular solution by the manufacturer FENECON GmbH. It is composed by 9 modules connected in series. Supervising and protecting them, on the top a master BMS is included.


**Figure 12**. Lithium-ion battery pack.

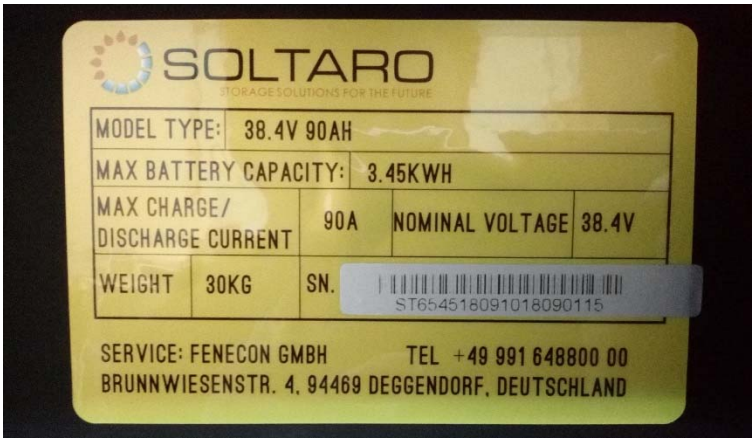


**Figure 13**. Nameplate for one of the 9 modules of the lithium-ion battery pack.

**Figure 13** depicts the nameplate for one of the 9 modules of the lithium-ion battery pack. As can be observed, each of the packs is rated at 38.4 V and 3.45 kWh in energy, thus providing a theoretical rated voltage of about 345.6 V and energy 30.05 kWh. The nominal driving currents are around 90 A. These numbers though, cannot be considered as fully reliable to characterize the parameters of the pack. To do so, these are obtained from laboratory tests. Such tests serve to obtain the actual voltages, energy and efficiency of the pack, and from this information, the parameters of a simulation model (i.e. the open circuit voltage profile and internal resistances) can be obtained.

In particular, and as in an analogous procedure as that presented for characterizing the parameters of a battery model in section 2.2.1, laboratory tests were carried out to charge and discharge the battery pack through a train of current pulses.

The battery is firstly fully discharged, and then a train of charging and discharging current pulses are applied from a minimum SOC equal to 0%, to the maximum practical SOC (100%). **Figure 14** plots such train of current pulses.

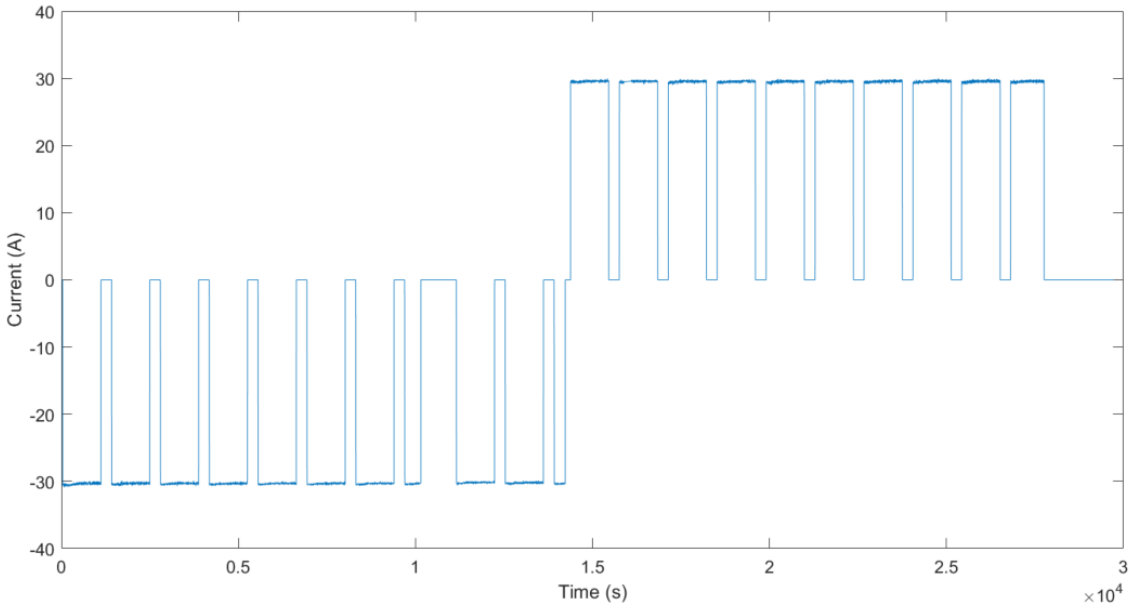


**Figure 14**. Train of current pulses charging (negative values) and discharging (positive values) the battery pack.

This current is provided by a bidirectional voltage source converter (see **Figure 15**). The ratings of this converter are 50 kW in power and up to 800 V dc voltage. At the grid side, the converter can be connected to a three-phase 400 V ac network. The converter communicates with the battery pack through a MODBUS RS485 protocol.

**Figure 15**. Bidirectional voltage source converter utilized for testing the lithium-ion battery pack.

Because of the charging and discharging process, the voltage of the battery varies from the minimum to the maximum voltage and vice-versa. The measured profile, along with the predicted profile by the battery simple model, zero-hysteresis model and the combined one, are plotted in **Figure 16**. The over and under voltage of the battery while driving current can be clearly observed in the voltage profile; also how the voltage varies in the resting periods between pulses. As previously introduced in section 2.2.1, the measurement of the voltage when the battery is relaxed serves to characterize the open circuit voltage of the battery function of the SOC. The over and under voltage of the pack while driving current serves to characterize the charging and discharging resistance.

In **Figure 16**, it can be observed the performance of the different battery models fits with the measured voltage profile (blue line).

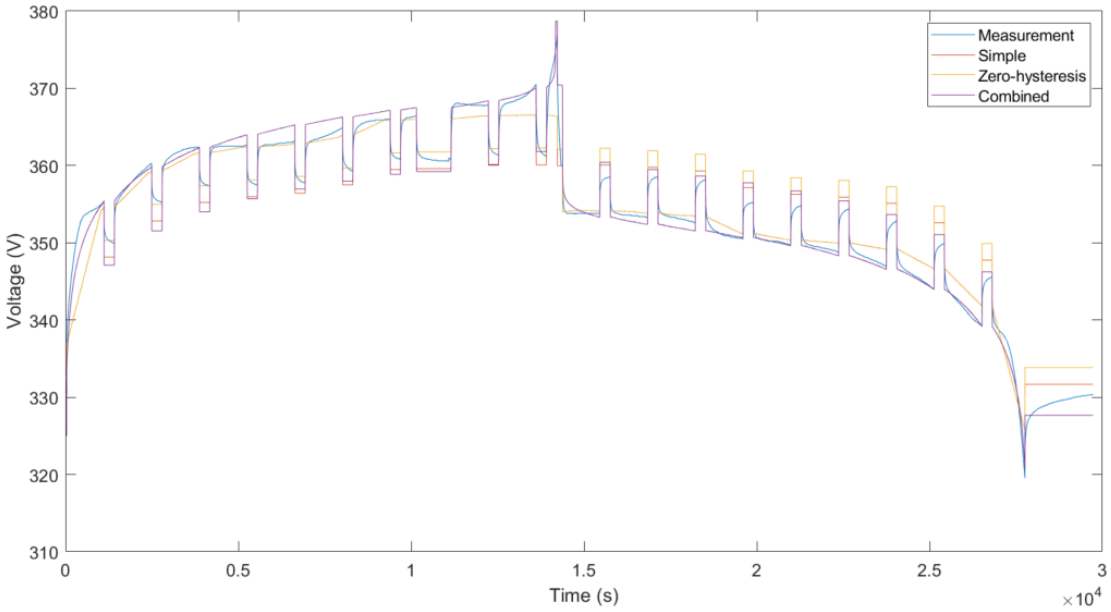


**Figure 16**. Measured battery voltage (blue line), and the predicted profiles by the simple (orange line), zero-hysteresis (yellow line) and combined (purple line) models.

Based on the laboratory tests, the main parameters for the battery to carry out subsequent optimizations and simulations throughout this document to test the PSA, are presented in **Table 5**.

| Item | Description |
|---|---|
| Manufacturer | FENECON |
| Model | C PLUS 25 |
| Nominal capacity and voltage | 87 Ah (C/3); 348 V nominal voltage for the whole pack, 3.2 V per cell. |
| Maximum discharge current | 90 A (1C) |
| Charge resistance, $R_c$ (simple model) | 0.2121 Ohm |
| Discharge resistance, $R_d$ (simple model) | 0.2012 Ohm |
| Discharge temperature | -15 ºC to 50 ºC (25 ºC recommended) |
| Charge temperature | 0 ºC to 40 ºC (25 ºC recommended) |
| Charging current for cycle use | Voltage limits for the whole pack are set between 302 V and 387 V (corresponding to 2.8 V and 3.65 V per cell) |
| Efficiency (round trip) | 94.7% |

**Table 5**.Characteristic parameters for the lithium-ion battery pack based on the information provided by the manufacturer and laboratory tests.

The round trip efficiency $\eta$ has been calculated by

$$\eta = E_{discharge}/E_{charge} \quad (39)$$

where $E_{discharge}$ is the energy provided by the battery while discharging from 100% SOC to 0% SOC. This corresponds to a discharge capacity of 87 Ah. Analogously, $E_{charge}$ is the energy consumed by the battery while charging 87 Ah, so increasing the SOC from 0% to 100%. Based on the tests performed to the battery, $E_{discharged} = 30.32$ kWh and $E_{charged} = 32.03$ kWh, so $\eta = 94.7\%$.

### 4.1.2.Lead-acid battery energy ratings and efficiency

The data characterizing the lead-acid battery pack is directly obtained from the manufacturer. The battery datasheet already includes the results from cycling tests that permit to characterize the capacity and degradation.


**Figure 17**. Ultracell UCG75-12 valve regulated lead-acid battery.

The nameplate characteristics of the battery are firstly presented in **Table 6**.

| Item | Description |
|---|---|
| Manufacturer | Ultracell |
| Model | UCG75-12 |
| Nominal capacity and voltage | 75 Ah (C/10) @ 12 V per battery; 240 V for the whole pack. |
| Maximum discharge current | 900 A |
| Internal resistance | 6.6 mOhm per battery; 0.1320 Ohm for the whole pack (and the resistance of the connectors and wires should be also added)[1]. |
| Discharge temperature | -15 ºC to 50 ºC (25 ºC recommended) |
| Charge temperature | 0 ºC to 40 ºC (25 ºC recommended) |
| Charging current for cycle use | Initial charging current less than 22.5 A. Per battery, final voltage between 14.4 V and 15.0 V at 25 ºC (between 288 V and 300 V for the whole pack). This value is corrected with temperature coefficient -30 mV/ºC |
| Efficiency (round trip) | 91.6%[2] |

**Table 6**.Characteristic parameters for lead-acid battery pack based on the information provided in [13].

The energy storage capacity of the battery depends on the discharge current rates. That is, the higher the discharge current, the lower the energy that can be obtained from a battery. Such dependency is tested by the manufacturer. Results are reproduced in **Figure 18** and **Figure 19**.

[1] The resistance of the connectors and wires has been adjusted to fit with envisaged voltage drop of the battery pack while driving currents when tested.

[2] This efficiency has been derived from the information in the datasheet It was not directly included in there.

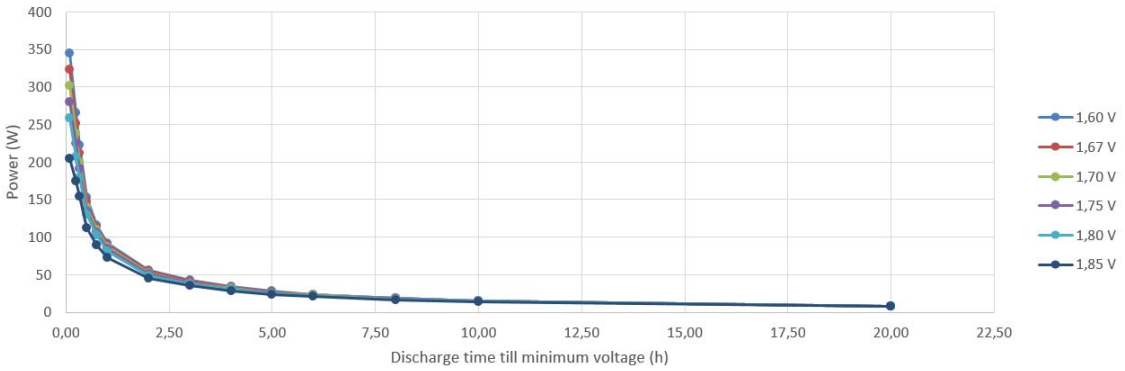


**Figure 18**. Effect of discharge rates in energy storage capacity of the lead-acid battery (I/II).

**Figure 18** presents, in the vertical axis, the power developed by the battery while being discharged, so the discharge velocity. As can be noted, the higher the power developed, the lower the time to get the minimum operating voltage for the cell (so the minimum state of charge).

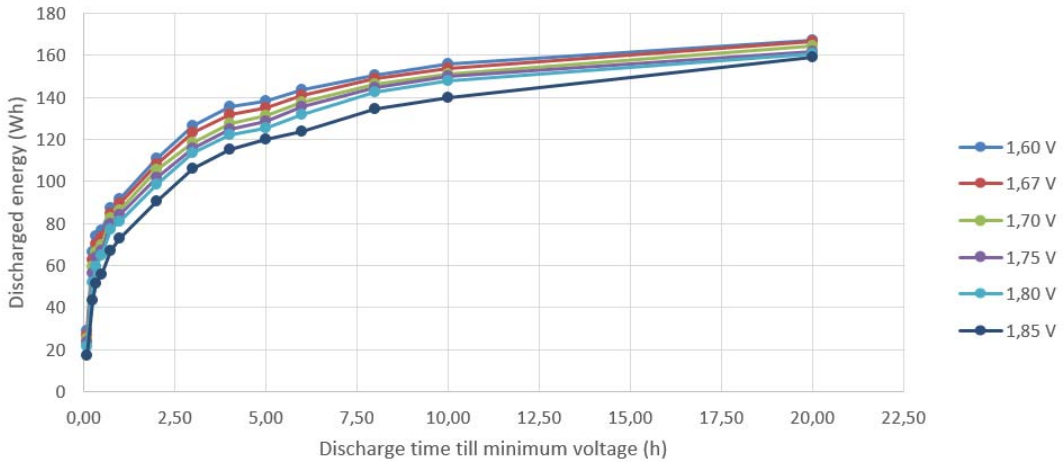


**Figure 19**. Effect of discharge rates in energy storage capacity of the lead-acid battery (II/II).

**Figure 19** clearly shows the dependency of the battery cell with the discharge velocity. As can be noted, the faster the discharge process, the lower the energy (in Wh, vertical axis) that can be extracted from the cell. Various trends are shown, each for a particular minimum operating voltage for the cell.

It is interesting to note that the capacity indicated by the manufacturer in the nameplate of the battery corresponds to a discharge process that takes 10 h (C/10 rate, see **Table 6**). Such slow discharge profile is the one that almost maximizes the storage capacity in **Figure 18**, so the information provided by the manufacturer about the capacity of the battery is very optimistic.

Depending on the service the battery provides, it may be subjected to higher or lower current ratings than C/10, and thus the capacity to be considered so as to estimate state of charge and similar calculations, would not be the one provided by the manufacturer in the nameplate. The designer should select the nominal capacity of the battery that fits best according to the expected current to be exchanged through it. **Table 7** depicts the capacity (in Ah) to consider for different current rates.

| Discharge rate | Capacity and final cell voltage |
|---|---|
| 4.02 A (C/20) | 80.4 Ah ; 1.80 V/cell (10.8 V/battery) |
| 7.50 A (C/10) | 75.0 Ah ; 1.80 V/cell (10.8 V/battery) |
| 13.2 A (C/5) | 65.8 Ah ; 1.75 V/cell (10.5 V/battery) |
| 48.5 A (1C) | 48.5 Ah ; 1.60 V/cell (9.6 V/battery) |

**Table 7**.Capacity of the lead-acid battery depending on the discharge current rate.

### 4.1.3.Calculation of parameters weighting degradation of lead-acid and lithium-ion batteries

There are various factors affecting battery degradation, either for lithium-ion and lead-acid types. Among most important factors, temperature, depth of discharge and current rates are principal ones (Hoke et al. 2011). The literature on battery degradation mechanisms is extensive and in most of the cases refer to particular battery types under heterogeneous test conditions. So it is difficult to derive conclusions that can be generalized to any battery type. Anyhow, and in general terms, from literature it can be concluded that:

- **The higher the depth of discharge, the lower the lifespan of batteries**. This has sense, since high depth of discharge means to utilize most of the active material in battery electrodes for electrochemical reactions and thus, batteries become degraded.
- **The higher the current rate, the lower the lifespan of batteries**. This also has sense, since the higher the current, the higher also the density of electrochemical reactions happening in the electrodes and thus degrading them.

In the present work, battery degradation is going to be associated to the above mentioned factors: depth of discharge and current rates. Temperature is also an important affecting factor [9] for degradation. However, since batteries are to be integrated in a stationary and conditioned environment, this is not to taken into account in this work.

#### 4.1.3.1. Effect of depth of discharge in battery lifespan

**Lead-acid batteries**

The higher the Depth of Discharge, DoD, the shorter the lifespan. From this information, one should derive the degradation parameters $C_{d_i}$ per each of the two battery types in the PED for running the power sharing algorithm (see **Table 3**, section 3.1).

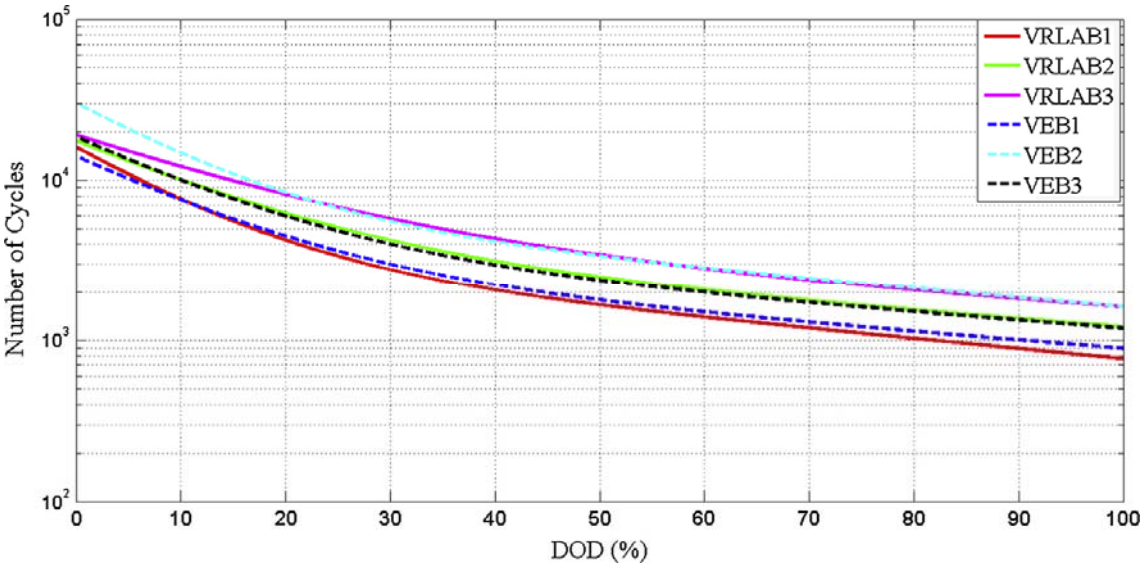


**Figure 20**. Dependency between cyclability and DoD for valve-regulated lead acid batteries. Source: [10]

The effect of DoD on lifespan for lead-acid batteries is properly reported by manufacturers in their datasheets. Cyclability can easily vary in a factor of ten as depicted in **Figure 20**.

A review of the datasheets for the particular battery to be integrated into the PED (battery model UCG75-12 from Ultracell [13]), along with similar ones found in the market yields **Figure 21**. This figure, plots that the larger the depth of discharge, the shorter the life of the battery. Further, such dependency is not linear, but it presents a logarithmic shape.

The data for the particular lead-acid battery type to be integrated in the PED is incorporated in the plot by the blue dotted line. This is directly provided by the battery manufacturer in the corresponding datasheet. As can be observed, the trend for this Ultracell UCG75-12 battery is quite similar to the one reported by other manufacturers.

According to **Figure 21**, it can be concluded that the cyclability of a lead-acid cell typically ranges between 4000 cycles at 20 % DoD and 450 cycles at 100% DoD on average. Life can be multiplied almost by 9 depending on the DoD.

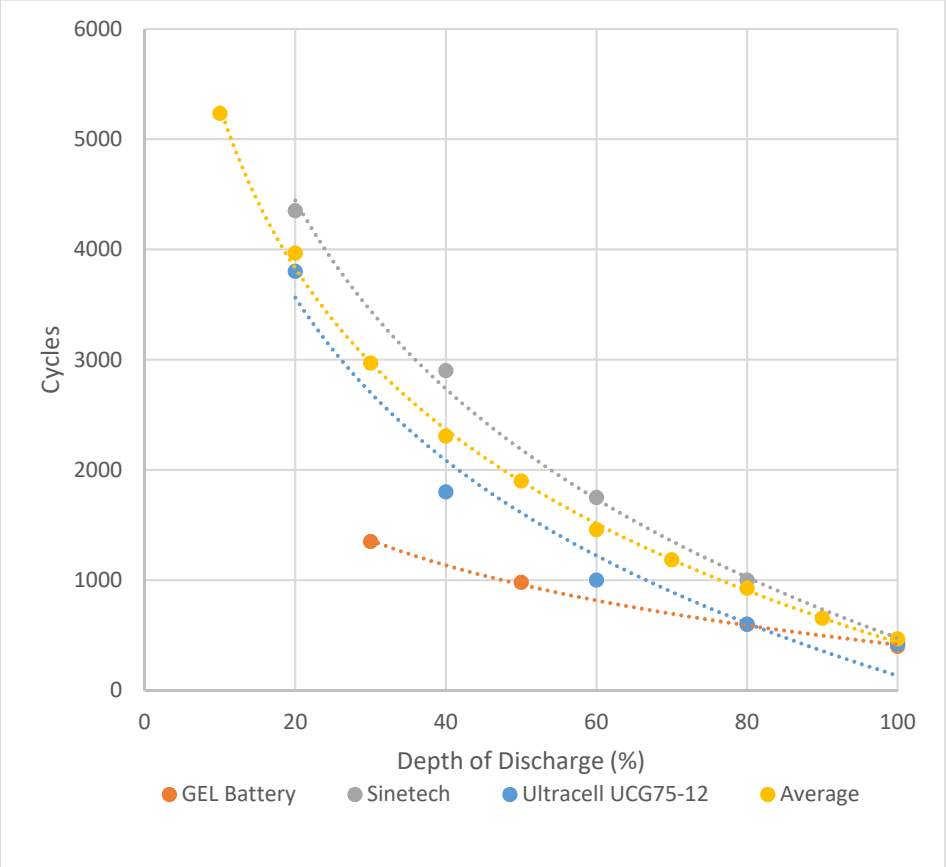


**Figure 21**. Dependency between cyclability and depth of discharge. Tests according to IEC 896-2 (25 ºC). Data for GEL battery: [11]; data for Sinetech battery: [12]; data for Ultracell battery: [13]

### Lithium-ion batteries (lithium-iron-phosphate, LFP type)

For LFP cells, such dependency between DoD and cyclability is not as well reported as for lead-acid batteries. Literature is extensive but it is not straightforward to conclude with clear, tangible and generalizable results.

Anyhow, some works propose similar relationship to that shown in **Figure 21** for lead-acid batteries. This is the case of [14], which output is reproduced in **Figure 22**. As can be observed, the relationship between DoD and cyclability is not linear at all. Cyclability can be greatly improved for very small DoD. For the particular LFP cell considered in **Figure 22**, it can be concluded that cyclability varies between 15000 cycles at 20% DoD and 2000 cycles at 100% DoD. Hence, lifespan can be multiplied by a factor of 7.5 depending on the DoD.

Comparing **Figure 21** with **Figure 22**, we can conclude that the affectation of DoD to LFP lifespan can be lower than for lead-acid batteries. This is totally aligned with the recommendations of manufacturers in regard of the integration of batteries in the particular ends they are aimed to: the minimum recommended SOC for lead-acid batteries is conventionally higher than for lithium-ion batteries.

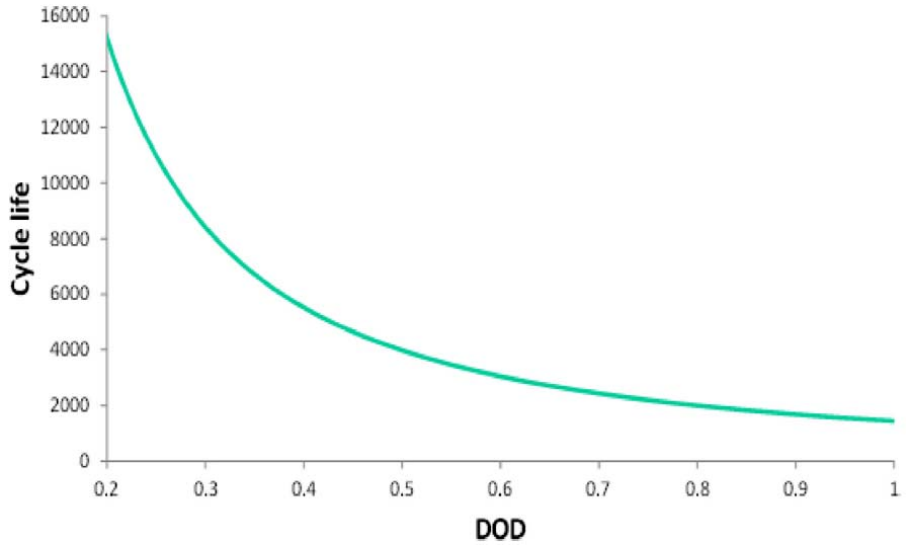


**Figure 22**. Dependency between cyclability and depth of discharge for a lithium-ion battery. Source: [14].

#### 4.1.3.2. Effect of current rates in battery lifespan

**Lead-acid batteries**

The dependency between cyclability and current rates for lead-acid batteries can be assessed from various works in literature. For instance, [15] performed tests on 25 Ah @ 2 V sealed lead-acid batteries to evaluate the influence of various aspects on battery degradation. The authors proposed, as an outcome, mathematical expressions for the degradation correlating the above mentioned aspects. An interesting expression is the one stating that the capacity of the battery, $C$ (in %), varies following the equation $C(\%) = 100 - 0.21 \cdot n - 0.31 \cdot c$, where $n$ is the number of cycles and $c$ is the charging rate, in A.

Hence, the relationship between current rates and degradation is clear. However, it is hard to generalize results since these are different for each lead-acid subtype; even for the same time and different batch. In general terms though, degradation in terms of power charge and discharge rates is considered in the present work as several times higher for lead-acid with respect to lithium-ion. A proof is that manufacturers, in their datasheets, recommend discharge rates are usually around 0.1C or 0.2C (so at 10% or 20% of the nominal design current for the battery) so as to maximize useful life; while this rate can be 0.7C or even 1C for lithium-ion batteries, so around 8 times more on average [16], [17], [18].

**Lithium-ion batteries (lithium-iron-phosphate, LFP type)**

Looking now at the of rate of discharge, for LFP the affectation of current rates can be derived from evaluating the trend in **Figure 23**. Accordingly, lifespan vary between 500 cycles at 10C and 3500 cycles at 1C. So lifespan can be multiplied by a factor of 7 depending on current rates.

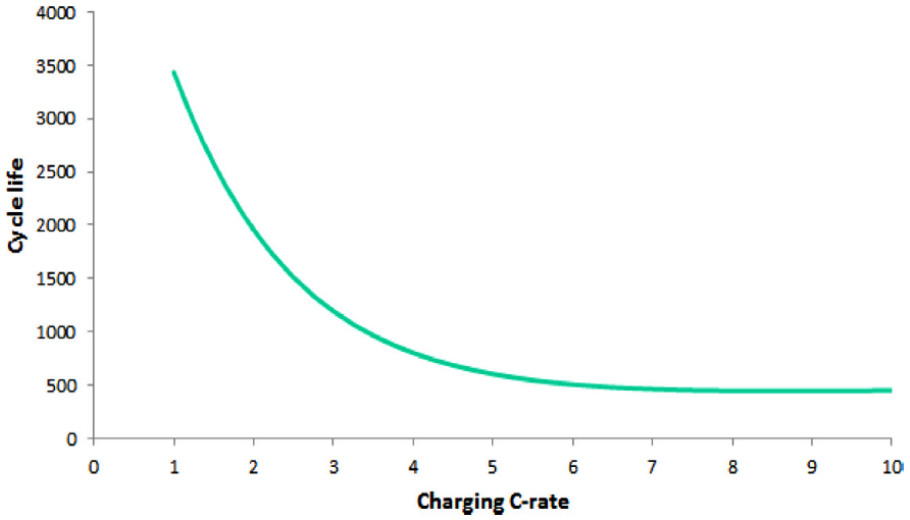


**Figure 23**. Dependency between cyclability and current rates for a lithium-ion battery. Source: [14].

The relationship between life and C-rate is also depicted by (Omar et al. 2014) for LFP cells. The experiments in this case were done at constant current and reaching 100 DoD%. It can be concluded that, for this particular cell, lifespan varies between 559 cycles at 15C, 1100 cycles at 10C and 2900 cycles at 1C. So life is multiplied by a factor of almost 3 between 1C and 10C.

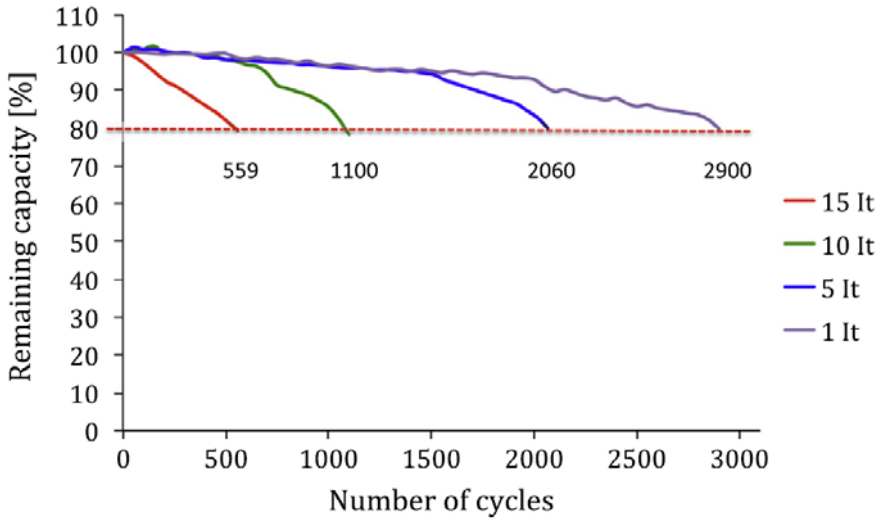


**Figure 24**. Dependency between cyclability and current rates. Source: [19].

### 4.1.4.Power demand from the network for the PED

Two power demand profiles for the PED are to be considered. The first one is step profiled, arbitrarily set by the authors of the present work. Although arbitrary, it serves to clearly evaluate the performance of the PSA while following the demand profile and distributing it among the two battery types for minimum degradation. The reason of considering such academic profile is to evaluate the dynamics of lithium-ion and lead-acid battery pack responses, while not subjected to the variability and randomness of a realistic demand profile for the PED. Such academic demand profile is depicted in **Figure 25**.

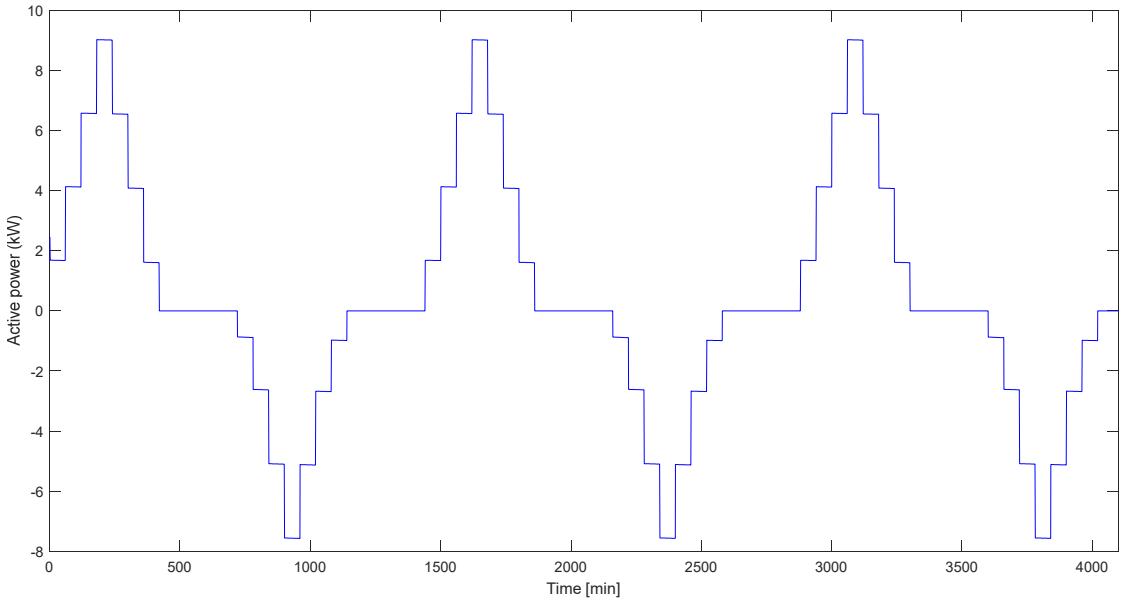


**Figure 25**. Arbitrary demand profile for the PED. The time step is 1 min.

In a second step, the performance of the PSA is to be tested with a realistic demand profile solved by the corresponding management algorithm of the distributor operator (this algorithm is being developed in the work package 3 of RESOLVD project, for more information).

This demand profile is updated in an hourly basis to diminish forecasting errors in the above mentioned management algorithm of the distributor operator. As a result, the PSA is to be also executed in an hourly basis in the PED. Such procedure is detailed in section 4.3.

### 4.2. Optimization results adopting the arbitrary demand profile

The aim of this section is to show the performance of the hybrid energy storage system when being operated under the PSA. The PSA is executed once per hour for determining both lithium-ion and lead-acid batteries power contribution to meet the demand profile while minimizing a multi-objective function. The multi-objective function to be minimized is:

$$z = \alpha \cdot \frac{Z_p}{Z_p^*} + \beta \cdot \frac{Z_{d1}}{Z_{d1}^*} + \gamma \cdot \frac{Z_{d2}}{Z_{d2}^*}$$

The terms $Z_p^*$, $Z_{d1}^*$ and $Z_{d2}^*$ are determined after running 3 optimization problems. The first is to minimize the discrepancy between the power output of the PED and the power scheduling profile ($\alpha = 1, \beta = \gamma = 0$). The corresponding optimal solution is $Z_p^*$. The second is to minimize the degradation cost for the batteries as function of excessive driving currents ($\beta = 1, \alpha = \gamma = 0$). The corresponding optimal solution is $Z_{d1}^*$. The third is to minimize the degradation cost for the batteries as function of excessive depth of discharge ($\gamma = 1, \alpha = \beta = 0$). The corresponding optimal solution is $Z_{d2}^*$. In each of these three optimizations, the input demand power profile is given by 4100 hourly values. The results obtained are depicted in **Figure 26**, **Figure 27** and **Figure 28**, respectively. These three optimization problems are identified as Optimization 1, Optimization 2 and Optimization 3 in **Table 8**.

When running the PSA, equal importance (i.e. same weight) is given to satisfy the demand and to minimize degradation. Therefore, the weights of the objective function have been selected as follows: $\alpha = 0.5, \beta = 0.25, \gamma = 0.25$. The corresponding results are depicted in **Figure 29**.

The plots in each figure (**Figure 26** - **Figure 29**) show, for each battery technology, the power delivered or absorbed at each hour (A), the input energy (B), the output energy (C) and the state of charge (SOC) (D). Battery 1 (blue line) corresponds to the lithium-ion and battery 2 (green line)

corresponds to the lead acid battery. Plot (E) shows the power reference of the PED versus the sum of all the power from the two batteries.

In the plot marked with (A), positive values mean to absorb power from the grid. The lithium-ion battery, since being the one with best performance in terms of efficiency and degradation, is holding most of power demand, both in terms of power magnitude and power ramp. The lead-acid battery, on the other hand, is delivering much lower power for reduced degradation.

In plot marked with (D), the SOC variation to fit the power profile set-point is represented. Most of the energy storage capacity is utilized for the lithium-ion battery. In addition, the state of charge variation presents high ramping, in coherence with the significant power developed in time. Conversely, the lead-acid battery is operated smoothly and within a limited state of charge range.

As shown in the plot marked with (E). while absorbing power, the power profile developed by the ESS mostly fits with the set-point. However, while injecting power to the grid, the output of the ESS is lower than requested. This difference though, is within admissible limits (35%, as set by parameter δ). Such difference is because the batteries need some flexibility to compensate losses: it is not possible to strictly follow the power set-point at all times.

| Optimization function | $z$ value | Computation time (s) |
|---|---|---|
| Optimization 1 | 0.5171 | 132 |
| Optimization 2 | 1.2360 | 104 |
| Optimization 3 | 869.6683 | 85 |
| PSA | 6.4349 | 40.7 |

**Table 8**. Objective function results and computation time to find the solution.

**Table 8** shows the objective function values obtained and computation times required in each optimization problem run (Optimization 1, Optimization 2, Optimization 3 and PSA). It is worth mentioning that the optimization results have been obtained for 4100 demand hourly values, but in practical implementation, only 24 values (one day) will be used as rolling horizon. The computer used to perform the calculations is an Intel i7-8550U CPU @ 180 GHz, 16 GB RAM, with operative system of 64 bits. The solver used is IPOPT.

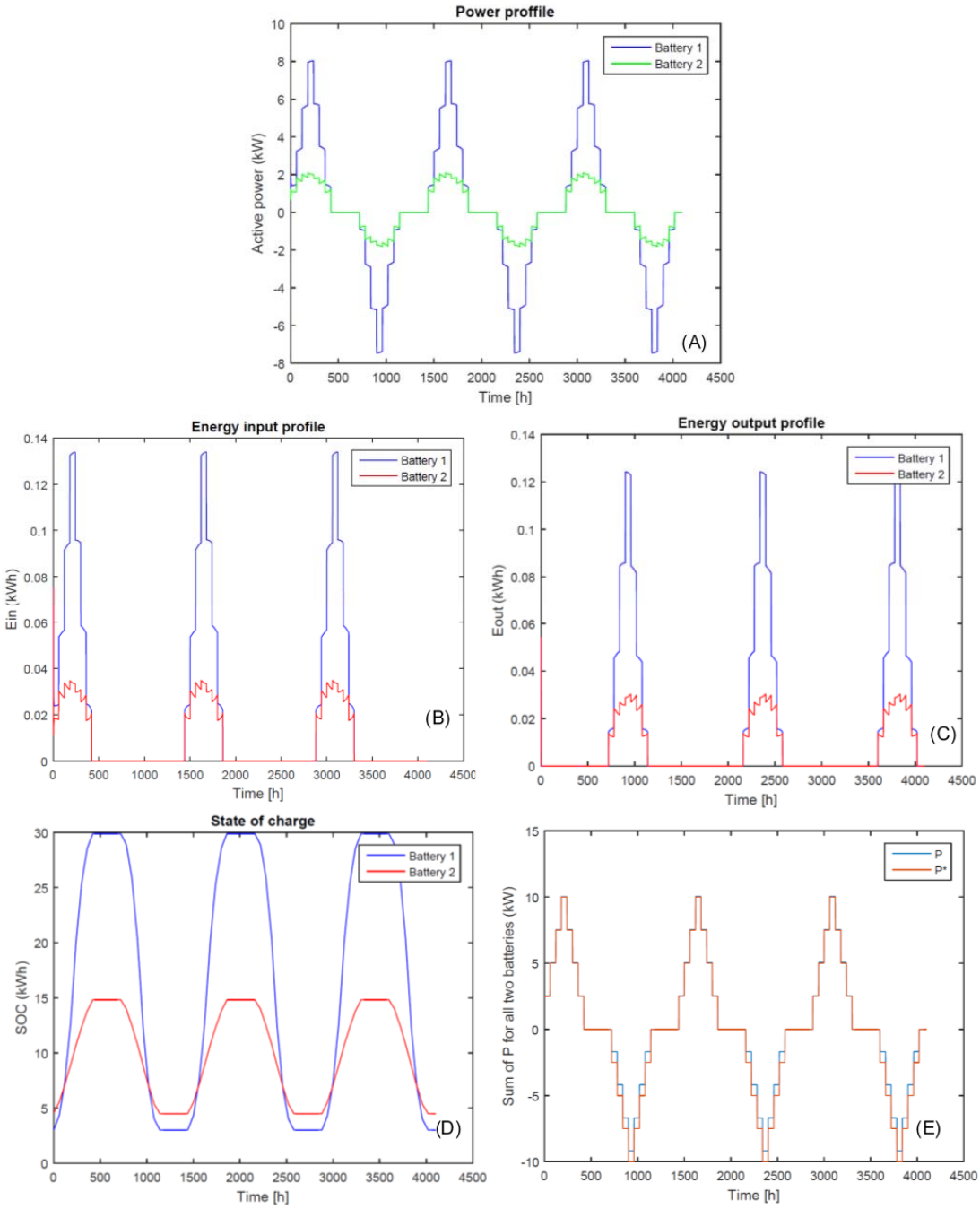


**Figure 26**. Results of the optimization for minimizing the discrepancy between the power output of the PED and the power scheduling profile.

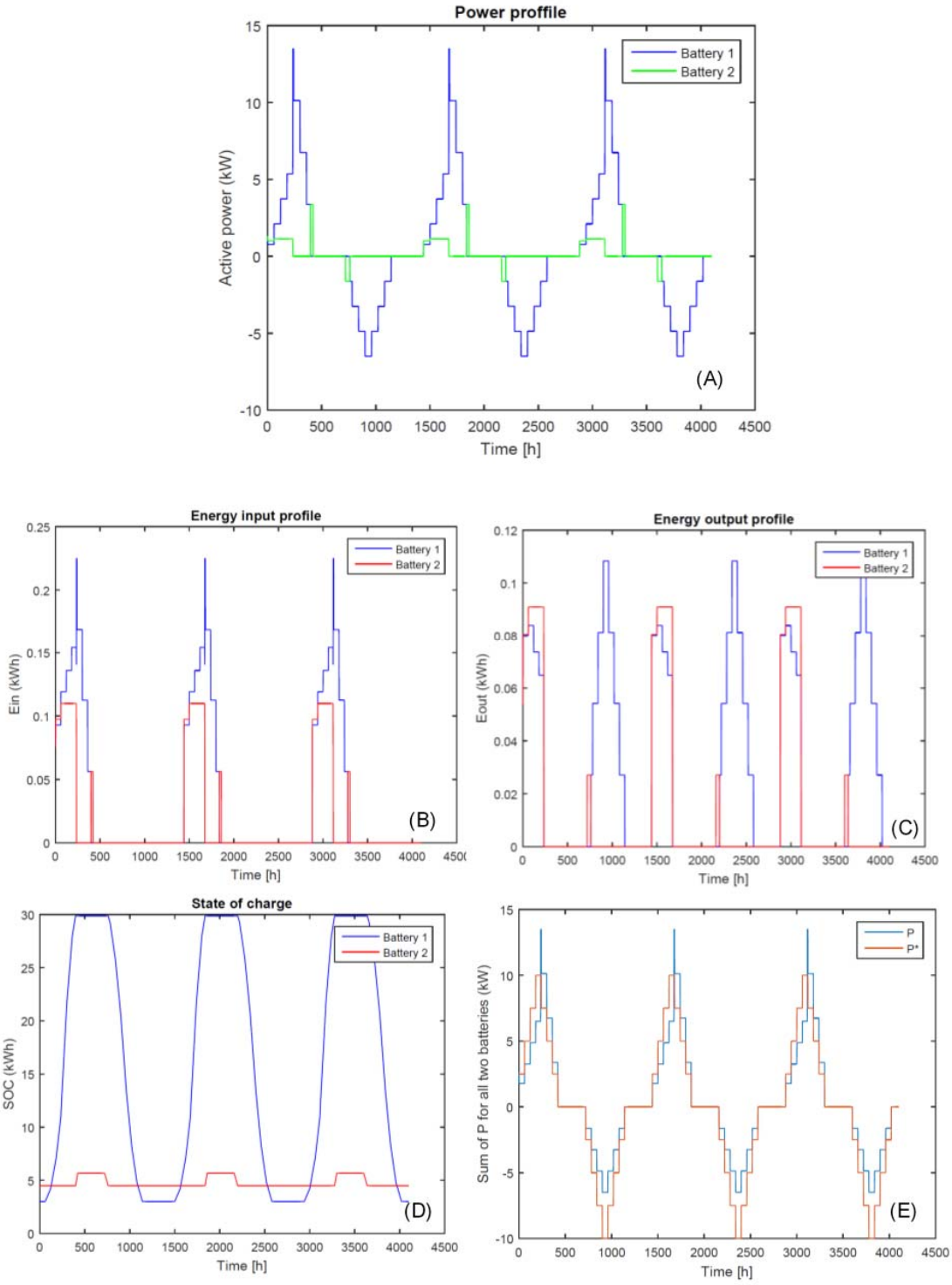


**Figure 27**. Results of the optimization for minimizing the degradation cost for the batteries as function of excessive DoD.

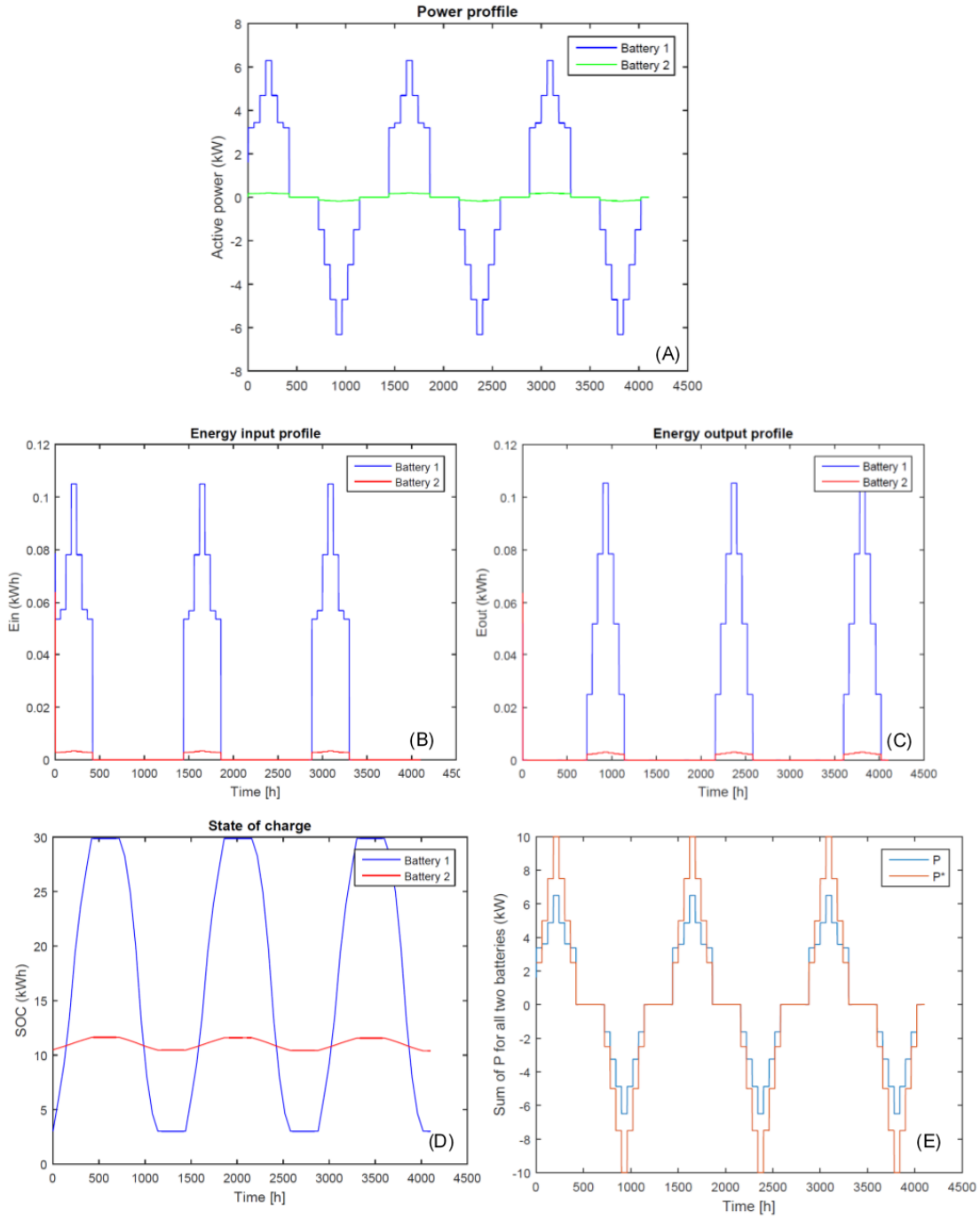


**Figure 28**. Results of the optimization for minimizing the degradation cost for the batteries as function of excessive driving currents.

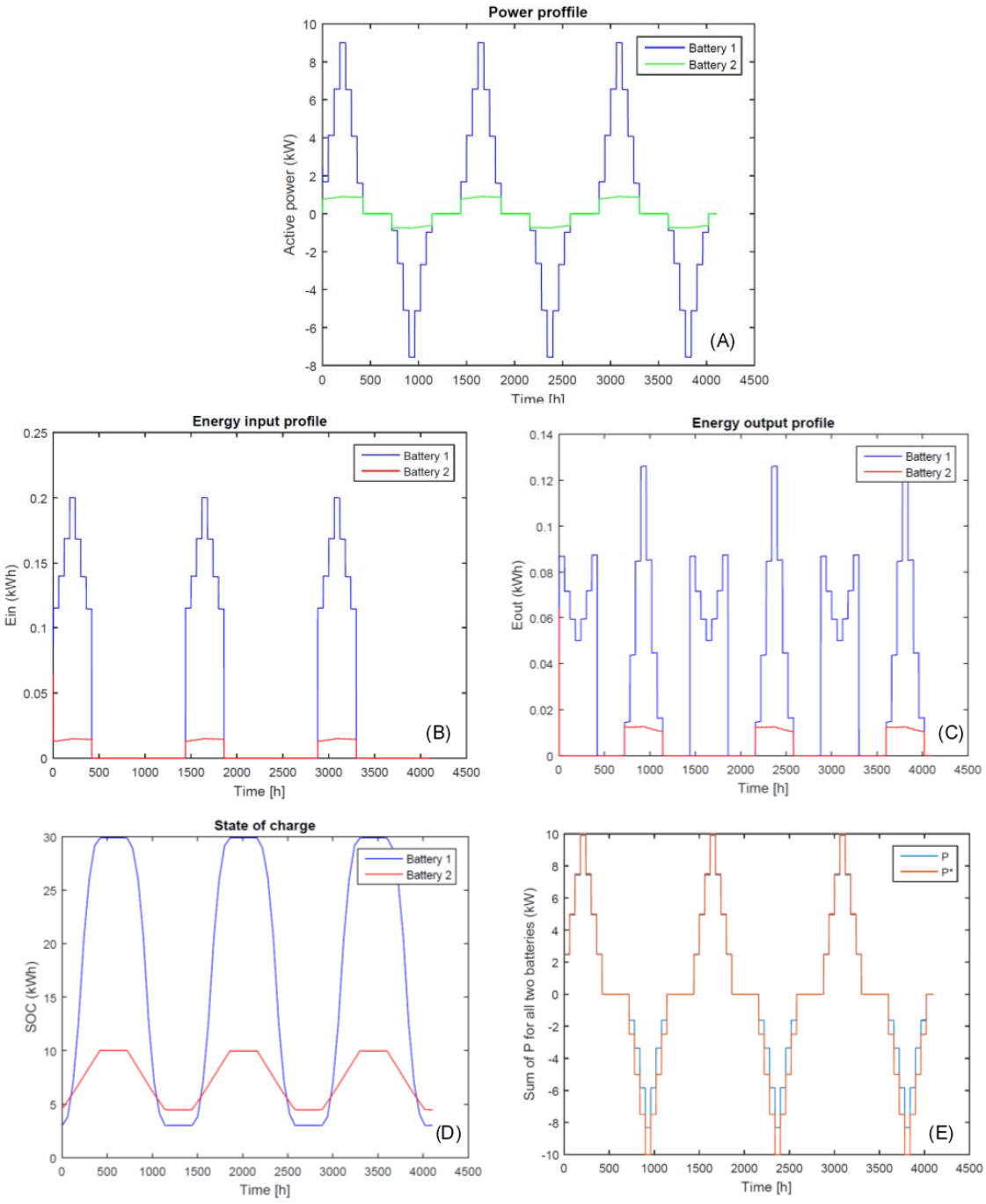


**Figure 29**. Results of the multi-objective optimization for the PSA.

### 4.3. Iterative procedure for performance evaluation

The iterative procedure is done performing the grid "Grid Operation Scheduler" and posteriorly applying the PSA function of forecasts and the estimated state of charge. In order to verify that the estimation of the SOC is right a parallel simulation is carried out to determine the real SOC of batteries.

Therefore, the process is the following and it is depicted in **Figure 30**:

- The first step of this iterative process is the estimation of the future SOC. The partials and averaged SOCs are estimated taking into account the current power set-points and the current SOCs of charge. Note that the partials SOCs corresponds to lithium and lead-acid batteries.
- The second step initializes when the averaged SOC is forecasted. The Grid Operation Scheduler is executed according to the most recent consumption and generation forecasts. Posteriorly, the energy schedule for the next 24 hours is requested to the PED.
- The third step is mainly the power sharing algorithm which takes this energy schedule and tries to optimize it to ensure the requested power and procure to take care of batteries. Finally, it defines how much energy comes from lithium and lead-acid batteries.

Simultaneously, the battery behavior simulation is performed in order to calculate the real SOCs when the batteries perform the requested energy set-points. The results are the point of departure for the estimation of future SOCs. **Figure 30** summarizes the first iterations of the above described procedure.

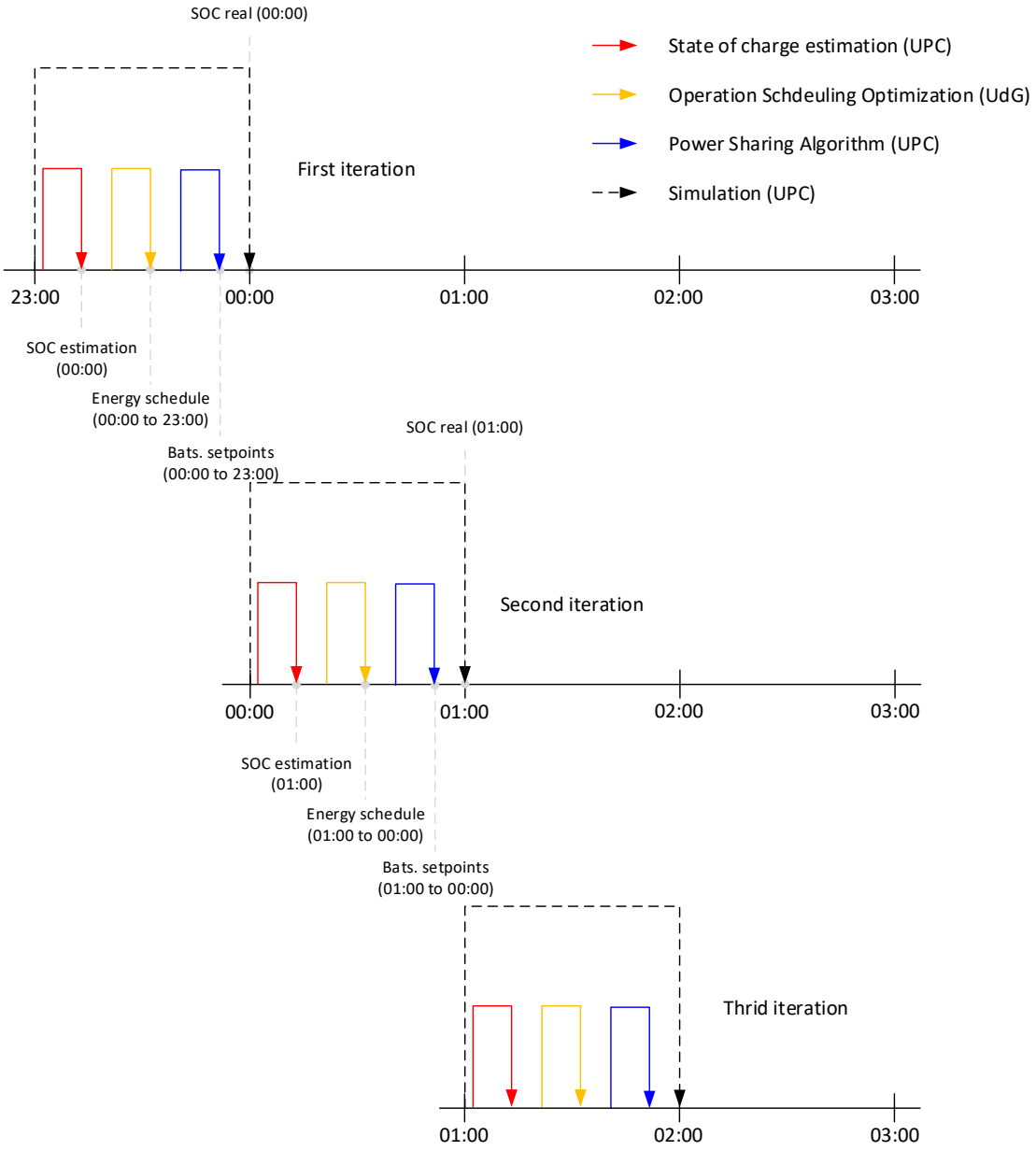


**Figure 30**. Graphical description of the iterative procedure to test the PSA in combination with the grid Grid Operation Scheduler.

In particular, we have done 15 iterations to test the performance of the PSA. A step-by-step description of the calculations performed in each of the iterations are summarized in **Table 9**.

| Iter. | Item | Time | Process | Inputs | Outputs | Results in files |
|---|---|---|---|---|---|---|
| 1 | 0 | 23:20 | SOC estimation by the beginning of next hour | Real SOC at 23:00 h (-1 day) | Estimated SOC at 00:00 h | estimacio.xlsx (iteration_1) |
| | 1 | 23:30 | Grid Operation Scheduler | Real SOC at 00:00 h | P_net*(00:00)<br>…<br>P_net*(23:00) | ESS_schedule.xlsx (iteration_1) |
| | 2 | 23:45 | PSA execution based on grid scheduling | Inputs item 1 + Results item 1 | P_psa*(00:00)<br>…<br>P_psa*(23:00) | iteracio1.mat |
| | 3 | 00:00 | PED simulation to check real behavior | iteracio1.mat | | Real SOC1.mat |

| Iter. | Item | Time | Process | Inputs | Outputs | Results in files |
|---|---|---|---|---|---|---|
| 2 | 4 | 00:20 | SOC estimation by the beginning of next hour | Real SOC at 00:00 h & P_psa*(00:00) | Real SOC(01:00) | estimacio.xlsx (iteration_2) |
| | 5 | 00:30 | Grid Operation Scheduler | Real SOC at 01:00 h | P_net*(01:00) … P_net*(00:00 +1d) | ESS_schedule.xlsx (iteration_2) |
| | 6 | 00:45 | PSA execution based on grid scheduling | Inputs item 5 + Results item 5 | P_psa*(01:00) … P_psa*(00:00 +1d) | iteracio2.mat |
| | 7 | 01:00 | PED simulation to check real behavior | iteracio2.mat | | Real SOC2.mat |
| 3 | 8 | 01:20 | SOC estimation by the beginning of next hour | Real SOC at 01:00 h & P_psa*(01:00) | Real SOC(02:00) | estimacio.xlsx (iteration_3) |
| | 9 | 01:30 | Grid Operation Scheduler | Real SOC at 02:00 h | P_net*(02:00) … P_net*(01:00 +1d) | ESS_schedule.xlsx (iteration_3) |
| | 10 | 01:45 | PSA execution based on grid scheduling | Inputs item 9 + Results item 9 | P_psa*(02:00) … P_psa*(01:00 +1d) | iteracio3.mat |
| | 11 | 02:00 | PED simulation to check real behavior | iteracio3.mat | | Real SOC3.mat |
| 4 | 12 | 02:20 | SOC estimation by the beginning of next hour | Real SOC at 02:00 h & P_psa*(02:00) | Real SOC(03:00) | estimacio.xlsx (iteration_4) |
| | 13 | 02:30 | Grid Operation Scheduler | Real SOC 03:00 h | P_net*(03:00) … P_net*(02:00 +1d) | ESS_schedule.xlsx (iteration_4) |
| | 14 | 02:45 | PSA execution based on grid scheduling | Inputs item 13 + Results item 13 | P_psa*(03:00) … P_psa*(02:00 +1d) | Iteracio4.mat |
| | 15 | 03:00 | PED simulation to check real behavior | Iteracio4.mat | | Real SOC4.mat |
| 5 | 16 | 03:20 | SOC estimation by the beginning of next hour | Real SOC at 03:00 h & P_psa*(03:00) | Real SOC(04:00) | estimacio.xlsx (iteration_5) |
| | 17 | 03:30 | Grid Operation Scheduler | Real SOC at 04:00 h | P_net*(04:00) … P_net*(03:00 +1d) | ESS_schedule.xlsx (iteration_5) |
| | 18 | 03:45 | PSA execution based on grid scheduling | Inputs item 17 + Results item 17 | P_psa*(04:00) … P_psa*(03:00 +1d) | Iteracio5.mat |
| | 19 | 04:00 | PED simulation to check real behavior | Iteracio5.mat | | Real SOC5.mat |
| 6 | 20 | 04:20 | SOC estimation by the beginning of next hour | Real SOC at 04:00 h & P_psa*(04:00) | Real SOC(05:00) | estimacio.xlsx (iteration_6) |
| | 21 | 04:30 | Grid Operation Scheduler | Real SOC at 05:00 h | P_net*(05:00) … P_net*(04:00 +1d) | ESS_schedule.xlsx (iteration_6) |
| | 22 | 04:45 | PSA execution based on grid scheduling | Inputs item 21 + Results item 21 | P_psa*(05:00) … P_psa*(04:00 +1d) | Iteracio6.mat |
| | 23 | 05:00 | PED simulation to check real behavior | Iteracio6.mat | | Real SOC6.mat |
| 7 | 24 | 05:20 | SOC estimation by the beginning of next hour | Real SOC at 05:00 h & P_psa*(05:00) | Real SOC(06:00) | estimacio.xlsx (iteration_7) |
| | 25 | 05:30 | Grid Operation Scheduler | Real SOC 06:00 h | P_net*(06:00) … P_net*(05:00 +1d) | ESS_schedule.xlsx (iteration_7) |
| | 26 | 05:45 | PSA execution based on grid scheduling | Inputs item 25 + Results item 25 | P_psa*(06:00) … P_psa*(05:00 +1d) | Iteracio7.mat |
| | 27 | 06:00 | PED simulation to check real behavior | Iteracio7.mat | | Real SOC7.mat |
| 8 | 28 | 06:20 | SOC estimation by the beginning of next hour | Real SOC at 06:00 h & P_psa*(06:00) | Real SOC(07:00) | estimacio.xlsx (iteration_8) |

| Iter. | Item | Time | Process | Inputs | Outputs | Results in files |
|---|---|---|---|---|---|---|
| | 29 | 06:30 | Grid Operation Scheduler | Real SOC at 07:00 h | P_net*(07:00) … P_net*(06:00 +1d) | ESS_schedule.xlsx (iteration_8) |
| | 30 | 06:45 | PSA execution based on grid scheduling | Inputs item 29 + Results item 29 | P_psa*(07:00) … P_psa*(06:00 +1d) | Iteracio8.mat |
| | 31 | 07:00 | PED simulation to check real behavior | Iteracio8.mat | | Real SOC8.mat |
| 9 | 32 | 07:20 | SOC estimation by the beginning of next hour | Real SOC at 07:00 h & P_psa*(07:00) | Real SOC(08:00) | estimacio.xlsx (iteration_9) |
| | 33 | 07:30 | Grid Operation Scheduler | Real SOC at 08:00 h | P_net*(08:00) … P_net*(07:00 +1d) | ESS_schedule.xlsx (iteration_9) |
| | 34 | 07:45 | PSA execution based on grid scheduling | Inputs item 33 + Results item 33 | P_psa*(08:00) … P_psa*(07:00 +1d) | Iteracio9.mat |
| | 35 | 08:00 | PED simulation to check real behavior | Iteracio9.mat | | Real SOC9.mat |
| 10 | 36 | 08:20 | SOC estimation by the beginning of next hour | Real SOC at 08:00 h & P_psa*(08:00) | Real SOC(09:00) | estimacio.xlsx (iteration_10) |
| | 37 | 08:30 | Grid Operation Scheduler | Real SOC at 09:00 h | P_net*(09:00) … P_net*(08:00 +1d) | ESS_schedule.xlsx (iteration_10) |
| | 38 | 08:45 | PSA execution based on grid scheduling | Inputs item 37 + Results item 37 | P_psa*(09:00) … P_psa*(08:00 +1d) | Iteracio10.mat |
| | 39 | 09:00 | PED simulation to check real behavior | Iteracio10.mat | | Real SOC10.mat |
| 11 | 40 | 09:20 | SOC estimation by the beginning of next hour | Real SOC at 09:00 h & P_psa*(09:00) | Real SOC(10:00) | estimacio.xlsx (iteration_11) |
| | 41 | 09:30 | Grid Operation Scheduler | Real SOC at 10:00 h | P_net*(10:00) … P_net*(09:00 +1d) | ESS_schedule.xlsx (iteration_11) |
| | 42 | 09:45 | PSA execution based on grid scheduling | Inputs item 41 + Results item 41 | P_psa*(10:00) … P_psa*(09:00 +1d) | Iteracio11.mat |
| | 43 | 10:00 | PED simulation to check real behavior | Iteracio11.mat | | Real SOC11.mat |
| 12 | 44 | 10:20 | SOC estimation by the beginning of next hour | Real SOC at 10:00 h & P_psa*(10:00) | Real SOC(11:00) | estimacio.xlsx (iteration_12) |
| | 45 | 10:30 | Grid Operation Scheduler | Real SOC at 11:00 h | P_net*(11:00) … P_net*(10:00 +1d) | ESS_schedule.xlsx (iteration_12) |
| | 46 | 10:45 | PSA execution based on grid scheduling | Inputs item 45 + Results item 45 | P_psa*(11:00) … P_psa*(10:00 +1d) | Iteracio12.mat |
| | 47 | 11:00 | PED simulation to check real behavior | Iteracio12.mat | | Real SOC12.mat |
| 13 | 48 | 11:20 | SOC estimation by the beginning of next hour | Real SOC 11:00 h & P_psa*(11:00) | Real SOC(12:00) | estimacio.xlsx (iteration_13) |
| | 49 | 11:30 | Grid Operation Scheduler | Real SOC at 12:00 h | P_net*(12:00) … P_net*(11:00 +1d) | ESS_schedule.xlsx (iteration_13) |
| | 50 | 11:45 | PSA execution based on grid scheduling | Inputs item 49 + Results item 49 | P_psa*(12:00) … P_psa*(11:00 +1d) | Iteracio13.mat |
| | 51 | 12:00 | PED simulation to check real behavior | Iteracio13.mat | | Real SOC13.mat |
| 14 | 52 | 12:20 | SOC estimation by the beginning of next hour | Real SOC at 12:00 h & P_psa*(12:00) | Real SOC(13:00) | estimacio.xlsx (iteration_14) |
| | 53 | 12:30 | Grid Operation Scheduler | Real SOC at 13:00 h | P_net*(13:00) … P_net*(12:00 +1d) | ESS_schedule.xlsx (iteration_14) |

| Iter. | Item | Time | Process | Inputs | Outputs | Results in files |
|---|---|---|---|---|---|---|
| | 54 | 12:45 | PSA execution based on grid scheduling | Inputs item 53 + Results item 53 | P_psa*(13:00)<br>…<br>P_psa*(12:00 +1d) | Iteracio14.mat |
| | 55 | 13:00 | PED simulation to check real behavior | Iteracio14.mat | | Real SOC14.mat |
| 15 | 56 | 13:20 | SOC estimation by the beginning of next hour | Real SOC 13:00 h & P_psa*(13:00) | Real SOC(14:00) | estimacio.xlsx (iteration_15) |
| | 57 | 13:30 | Grid Operation Scheduler | Real SOC at 14:00 h | P_net*(14:00)<br>…<br>P_net*(13:00 +1d) | ESS_schedule.xlsx (iteration_15) |
| | 58 | 13:45 | PSA execution based on grid scheduling | Inputs item 57 + Results item 57 | P_psa*(14:00)<br>…<br>P_psa*(13:00 +1d) | Iteracio15.mat |
| | 59 | 14:00 | PED simulation to check real behavior | Iteracio15.mat | | Real SOC15.mat |

**Table 9**. Step-by-step description of the 15 iterations for the performance evaluation procedure of the PSA in combination with the optimization algorithm of the power network.

**Figure 31** shows the whole energy schedules determined in this process.

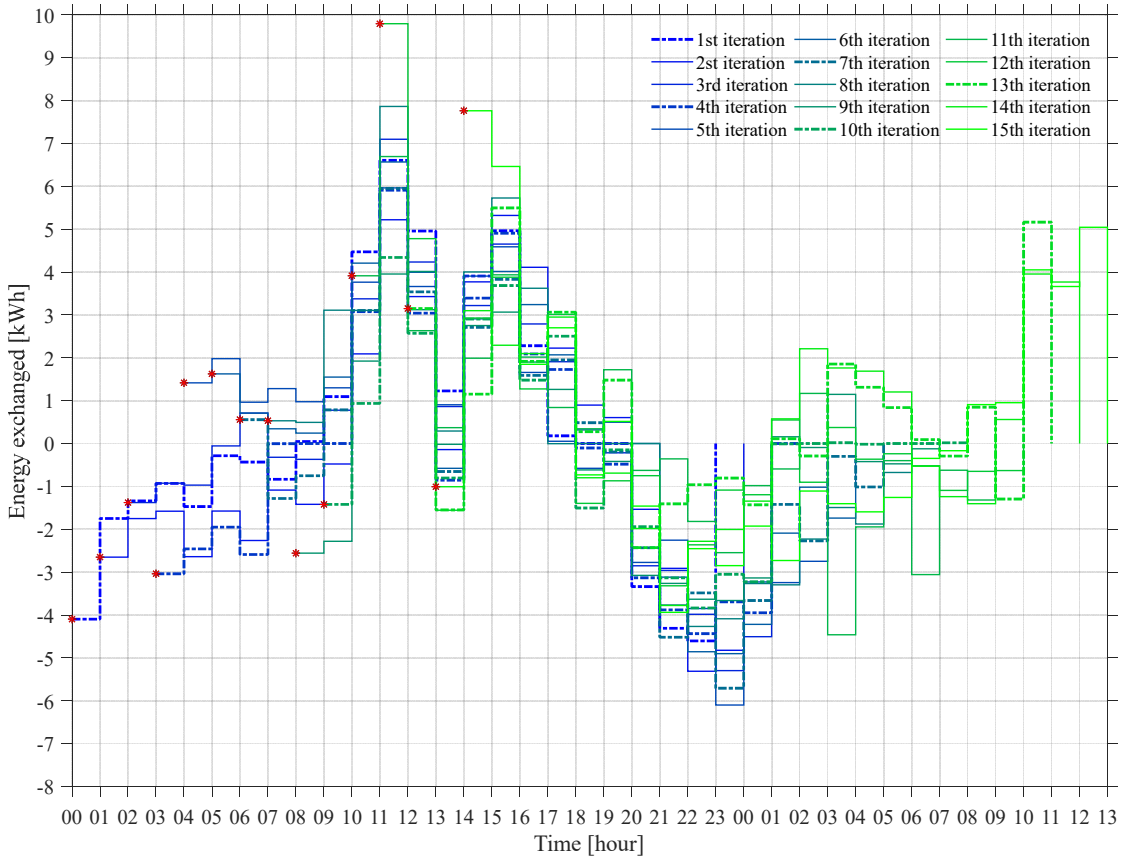


**Figure 31**. Energy schedules determined by the Grid Operation Scheduler. Negative values are for discharging set-points for the battery. Positive ones are for charging.

As a result of the process, we can see here how the scheduling is updated. As **Figure 31** depicts, the trend is to discharge the battery during the night and charging it during the day. As the evolution of day progresses, this tend also evolves, note that first iterations (blue) are more pronounced than final iterations (green). The red points indicate the starting hour per each scheduling. As the service requested by the PED is to apply the peak shaving, batteries are charged at central hours of the day and discharged during the night.

Then, according to the PSA, the PED responds with the exchanging energy between the network and the batteries, fulfilling the requested energy schedule (as **Figure 32** depicts).

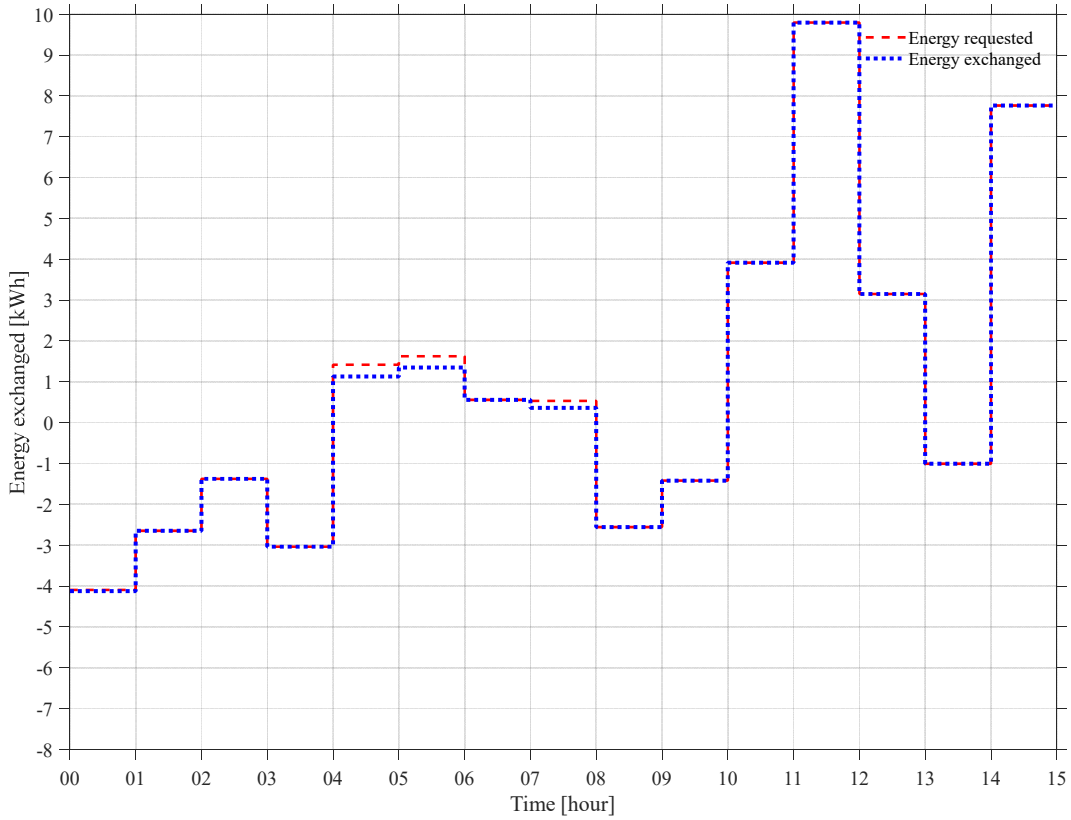


**Figure 32**. Energy requested by the network operator per each hour (red line), and the corresponding output by the PED (blue line).

As observed in **Figure 32**, the error between the requested energy and that actually exchanged by the PED is quite small at all times. At some hours though, the output of the PED presents some variations with respect to the requested energy, and this is because the PSA decides to do so, to compensate the losses in batteries not exactly envisaged by the Grid Operation Scheduler.

Then, **Figure 33** presents the discrepancy between the SOC estimated (considered) by the network operator for its Grid Operation Scheduler per each hour (red line), and actual (averaged) SOC of batteries embedded in the PED (blue line). An averaged SOC, $\overline{soc}_t$, for the set of the 2 battery packs embedded into the PED is calculated as

$$\overline{soc}_t = \frac{\sum E_{r_i} \cdot soc_{i,t}}{\sum E_{r_i}} \qquad \forall_i \in I\,, t \in T \tag{40}$$

where $E_{r_i}$ is the rated energy of each of the battery packs embedded into the PED.

**Figure 34** and **Figure 35** compares the estimated lithium-ion and lead-acid battery SOC's by the PSA, with the real ones provided by the simulation model of the PED. As can be observed, little discrepancies are observed for the lithium-ion battery, while most remarkable ones are for the lead-acid battery. This is because the calculation of SOC for the lead-acid battery is more challenging than for the lithium-ion pack due to the higher internal resistance of this technology. The higher the internal resistance, the higher also the over and under voltages the battery experiences while driving current, and this affects the accuracy of SOC estimation. In addition, it can be observed that the minimum SOC for the lead-acid pack is limited at 0.3 p.u., while it is 0.1 for the lithium-ion pack, as included as a premise for the PSA.

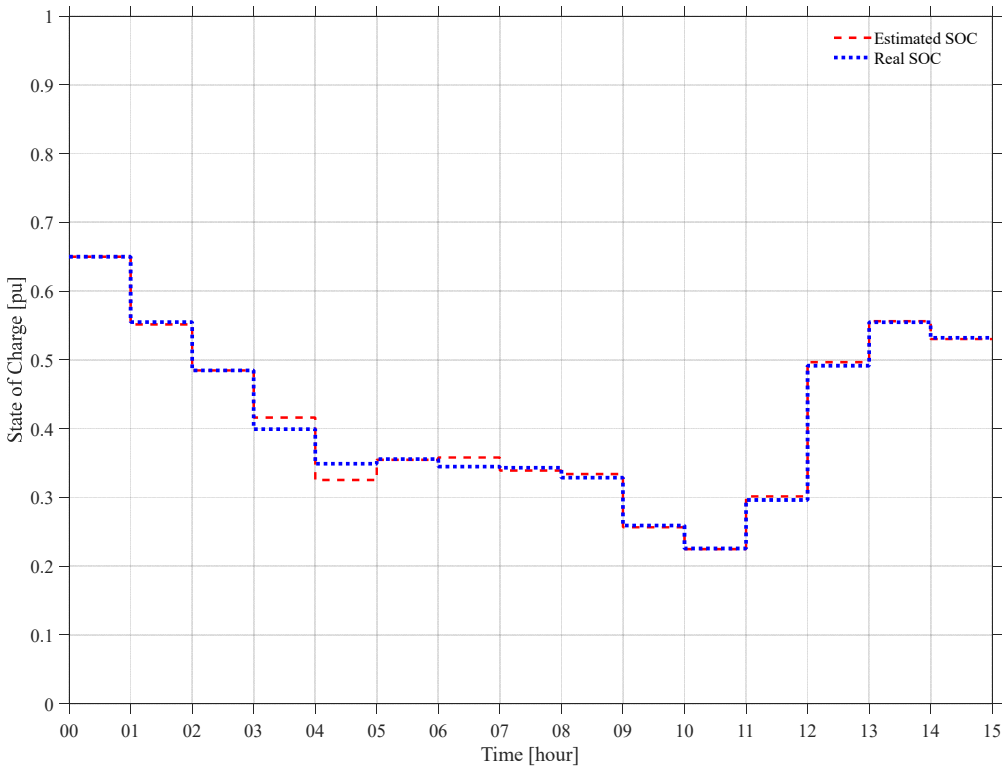


**Figure 33**. SOC estimated (considered) by the network operator for its Grid Operation Scheduler per each hour (red line), and actual (averaged) SOC of batteries embedded in the PED (blue line).

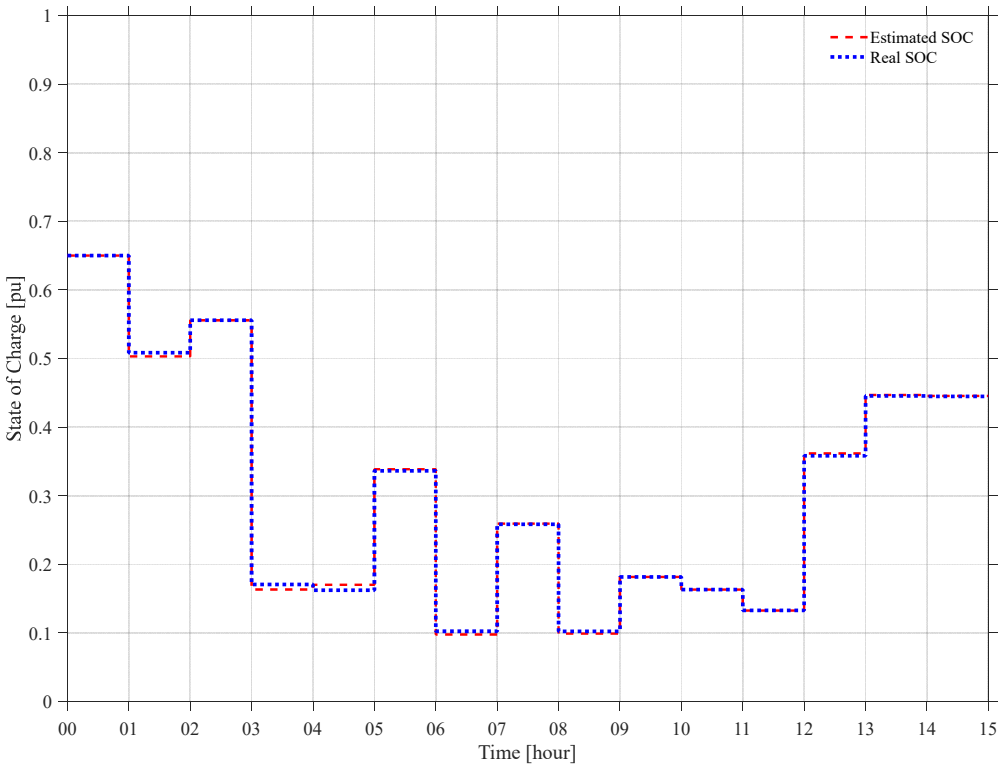


**Figure 34**. Lithium-ion SOC estimated (considered) by the PSA (red line), and actual SOC provided by the simulation model of the PED.

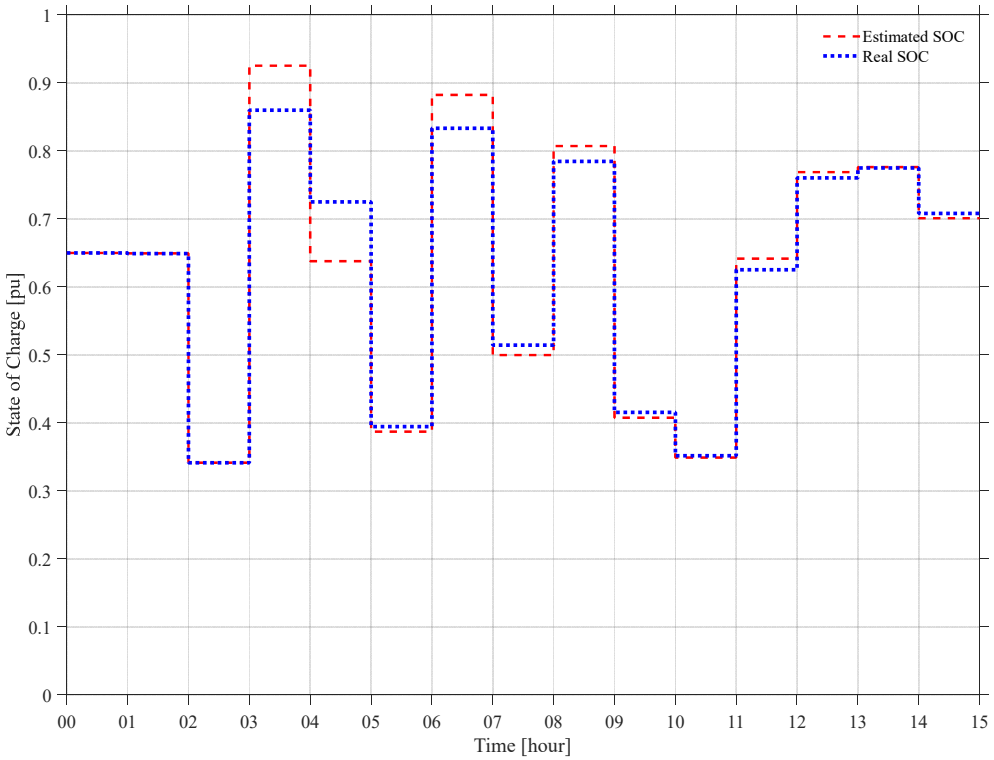


**Figure 35**. Lead-acid SOC estimated (considered) by the PSA (red line), and actual SOC provided by the simulation model of the PED.

Complementing the above graphical evaluations, **Table 10** compares the real SOC (obtained from the simulation model of the PED) with the estimated ones by the PSA and the Grid Operation Scheduler. Per each estimation, the error to the real SOC is also included. It can be clearly appreciated that the error for most of the hours is lower for PSA than for the Grid Operation Scheduler. This is because the PSA details the behavior of each of the batteries embedded into the PED, while the Grid Operation Scheduler considers all batteries as if they were just one aggregated pack. In any case, though, the error for both algorithms (PSA and Grid Operation Scheduler) is below 10% for almost all cases, and this is considered accurate enough.

| Hour | Real SOC (from simulation) | Estimated SOC by PSA and error | | Estimated SOC by the Grid Operation Scheduler and error | |
|---|---|---|---|---|---|
| 01:00 h | 0.5550 | 0.5551 | 0.02 % | 0.5516 | -0.61 % |
| 02:00 h | 0.4847 | 0.4812 | -0.72 % | 0.4873 | 0.54 % |
| 03:00 h | 0.4161 | 0.4161 | 0.00 % | 0.4482 | 7.71 % |
| 04:00 h | 0.3490 | 0.3421 | -1.98 % | 0.3431 | -1.69 % |
| 05:00 h | 0.3556 | 0.3310 | -6.92 % | 0.3542 | -0.39 % |
| 06:00 h | 0.3448 | 0.3570 | 3.54 % | 0.3878 | 12.47 % |
| 07:00 h | 0.3433 | 0.3523 | 2.62 % | 0.3693 | 7.57 % |
| 08:00 h | 0.3286 | 0.3298 | 0.37 % | 0.3499 | 6.48 % |
| 09:00 h | 0.2592 | 0.2619 | 1.04 % | 0.2724 | 5.09 % |
| 10:00 h | 0.2258 | 0.2223 | -1.55 % | 0.2224 | -1.51 % |
| 11:00 h | 0.2963 | 0.3005 | 1.42 % | 0.3048 | 2.87 % |
| 12:00 h | 0.4915 | 0.5018 | 2.10 % | 0.5041 | 2.56 % |
| 13:00 h | 0.5547 | 0.5612 | 1.17 % | 0.5608 | 1.10 % |
| 14:00 h | 0.5321 | 0.5316 | -0.09 % | 0.5319 | -0.04 % |
| 15:00 h | 0.6833 | 0.6885 | 0.76 % | 0.6887 | 0.79 % |

**Table 10**. Objective function results and computation time to find the solution.

# 5. Integration of power sharing algorithm into the ILEM and cybersecurity assessment

## 5.1. Integration of power sharing algorithm into the ILEM

The PSA is a module in the software ILEM (Intelligent Local Energy Management algorithm), which manages the whole PED. This section provides an overview of the main modules of ILEM and the procedure for the execution of the PSA integrated in there. A general description of the modules building up the ILEM is provided by **Figure 36**.

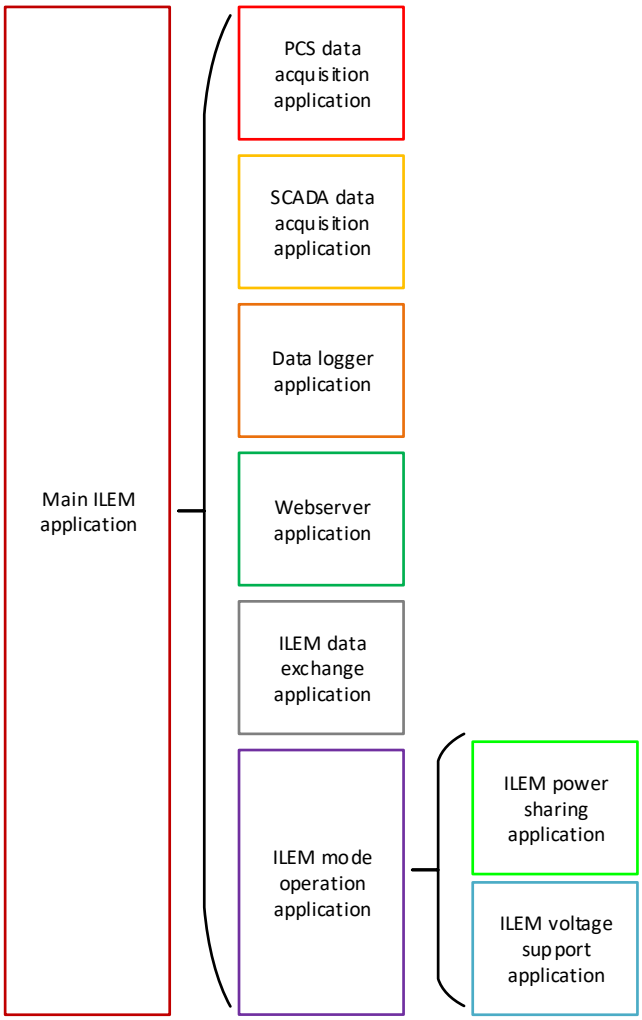


**Figure 36**. Main modules building up the ILEM software.

The ILEM is a software which is continuously running in an industrial PC located into the PED solution. The Main ILEM Application (MIA) encloses all the processes that are performed by the ILEM. The main functionalities of the ILEM are to communicate with the PCS, the SCADA and a web to execute the PSA in order to manage the hybrid storage system and to fulfill the scheduled power exchanging.

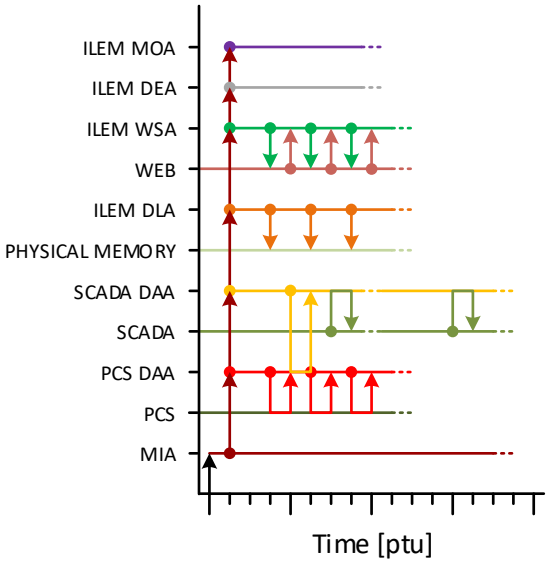


**Figure 37**. Distribution in time of the execution of the main processes carried out by ILEM.

When MIA runs, it calls five independents, parallel and interconnected processes: (i) PCS Data Acquisition Application (DAA), (ii) the SCADA DAA, (iii) the ILEM Data Logger Application (DLA), (iv) the ILEM Webserver Application (WSA), (v) the ILEM Data Exchange Application (DEA) and (vi) the ILEM Mode Operation Application (MOA).

- The **PCS DAA** is an application which communicates periodically (each half-second) with the PCS through MODBUS RTU, it plays the master role, it is continuously asking all the PCS and BMS data and writes punctually the set points.
- The **SCADA DAA** is a permanent MODBUS server that collects all the ILEM data together with the PCS and BMS information. It awaits a valid external client in order to be commanded. In particular, the valid client is the SCADA.
- The **ILEM DLA** is an application which stores the most relevant information from the whole PED in the physical memory. The information is kept up to a maximum of a year.
- The **ILEM WSA** provides a bidirectional communication between the MIA and a web. In addition, this web can be used occasionally for managing manually the PED by a technical user.
- The ILEM DEA is an application which manages the data between the three main sources PCS, SCADA and web.
- Finally, the **ILEM MOA** is the application responsible of operating the PED. **Figure 38** depicts the state machine of ILEM which is performed by the MOA.

When the MOA starts, all set points are reset. The application waits in default mode until an external order. In the default mode, the ILEM does not performs anything apart from communicating with the rest of the players.

The Remote Automatic Mode (RAM) is the most usual operation mode. In this mode the ILEM performs three sub-applications the ILEM Power Sharing Application (PSA) and the ILEM Voltage Support Application (VSA).

The ILEM PSA performs optimizations according to the BMS data and the scheduled power exchanging in order to determinate the best contribution of both storage systems in terms of power accuracy and battery degradation.

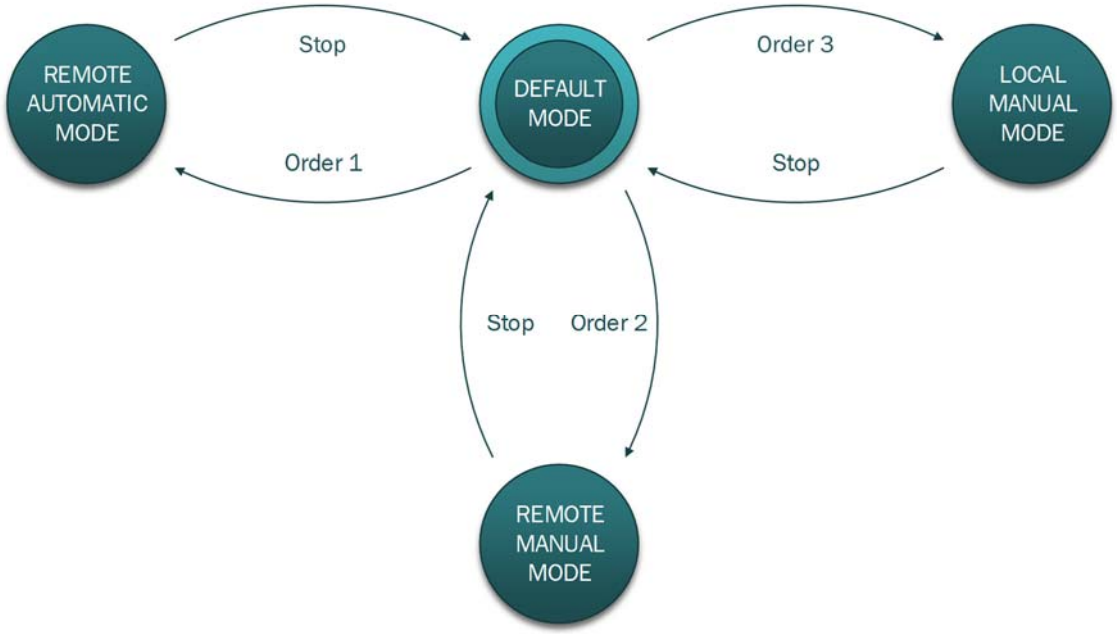


**Figure 38**. State-machine for the ILEM, executed by the Mode Operation Application (MOA).

The **ILEM VSA** is an application which remains in a second phase until an external command. The purpose of it is to calculate the active and reactive powers contribution in order to achieve a desired voltage, according to specific grid constraints. The Manual Remote Mode (RMM) is a specific mode for operating the PED as an external controllable battery. It can also execute the VSA but it cannot execute the PSA. Finally, the Local Manual Mode (LMM) is also a specific mode for debugging and configuring the PED, and also to operate manually the PED.

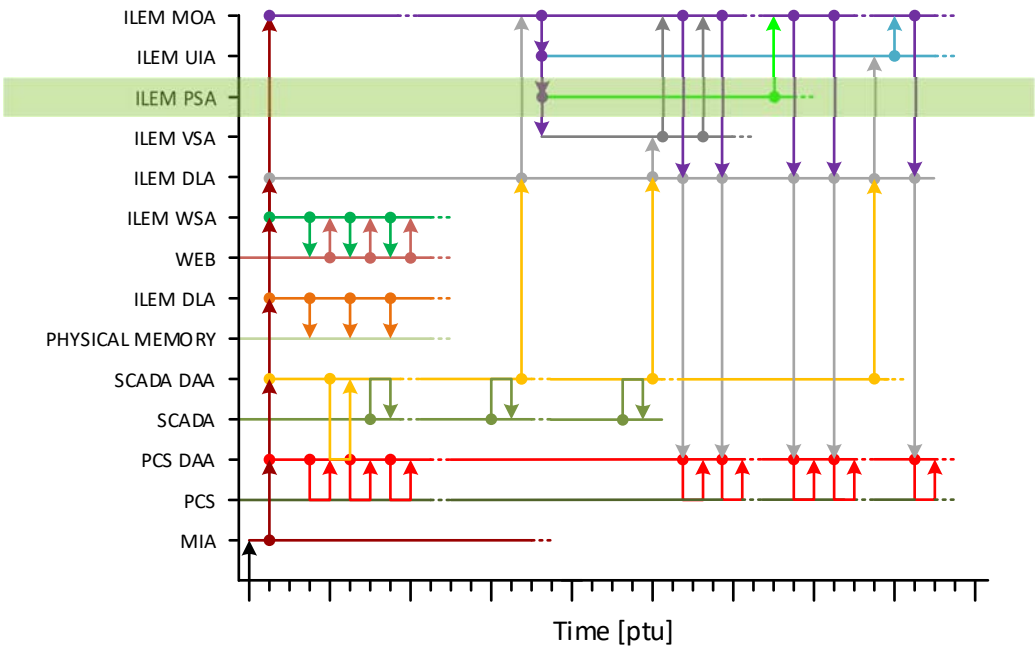


**Figure 39**. Distribution in time of the execution of the main processes carried out by ILEM. Detail of the PSA algorithm (highlighted in green), as triggered by the MOA.

In detail the PSA runs once per hour for determining both lithium-ion and lead-acid batteries operation. The process, in turn, is composed by three different steps:

- **First step**. When a new scheduled power exchanging profile arrives to the PED, the data from the BMS and PCS data are loaded to the PSA. Based on such data, the best solution for each of the three objective function terms of the PSA is determined (see section 3.3). As a reminder:
  - The first optimization criterion for the PSA is to minimize the discrepancy between the power output of the PED and the power scheduling profile. This corresponds to the optimization cost $z_p$. The corresponding optimal solution is $Z_p^*$.
  - The second optimization criterion for the PSA is to minimize the degradation cost for the batteries as function of excessive driving currents. This corresponds to the optimization cost $z_{d1}$. The corresponding optimal solution is $Z_{d1}^*$.
  - The third optimization criterion for the PSA is to minimize the degradation cost for the batteries as function of excessive depth of discharge. This corresponds to the optimization cost $z_{d2}$. The corresponding optimal solution is $Z_{d2}^*$.
- **Second step**. Then, optimal costs $Z_p^*$, $Z_{d1}^*$ and $Z_{d2}^*$ are applied to the optimization function $z$ (see equation (35)).
- **Third step**. The PSA algorithm is executed again, now considering the multi-objective optimization function $z$, as formulated in the previous step.

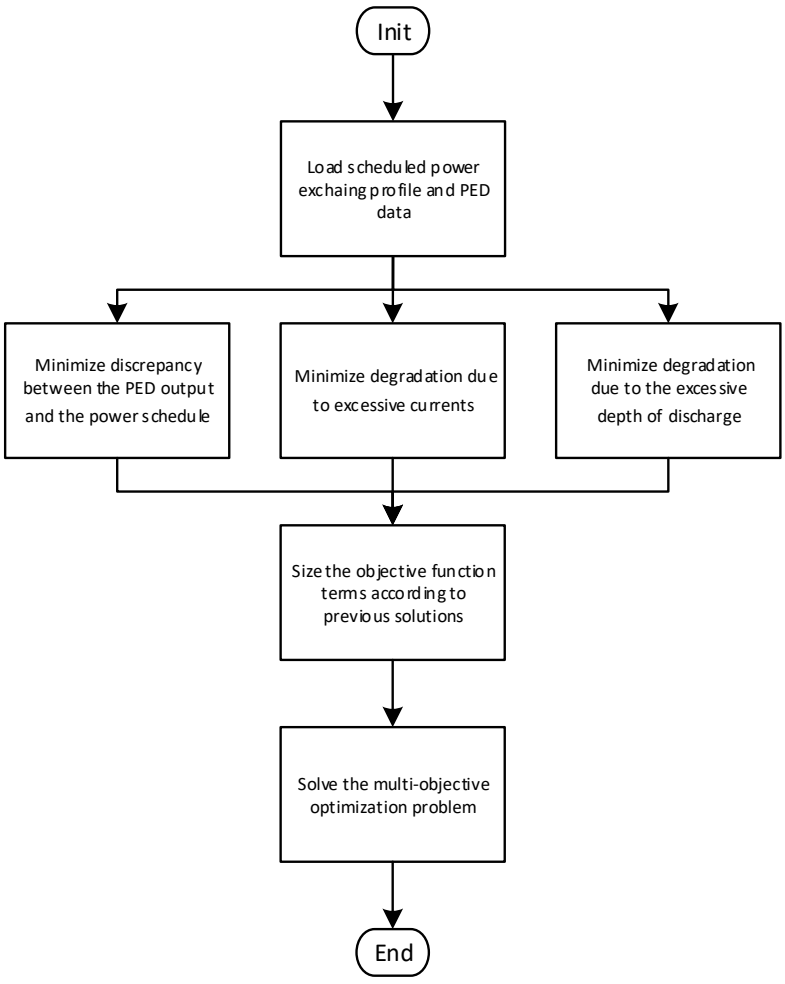


**Figure 40**. Execution procedure for the PSA.

## 5.2. Cybersecurity assessment

### 5.2.1.Summary and scope

The aim of this security check is the identification of typical application and configuration vulnerabilities of the public available services. This section gives an overview about the systems which were investigated, describes the testing approach and lists the recommendations and actions to take.

This external security audit was based on a grey box approach where Joanneum Research investigated the provided IP address on a single host.

### 5.2.2. Result

The host which were audited is secured by a whitelisting approach, which is a good and secure way to prevent public access. Therefore, the auditors were not able to access the host until the administrators whitelisted the IP address which were used for the audit. The security audit identified a total of one low and two medium vulnerabilities. All of them are stated in **Table 11** below and are described in more detail in the respective section. In addition, since the web application is still under development and the functionality could therefore not be tested, an information regarding the input validation can also be found in the table.

| Vulnerability | Solution | Threat level | Reference |
|---|---|---|---|
| SSH User Enumeration | Upgrade SSH daemon | Medium | 5.2.3.6 |
| Unencrypted communications | Applications should use transport-level encryption (SSL/TLS) to protect all communications passing between the client and the server. The Strict-Transport-Security HTTP header should be used to ensure that clients refuse to access the server over an insecure connection. A recommendation of secure TLS version and secure cipher suits can be found in the appendix. | Medium | 5.2.3.6; Annex III |
| Directory Listing | Configure your web server to prevent directory listings for all paths beneath the web root | Low | 5.2.3.6 |

**Table 11**. Result overview

### 5.2.3. Testing approach

#### 5.2.3.1. Method

The tools, methods and techniques used for the security audit can by divided into following categories:

- Usage of general and publicly available analysis tools to detect vulnerabilities of public accessible services.
- Use of experienced specialists to cover security issues which could not be detected automatically.

#### 5.2.3.2. Timetable

The security check was performed at 22.07.2019 with the aim to identify security vulnerabilities.

#### 5.2.3.3. Information about the system to test

The following information (**Table 12**) was provided by the project partner and builds the starting point for the security audit.

| IP address | Description |
|---|---|
| 147.83.xx.xx | PED Front End |

**Table 12**. Information provided

#### 5.2.3.4. Whois

The whois result shows, that the IP range, the registrant as well as basic information like the company name and the company address are revealed. This information, however, is not of any concern.

#### 5.2.3.5. Censys

Censys finds three open services for the given host and also exposes three version numbers. The Censys check shows, that not only the IP address which were used within this audit was whitelisted, but instead the host was exposed to the public as well.

#### 5.2.3.6. 147.83.xx.xx

##### Port scan

The following **Table 13** shows the list of open ports and their corresponding services.

| Port | Service | Additional Output |
|---|---|---|
| 22/tcp | SSH | OpenSSH 7.4p1 Debian 10+deb9u6 (protocol 2.0) |
| 80/tcp | HTTP | Apache/2.4.25 |
| 443/tcp | HTTPS | no response |

**Table 13**. Port scan

##### Services

In this section, the found services are further investigated.

**OpenSSH 7.4p1 (Port 22)**

The ssh daemon exposes the used version, which makes it very easy to look for available vulnerabilities. Thus, if possible, we recommend to alternate the welcome message when a client connects to the service.

*User Enummeration*

**Description**: OpenSSH through 7.7 is prone to a user enumeration vulnerability due to not delaying bailout for an invalid authenticating user until after the packet containing the request has been fully parsed, related to auth2-gss.c, auth2-hostbased.c, and auth2-pubkey.c.

**Solution**: Upgrade the SSH daemon.

**Impact**: 5.0 Medium

**CVE**: CVE-2018-15473

### Webserver (Port 80/443)

The webserver only responds on port 80 with the web control for the RESOLVD system. In general, any web application should use HTTPS to ensure integrity and confidentiality. Thus, HTTP on port 80 should be disabled and any content should be moved to use HTTPS.

*Unencrypted communications*

**Description:** The application allows users to connect to it over unencrypted connections. An attacker suitably positioned to view a legitimate user's network traffic could record and monitor their interactions with the application and obtain any information the user supplies. Furthermore, an attacker able to modify traffic could use the application as a platform for attacks against its users and third-party websites. Unencrypted connections have been exploited by ISPs and governments to track users, and to inject adverts and malicious JavaScript. Due to these concerns, web browser vendors are planning to visually flag unencrypted connections as hazardous. To exploit this vulnerability, an attacker must be suitably positioned to eavesdrop on the victim's network traffic. This scenario typically occurs when a client communicates with the server over an insecure connection such as public Wi-Fi, or a corporate or home network that is shared with a compromised computer. Common defenses such as switched networks are not sufficient to prevent this. An attacker situated in the user's ISP or the application's hosting infrastructure could also perform this attack. Note that an advanced adversary could potentially target any connection made over the Internet's core infrastructure. Please note that using a mixture of encrypted and unencrypted communications is an ineffective defense against active attackers, because they can easily remove references to encrypted resources when these references are transmitted over an unencrypted connection.

**Threat Level**: Medium

**Solution:** Applications should use transport-level encryption (SSL/TLS) to protect all communications passing between the client and the server. The Strict-Transport-Security HTTP header should be used to ensure that clients refuse to access the server over an insecure connection. Also, when using TLS, it is essential to also use secure cipher suits. A recommendation can be found in the Annex III.

**CWE:** 326

*Directory listing*

**Description:** Web servers can be configured to automatically list the contents of directories that do not have an index page present. This can aid an attacker by enabling them to quickly identify the resources at a given path, and proceed directly to analyzing and attacking those resources. It particularly increases the exposure of sensitive files within the directory that are not intended to be accessible to users, such as temporary files and crash dumps. Directory listings themselves do not necessarily constitute a security vulnerability. Any sensitive resources within the web root should in any case be properly access-controlled, and should not be accessible by an unauthorized party who happens to know or guess the URL. Even when directory listings are disabled, an attacker may guess the location of sensitive files using automated tools.

**Threat Level**: Low

**Solution:** There is not usually any good reason to provide directory listings, and disabling them may place additional hurdles in the path of an attacker. This can normally be achieved in two ways:

Configure your web server to prevent directory listings for all paths beneath the web root;

Place into each directory a default file (such as index.htm) that the web server will display instead of returning a directory listing.

**CWE:** 538, 548

### PED Front-End

The PED web application is still under development and therefore could only be partly audited. The audited part of the application consists of single HTML, a single Javascript file as controller (resolvd_controller.js), and some images and css files. Since any code that would connect to the backend, which is not implemented yet, is not in use, no functionality can be audited. However, the Javascript controller consists of some client side input validation, which should be validated on the server side (backend). This is due to the fact that client side validation can be easily circumvented using interception proxies.

# 6. Conclusions

This report summarizes the work done in regard of the development of the so-called Power Sharing Algorithm (PSA). The PSA is one of the algorithms composing the local controller of the Power Electronics Device (PED). The PED development is the main goal of Work Package 2 of the RESOLVD project. The main objective of this deliverable was to the report the design the PSA, evaluate its performance and assess its integration as one of the modules of the Intelligent Local Energy Manager (ILEM) software (also addressing the cybersecurity aspect), which is the software in charge of connecting the Power Electronics Device (PED) with the rest of the power network.

The PSA has been defined as a multi-objective criteria optimization algorithm. It receives a time-dependent power profile set-point from the network operator, and distributes it among the different battery types embedded into the PED. This way, it triggers an internal power sharing, based on the criteria of maximum performance and minimum battery degradation. From a literature review, two degradation mechanisms for batteries were identified as most important for the purposes of the present project: the power developed by batteries, and the depth of discharge. Based on that, the PSA incorporated constraints to penalize degradation.

To design the PSA, batteries were firstly characterized. While the parameters for the lead-acid battery were directly obtained from the manufacturer, the parameters for the lithium-ion pack were derived from laboratory tests. Results were translated into a simulation model, that reliably represent the dynamic behavior of the batteries while charging and discharging. This simulation model of batteries, along with the simulation model of the associated power electronics, completed a simulation platform for the whole PED.

As a multi-objective criteria optimization algorithm, each time the PSA is executed it is in fact solved four times. Tests performed and reported in this deliverable indicated that considering time-dependent power profile series of 24 set-points, the time needed for carrying out such four executions for the PSA is just few seconds at most. Thus, formulating this as a multi-objective criteria problem, it becomes feasible to be applied on field for the purposes of the project.

Then, to test the PSA, two different exercises were carried out. The first one aims to test the PSA while driven by an arbitrary, academic time-dependent power profile set-point. The results of this exercise show that the PSA reliably fit the response of the PED to the requirements of the network operator while still minimizing degradation of the batteries (e.g. higher power rates were experienced by the lithium-ion pack and not by the lead-acid pack, and minimum SOCs for batteries were respected all times. The second exercise tested the PSA while driven by a realistic time-dependent power profile set-point provided by the Grid Operation Scheduler.

For this second exercise, an iterative procedure was needed. Fifteen iterations were carried out (emulating the behavior of the algorithms during the first fifteen hours of a day). Results of such iterative process show how the PSA manages the charging and discharging of the batteries following the power set-points from Grid Operation Scheduler. Little discrepancy between the requested power and the developed by the PED is noticed. In fact, the output of the PED mostly fits with the requested value for most of the evaluated time periods, and for those presenting discrepancies, the error with respect to power demand is lower than 10%. Both algorithms, PSA and Grid Operation Scheduler, presented also a good performance while estimating battery SOC. In particular, the error for both algorithms in SOC estimation was below 10% for almost all evaluated cases.

After PSA design and test, this was presented as a part of the ILEM and cybersecurity aspect was assessed, motivated by the fact that the ILEM is actually exchanging information with other agents of the network. The cybersecurity check was based on a grey box approach where the provided IP address was investigated on a single host. The conclusions for this exercise are that the host is secured by a whitelisting approach, which is a good and secure way to prevent public access. The security audit identified a total of one low and two medium vulnerabilities. These vulnerabilities were in regard of SSH user enumeration; unencrypted communications; and weak directory listing.

## References


[1]. Díaz-González F, Sumper A, Gomis-Bellmunt O. (2016) Energy storage in power systems, John Wiley and Sons, pp. 306

[2]. Plett G. (2004) Extended Kalman filtering for battery management systems of LiPB-based HEV battery packs. Part 2. Modeling and identification. Journal of Power Sources 134:262-276

[3]. Shepherd CM. (1962) Theoretical design of primary and secondary cells. Part III – Battery discharge equation, US Naval Research Laboratory, Washington, DC

[4]. He H, Xiong R, Guo H, Li S. (2012) Comparison study on the battery models used for the energy management of batteries in electric vehicles. Energy Conversion and Management 64:113-121

[5]. Van de Geer, SA. (2005) Least Squares Estimation. Encyclopedia of Statistics in Behavioral Science, 2:1041-1045

[6]. Test data for lithium-ion cell INR 18650-20R. Calce Battery Research Group. URL: https://web.calce.umd.edu/batteries/data.htm. Accessed: 10.03.2019

[7]. Krause PC, Wasynczuk O, Sudhoff SD. (2002) Analysis of Electric Machinery and Drive Systems, John Wiley and Sons, Inc., Hoboken, NJ

[8]. Díaz-González F, Heredero-Peris D, Galceran-Arellano S. (2018) Design methodology for a dc-dc power conversion system with EIS capability for battery packs. Simulation Modelling Practice and Theory, 87:15-34

[9]. Zhou X, Huang J, Pan Z, Ouyang M. (2019) Impedance characterization of lithium-ion batteries aging under high-temperature cycling: importance of electrolyte-phase diffusion. Journal of Power Sources 426:216-222

[10]. Madani Layadi T, Champenois G, Mostefai M, Abbes D. (2015) Lifetime estimation tool of lead-acid batteries for hybrid power sources design. Simulation Modelling Practice and Theory 54:36-48

[11]. Datasheet for Power-Sonic GEL batteries, PS Series. URL: https://www.power-sonic.com/batteries/ps-series/. Accessed: 15.07.2019

[12]. Datasheet for RENESOLA GEL batteries, model 6GFMJ-65. URL: http://www.renesola.com/file/Global/product/pdf/Lead-Acid%20Battery.pdf. Accessed: 15.07.2019

[13]. Datasheet for Ultracell VRLA battery, model UCG75-12. URL: http://ultracell.co.uk/datasheets/UCG75-12.pdf. Accessed: 15.07.2019

[14]. Pelletier S, Jabali O, Laporte G, Veneroni M. (2017) Battery degradation and behavior for electric vehicles: review and numerical analyses of several models. Transportation Research Part B 130:158-187

[15]. Vignarooban K, Chu X, Chimatapu K, et al. (2016) State of health determination of sealed lead acid batteries under various operating conditions. Sustainable Energy Technologies and Assessments 18:134-139

[16]. Power-Sonic Corporation website, "PDC-121000 battery datasheet". URL: https://www.power-sonic.com/product/pdc-121000/. Accessed: 02.03.2019

[17]. Panasonic website, "Lithium-ion batteries datasheet". URL: https://na.industrial.panasonic.com/products/batteries/rechargeable-batteries/lithium-ion. Accessed: 02.03.2019

[18]. Kokam website, "Lithium-ion batteries". URL: http://kokam.com/cell/. Accessed: 02.03.2019

[19]. Omar N, Monem MA, Firouz Y, et al. (2014) Lithium iron phosphate based battery – Assessment of the aging parameters and development of cycle life model. Applied Energy 113:1575-1585

# Annex I: Simulation model in Matlab Simulink of the Power Electronics Device (PED) including batteries

This annex describes the simulation platform built in Matlab Simulink utilized for the purposes of the work in the task 2.3. This model complements the one built in deliverable 2.1 of RESOLVD project (corresponding to the task 2.1). The differences among the models are that the one presented here is averaged and includes the battery model. It is averaged because of the fact that power converters are modeled as controllable ideal voltage sources. Since averaged, the model can be utilized to simulate the behavior (i.e. current and voltage dynamics, power flow among components, electrical stability of associated controllers) of the system for long periods of time, e.g. charge or discharge processes for batteries for hours. As a reminder, in the non-averaged model in 2.1, the power converters were treated as actual H-bridges from which switching and conduction losses of semiconductors could be estimated, the behavior of the system against eventualities like short circuits as well. A non-averaged model can, however, be utilized to simulate short periods of time, e.g. some seconds, because of the high computational effort involved. This is the main drawback of a non-averaged model and for this reason it is not suitable for this task 2.3.

**Figure 41** firstly presents the main blocks of the simulation model. As shown, the model is composed by 4 main Blocks (blocks A, B, C and D). Block E just collects all plotting scopes. The front-end inverter of the PED is represented by Block A. Block B contents the dc-link interfacing the dc side of the front-end inverter with the dc-dc converters in Blocks C and D. These Blocks C and D, in addition, includes the model of the two batteries included in the system.

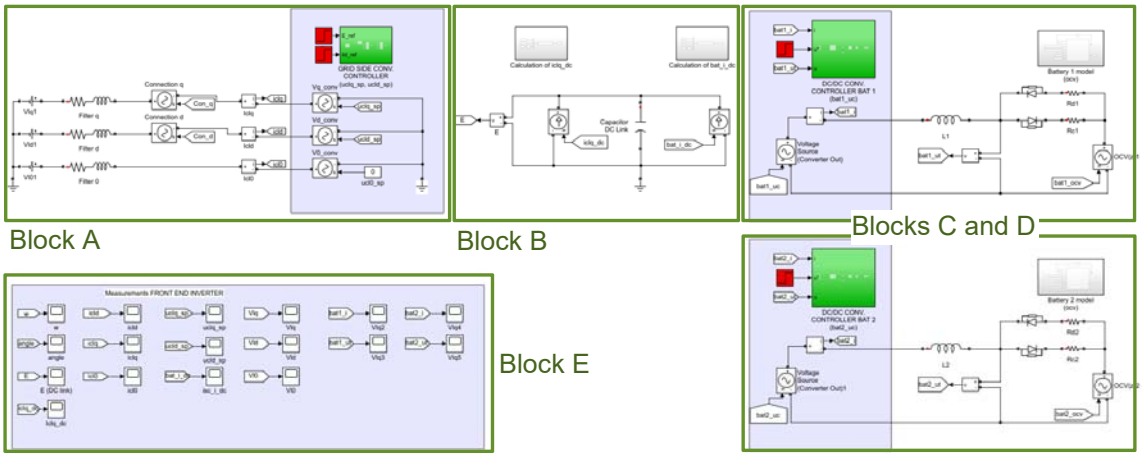


**Figure 41**. General description of Matlab Simulink model for the Power Electronics Device (PED) including two batteries. Block A: Front-end inverter; Block B: dc-link; Block C: dc-dc converter and battery 1; Block D: dc-dc converter and battery 2; Block E: Plotting scopes.

Block A is again presented in **Figure 42**. As shown, the front end inverter and the external grid are modelled adopting the Park's *qd0* frame [7]. The advantage of doing so, is that voltage and current waveforms are not sinusoidal, but constant in time. This reduces computational effort for the model. The voltage across each of axis of the Park's frame with respect to ground in the model by three voltage sources. Such voltage sources are connected to a resistance and inductance in series, characterizing the short-circuit impedance of the grid. Then, the grid is connected to three controllable voltage sources again, which actually model the front-end inverter.

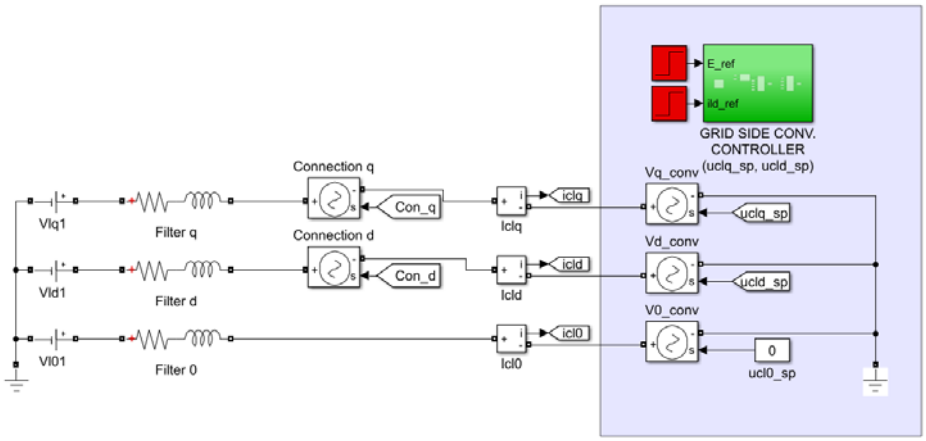


**Figure 42**. Detail of Block A: front end inverter and external ac network.

The *qd0* voltages synthetized at the converter terminals are managed by the block in green "Grid Side Converter Controller." A detail of such controller is depicted in **Figure 43**. As can be noted, there are two control loops, each providing the voltages to be synthetized by the converter at its terminals through the *q* and *d* axis. For the q axis, there are two control loops in cascade. The outer control loop is in charge of managing the dc-link voltage $E$. The output of such control loop provides the current setpoint $i_{clq}^{*}$ for the inner control loop. The controller for the Grid Side Converter is widely described in [1].

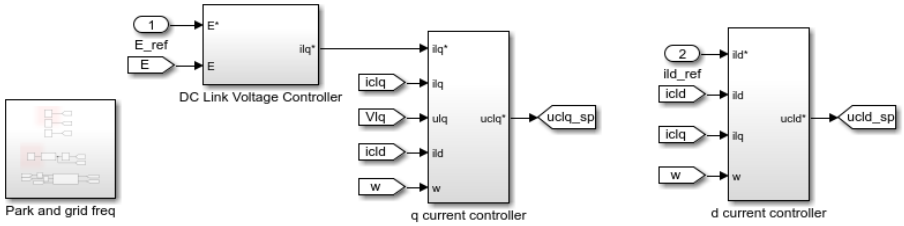


**Figure 43**. Detail of Grid Side Converter Controller.

For completeness though, the contents in the blocks "d current controller" and "q current controller" are presented in **Figure 44** and **Figure 45**. Contents in the block "DC link voltage controller" are presented in **Figure 46**.

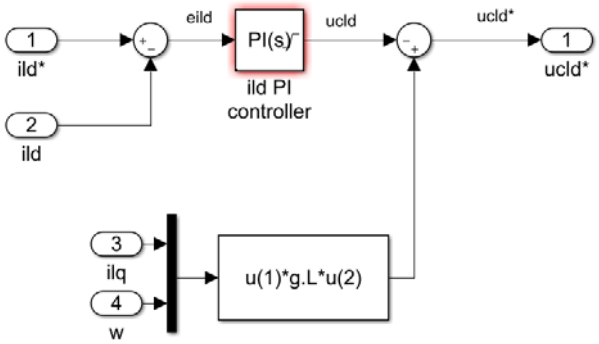


**Figure 44**. Detail of "d current controller".

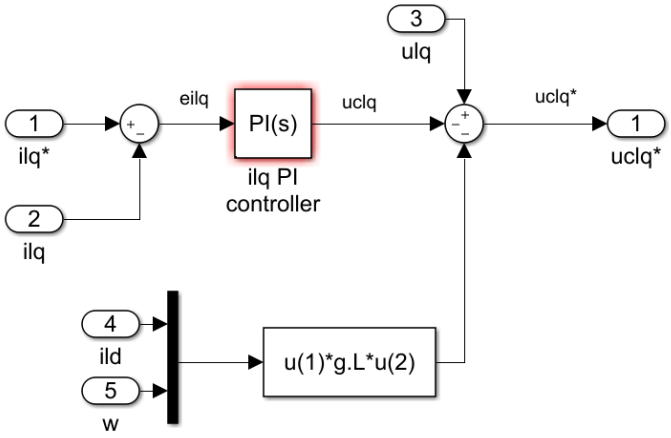


**Figure 45**. Detail of "q current controller".

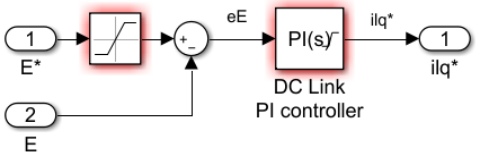


**Figure 46**. Detail of "DC link voltage controller".

Block B models the interface between the dc side of the front end inverter and the dc-dc converters in blocks C and D integrating two battery packs. A detail of Block B is presented in **Figure 47**.

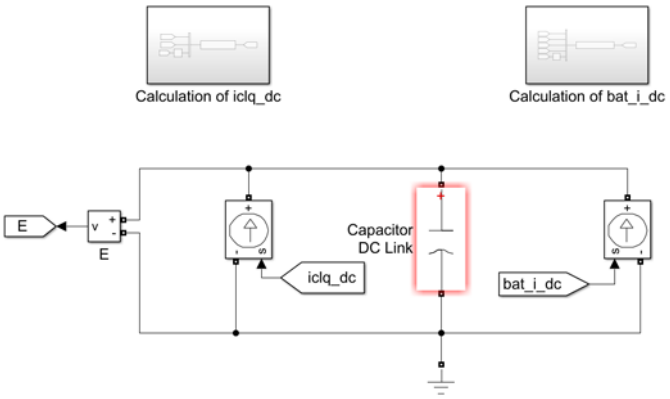


**Figure 47**. Detail of Block B: dc-link.

As can be noted, the dc-link model is composed by a current source $i_{clq\_dc}$, weighting the dc current at the dc-side of the front end inverter; a capacitor; and a current source $bat\_i\_dc$, weighting the dc current injected or subtracted from the dc-link by the batteries. Thus, a constant dc-link voltage $E$ is given by the equilibrium among the current $i_{clq\_dc}$ and $bat\_i\_dc$. Any mismatch among these two magnitudes is to be translated into a current injected or provided by the dc-link capacitor, thus varying its energy stored and, as a consequence, the voltage $E$.

The equations calculating the current $i_{clq\_dc}$ are in the block "Calculation of iclq_dc" in **Figure 47**. A detail of such block is presented in **Figure 48**.

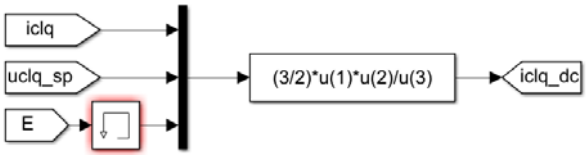


**Figure 48**. Detail of Block "Calculation of iclq_dc".

Analogously, the equations calculating the current $bat\_i\_dc$ are presented in the block "Calculation of bat_i_dc" in **Figure 47**. A detail of such block is presented in **Figure 49**.

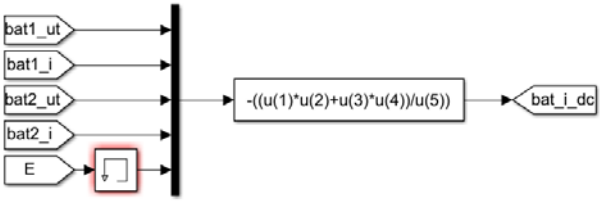


**Figure 49**. Detail of Block "Calculation of bat_i_dc".

Blocks C and D are almost identical. They just differ in the input data they received, characterizing the two battery packs. A detail of Block C is firstly introduced in **Figure 50**.

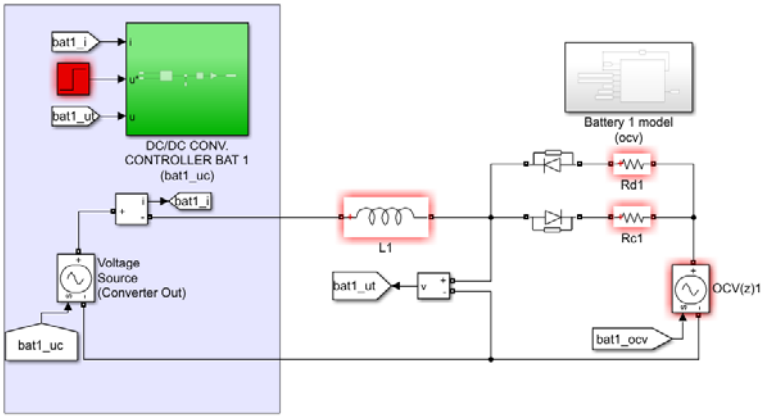


**Figure 50**. Detail of Block C, dc-dc converter and battery 1.

This Block C includes the modeling of a dc-dc converter (shadowed in light blue in **Figure 50**), along with an inductive filter (filter $L1$) and the battery 1. As noted, the battery is modeled as a resistance in series with a voltage source. As introduced in section 2.2, the internal resistance of the cell slightly varies for charging or discharging circumstances, and this is why in the model this is represented, in fact, as a two different resistances in parallel. The voltage source weights the voltage at the terminals of the battery in the case it is in open circuit. The value of such voltage (i.e. the open circuit voltage, $OCV(z)$) depends on the state of charge ($z$) of the battery. So mathematical expressions should be included in the model to estimate the state of charge and derive the voltage $OCV(z)$. These are included in the block "Battery 1 model" in **Figure 51**. A detail of what is inside such block is presented in **Figure 52**.

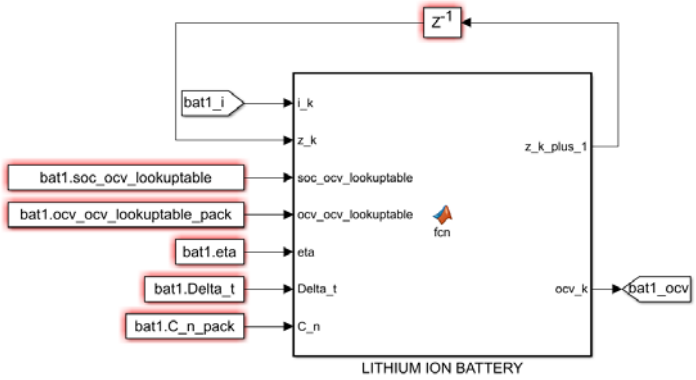


**Figure 51**. Detail of Block "Battery 1 model".

Equations for state of charge and open circuit voltage estimation are in the box "LITHIUM ION BATTERY" (see the code in **Figure 52**). All input data for such box should be derived from manufacturer datasheets or experimental tests.

```
function [z_k_plus_1,ocv_k] = fcn(i_k,z_k,soc_ocv_lookuptable,
ocv_ocv_lookuptable,eta,Delta_t,C_n)

ocv_k = interp1(soc_ocv_lookuptable,ocv_ocv_lookuptable,z_k,
'linear','extrap');
z_k_plus_1 = z_k + ( eta * Delta_t / C_n ) * i_k;
```

**Figure 52**. Detail of box "LITHIUM ION BATTERY".

Then, the dc-dc converter integrating each of the batteries, as represented in Figure XX, is modeled as a controllable voltage source which synthetizes a voltage $bat1\_uc$. Depending on the magnitude of this voltage with respect to the voltage of the battery $bat1\_ut$, the battery is being charged or discharged. Thus, the control of such voltage $bat1\_uc$ is, in fact, the duty for the associated controller in the green block in **Figure 50** "DC-DC CONV. CONTROLLER BAT 1". A detail of such controller is offered in **Figure 53**.

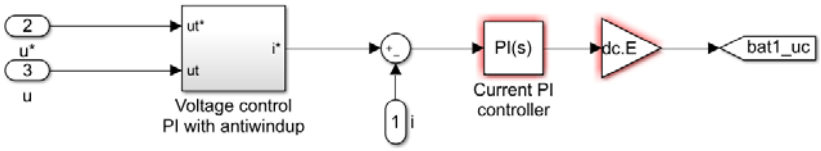


**Figure 53**. Detail of box "DC-DC CONV. CONTROLLER BAT 1".

As depicted in **Figure 53**, the voltage control is equipped with an antiwindup. A graphical description on how such anti-windup is implemented, is offered in **Figure 54** and **Figure 55**.

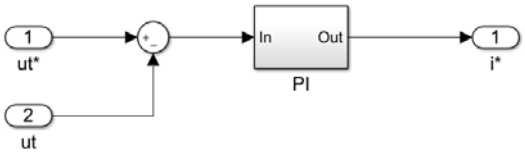


**Figure 54**. Detail of box "Voltage control PI with anti-windup".

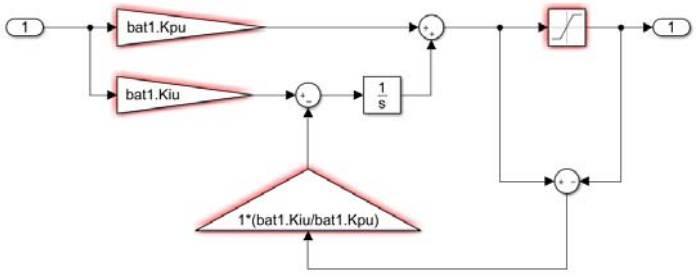


**Figure 55**. Detail of box "PI" in the "Voltage control PI with anti-windup".

Prior executing the simulation model, the input parameters should be defined. For that, Matlab script has been built. For completeness, this is included in the following.

```
%% ------------------------------------------------------------------ %
Hybrid energy storage system integrating two battery packs through two
dc-dc converters in parallel and connected to the dc-link of a front
end inverter.

Date and version: 30.04.2019, v1.0
% ------------------------------------------------------------------ %

%% INITIALIZATION
    clear all;
    clc;

%% GRID PARAMETERS

    g.Ul=400;           % (V) - Line RMS voltage (Phase-to-Phase)
    g.Uf=g.Ul/sqrt(3);  % (V) - Phase RMS voltage
    g.Ufp=g.Uf*sqrt(2); % (V) - Phase peak voltage
    g.F=50;             % (Hz)- Frequency
    g.R=0.3;            % (Ohms) - Line resistance
    g.L=0.005;          % (H)    - Line impedance
    g.lambda=g.L/g.R;   % (-)    - Time constant

%% FRONT-END INVERTER PARAMETERS

    dc.E=800;               % (V) - Rated dc-link voltage
    dc.C=0.01;              % (F) - dc-link capacitance
    inv.P=40000;            % (W) - Inverter power
    inv.current=inv.P/dc.E; % (A) - Maximum current for the inverter

%% FRONT-END INVERTER CONTROLLERS

% DC-LINK CONTROLLER

    % TO BE SELECTED BY THE DESIGNER
    dc.w=5;  % (rad/s) - Natural frequency
    dc.xi=1; % (-)     - Damping coefficient

    % CALCULATIONS
    dc.k=g.Ufp/dc.E;                    % (-)
    dc.Kp=4*dc.C*dc.xi*dc.w/(3*dc.k); % (-) - Proportional gain
```

```
    dc.Ki=2*dc.C*(dc.w)^2/(3*dc.k);   % (-) - Integral gain
    dc.maxsat= dc.E*1.2;              % (V) - Maximum voltage
    dc.minsat=g.Ul/(2*dc.E/sqrt(3));  % (V) - Minimum voltage
    g.Uf_security=0.1;                % (p.u.) – Adm. voltage var.
    dc.ilq=inv.P*2/(g.Ufp*(1-g.Uf_security)*3); % (A) – Max. current.

% Q-CURRENT CONTROLLER

    % TO BE SELECTED BY THE DESIGNER
    q.w=100; % (rad/s) - Natural frequency
    q.xi=1;  % (-)     - Damping coefficient

    % CALCULATIONS
    q.Kp=g.L/g.lambda; % (-) - Proportional control gain
    q.Ki=g.R/g.lambda; % (-) - Integral control gain

% D-CURRENT CONTROLLER

    % TO BE SELECTED BY THE DESIGNER
    d.w=100; % (rad/s) - Natural frequency
    d.xi=1;  % (-)     - Damping coefficient

    % CALCULATIONS
    d.Kp=g.L/g.lambda; % (-) - Proportional control gain
    d.Ki=g.R/g.lambda; % (-) - Integral control gain

%% BATTERY 1: LITHIUM-ION

    % CELL PARAMETERS
    bat1.Rd_cell = 0.2648;  % (Ohm) - Discharge resistance
    bat1.Rc_cell = 0.2430;  % (Ohm) - Charge resistance
    bat1.eta = 1;           % (-)   - Couloumbic efficiency
    bat1.Delta_t = 0.01;    % (s)   - Time step
    bat1.C_n_cell = 7200;        % (As)  - Cell capacity
    bat1.soc_ocv_lookuptable = [0.0066 0.1004 0.2004 0.3003 0.4002
0.5002 0.6001 0.7000 0.8000 0.8999 0.9998]';
    bat1.ocv_ocv_lookuptable_cell = [3.2472 3.4658 3.5546 3.5987
3.6254 3.6645 3.7531 3.8397 3.9400 4.0502 4.1763]';

    % PACK PARAMETERS
    bat1.Nseries = 333;
    bat1.Nparallel = 200;
    bat1.Rd_pack = bat1.Rd_cell*bat1.Nseries/bat1.Nparallel;
    bat1.Rc_pack = bat1.Rc_cell*bat1.Nseries/bat1.Nparallel;
    bat1.C_n_pack = bat1.C_n_cell*bat1.Nparallel;
    bat1.ocv_ocv_lookuptable_pack = bat1.Nseries*[3.2472 3.4658 3.5546
3.5987 3.6254 3.6645 3.7531 3.8397 3.9400 4.0502 4.1763]';
    bat1.Unom_pack = mean(bat1.ocv_ocv_lookuptable_pack);
    bat1.Uexp_pack = max(bat1.ocv_ocv_lookuptable_pack);
    bat1.Umin_pack = min(bat1.ocv_ocv_lookuptable_pack);

%% DC-DC CONVERTER PARAMETERS FOR BATTERY 1: LITHIUM-ION

    bat1.L = 0.005; % (H) - Inductance between converter and battery
    bat1.P = 20e3;  % (W) - Rated power
    bat1.Irated = bat1.P / bat1.Umin_pack;  % (A) - Rated current
```

```
%% DC-DC CONVERTER CONTROLLERS FOR BATTERY 1: LITHIUM-ION

% VOLTAGE CONTROLLER

    % TO BE SELECTED BY THE DESIGNER
    bat1.wu=1;    % (rad/s) - Natural frequency
    bat1.xiu=0.7; % (-)     - Damping coefficient

    % CALCULATIONS
    bat1.C=(bat1.C_n_pack*(bat1.Uexp_pack +
bat1.Unom_pack))/((bat1.Uexp_pack^2)-(bat1.Unom_pack^2)); % (F)
    bat1.Kpu=2*bat1.xiu*bat1.wu*bat1.C;  % (-) - Proportional gain
    bat1.Kiu=bat1.wu^2*bat1.C;           % (-) - Integral gain

% CURRENT CONTROLLER

    % TO BE SELECTED BY THE DESIGNER
    bat1.wi=20;   % (rad/s) - Natural frequency
    bat1.xii=0.7; % (-)     - Damping coefficient

    % CALCULATIONS
    bat1.Kpi=2*bat1.xii*bat1.wi*bat1.L/dc.E; % (-) - Proportional gain
    bat1.Kii=bat1.wi^2*bat1.L/dc.E;          % (-) - Integral gain

%% BATTERY 2: LEAD-ACID

    % CELL PARAMETERS
    bat2.Rd_cell = 0.2648;  % (Ohm) - Discharge resistance
    bat2.Rc_cell = 0.2430;  % (Ohm) - Charge resistance
    bat2.eta = 1;           % (-)   - Couloumbic efficiency
    bat2.Delta_t = 0.01;    % (s)   - Time step
    bat2.C_n_cell = 75*3600;        % (As)  - Cell capacity
    bat2.soc_ocv_lookuptable = [0.0066 0.1004 0.2004 0.3003 0.4002
0.5002 0.6001 0.7000 0.8000 0.8999 0.9998]';
    bat2.ocv_ocv_lookuptable_cell = [10.8 10.9 11.1 11.5 12 12.05 12.1
12.2 12.7 13.1 13.5]';

    % PACK PARAMETERS
    bat2.Nseries = 24;
    bat2.Nparallel = 1;
    bat2.Rd_pack = bat2.Rd_cell*bat2.Nseries/bat2.Nparallel;
    bat2.Rc_pack = bat2.Rc_cell*bat2.Nseries/bat2.Nparallel;
    bat2.C_n_pack = bat2.C_n_cell*bat2.Nparallel;
    bat2.ocv_ocv_lookuptable_pack = bat2.Nseries*[3.2472 3.4658 3.5546
3.5987 3.6254 3.6645 3.7531 3.8397 3.9400 4.0502 4.1763]';
    bat2.Unom_pack = mean(bat2.ocv_ocv_lookuptable_pack);
    bat2.Uexp_pack = max(bat2.ocv_ocv_lookuptable_pack);
    bat2.Umin_pack = min(bat2.ocv_ocv_lookuptable_pack);

%% DC-DC CONVERTER PARAMETERS FOR BATTERY 2: LEAD-ACID

    bat2.L = 0.005; % (H) - Inductance between converter and battery
    bat2.P = 20e3;  % (W) - Rated power
    bat2.Irated = bat2.P / bat2.Umin_pack;  % (A) - Rated current
```

```
%% DC-DC CONVERTER CONTROLLERS FOR BATTERY 2: LEAD-ACID

% VOLTAGE CONTROLLER

    % TO BE SELECTED BY THE DESIGNER
    bat2.wu=1;    % (rad/s) - Natural frequency
    bat2.xiu=0.7; % (-)     - Damping coefficient

    % CALCULATIONS
    bat2.C=(bat2.C_n_pack*(bat2.Uexp_pack +
bat2.Unom_pack))/((bat2.Uexp_pack^2)-(bat2.Unom_pack^2)); % (F)
    bat2.Kpu=2*bat2.xiu*bat2.wu*bat2.C;  % (-) - Proportional gain
    bat2.Kiu=bat2.wu^2*bat2.C;           % (-) - Integral gain

% CURRENT CONTROLLER

    % TO BE SELECTED BY THE DESIGNER
    bat2.wi=20;   % (rad/s) - Natural frequency
    bat2.xii=0.7; % (-)     - Damping coefficient

    % CALCULATIONS
    bat2.Kpi=2*bat2.xii*bat2.wi*bat2.L/dc.E; % (-) - Proportional gain
    bat2.Kii=bat2.wi^2*bat2.L/dc.E;          % (-) - Integral gain

%% SETPOINTS AND INITIAL CONDITIONS FOR SIMULATION

    % INITIAL CONDITIONS
    bat1.initial_z = 0.7;
    bat1.initial_ocv =
interp1(bat1.soc_ocv_lookuptable,bat1.ocv_ocv_lookuptable_pack,
bat1.initial_z,'linear','extrap');
    bat2.initial_z = 0.7;
    bat2.initial_ocv =
interp1(bat2.soc_ocv_lookuptable,bat2.ocv_ocv_lookuptable_pack,
bat2.initial_z,'linear','extrap');
```

# Annex II: Least-squares estimation theory for the adjustment of the parameters of the battery model

Model parameters can be derived from a procedure in which the response of simulation models is fitted to the real performance of battery cells. To do so, model equations may be discretized, to fit with time step of collected data from measurement devices. In this sense, the above presented discretized model equations are useful. Following subsections present the procedures that permit to obtain model parameters.

The basis for **least-squares estimation theory** are explained in [5]. The idea behind this theory is that a response variable $Y$ characterizing a system, can be partly explained by the variation of the other variables in the model, called covariables $X$. Given the value of $X$, the best prediction of $Y$ is the mean of function $f(X)$. So the actual response $Y$ is function of $f(X)$ plus a noise,

$$Y = f(X) + noise \tag{41}$$

The function $f(X)$ is a regression function. Regression parameters are collected in vector $\beta = (\beta_1, \dots, \beta_p)$ and in case of linear regression, $f(X)$ –now $f_\beta(X)$-- can be written as $f_\beta(X) = X_1\beta_1 + \dots + X_p\beta_p$. Given $k$ samples of measured data (and $p \leq k$), we can define a vector for measured response $y = (y_1, \dots, y_k)'$, and the matrix for observed data $X$,

$$X = \begin{pmatrix} x_{1,1} & \cdots & x_{1,p} \\ \vdots & \ddots & \vdots \\ x_{k,1} & \cdots & x_{k,p} \end{pmatrix} \tag{42}$$

The idea is to find the best estimation for regression parameters, $\hat{\beta}$, that minimizes the error between the response of the system and the linear regression of observed data. Such estimation for regression parameter $\hat{\beta}$, is named least-squares estimator, and is that over all possible value $b$ that minimizes

$$\sum_{i=1}^{k} \left(y_i - f_b(x_i)\right)^2 \tag{43}$$

For a linear regression, and in case $X$ has full column rank, so no column can be written as linear combination of other columns, the least squares estimator $\hat{\beta}$ can be calculated by,

$$\hat{\beta} = (X'X)^{-1}X'y \tag{44}$$

Let's apply least-squares estimation theory for the identification of the parameters of the Simple model. In this model (see equation (1), in section 2.2.1.1), the response variable would be the cell voltage $y_k$. However, variable $OCV(z_k)$ cannot be considered as a direct observable variable while charging and discharging a battery, so cannot be included as part of matrix $X$. Instead, the relationship between the open circuit voltage of the cell and the state of charge, $OCV(z_k)$ should be derived from specific discharge tests at very low discharge rate. So, while adopting the data for model parameters identification, that relationship $OCV(z_k)$ is considered as known. Then, as the measurable variable $Y$, instead of considering the cell voltage $y_k$, it will be, for any *k*-th time, the expression

$$Y = [y_1 - OCV(z_1), \dots, y_k - OCV(z_k)]^T \tag{45}$$

This output, or response variable, can be explained by the variation in the other co-variables, building matrix $X$ as,

$$X = [x_1, \dots x_p]^T \tag{46}$$

and the rows for $X$ are,

$$x_k^T = [i_k^+, i_k^-] \tag{47}$$

And the vector for unknown parameters

$$\hat{\beta}^T = [R^+, R^-] \tag{48}$$

Then, the output of the system $Y$ can be calculated as

$$Y = X\hat{\beta} \tag{49}$$

and the least square estimator $\hat{\beta}$ is calculated as

$$\hat{\beta} = (X^T X)^{-1} X^T Y \tag{50}$$

# Annex III: Cybersecurity analysis – Secure TLS and Secure Cipher Suits

Transport Layer Security (TLS) is the secure successor of SSL. However, there are differences between each version of TLS. To make it short, TLS should only be used as version 1.2 and the latest version 1.3. Also, when using TLS it is essential to only enable secure cipher suits which are listed in **Table 14**.

| TLSv1.2 | TLSv1.3 |
|---|---|
| TLS_DHE_RSA_WITH_AES_128_GCM_SHA256 | TLS_AES_128_GCM_SHA256 |
| TLS_ECDHE_RSA_WITH_AES_128_GCM_SHA256 | TLS_AES_128_CCM_SHA256 |
| TLS_DHE_RSA_WITH_AES_256_GCM_SHA384 | TLS_AES_256_GCM_SHA384 |
| TLS_ECDHE_RSA_WITH_AES_256_GCM_SHA384 | |

**Table 14**. Secure Cipher Suits